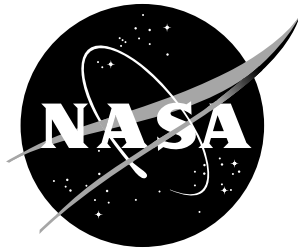


NASA/TP-2003-212641
ARL-TR-2824



Full-Scale Crash Test and Finite Element Simulation of a Composite Prototype Helicopter

*Karen E. Jackson, Edwin L. Fasanella, and Richard L. Boitnott
United States Army Research Laboratory, Vehicle Technology Directorate*

*Karen H. Lyle
Langley Research Center, Hampton, Virginia*

August 2003

The NASA STI Program Office ... in Profile

Since its founding, NASA has been dedicated to the advancement of aeronautics and space science. The NASA Scientific and Technical Information (STI) Program Office plays a key part in helping NASA maintain this important role.

The NASA STI Program Office is operated by Langley Research Center, the lead center for NASA's scientific and technical information. The NASA STI Program Office provides access to the NASA STI Database, the largest collection of aeronautical and space science STI in the world. The Program Office is also NASA's institutional mechanism for disseminating the results of its research and development activities. These results are published by NASA in the NASA STI Report Series, which includes the following report types:

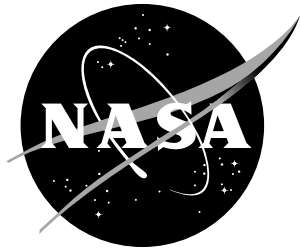
- **TECHNICAL PUBLICATION.** Reports of completed research or a major significant phase of research that present the results of NASA programs and include extensive data or theoretical analysis. Includes compilations of significant scientific and technical data and information deemed to be of continuing reference value. NASA counterpart of peer-reviewed formal professional papers, but having less stringent limitations on manuscript length and extent of graphic presentations.
- **TECHNICAL MEMORANDUM.** Scientific and technical findings that are preliminary or of specialized interest, e.g., quick release reports, working papers, and bibliographies that contain minimal annotation. Does not contain extensive analysis.
- **CONTRACTOR REPORT.** Scientific and technical findings by NASA-sponsored contractors and grantees.
- **CONFERENCE PUBLICATION.** Collected papers from scientific and technical conferences, symposia, seminars, or other meetings sponsored or co-sponsored by NASA.
- **SPECIAL PUBLICATION.** Scientific, technical, or historical information from NASA programs, projects, and missions, often concerned with subjects having substantial public interest.
- **TECHNICAL TRANSLATION.** English-language translations of foreign scientific and technical material pertinent to NASA's mission.

Specialized services that complement the STI Program Office's diverse offerings include creating custom thesauri, building customized databases, organizing and publishing research results ... even providing videos.

For more information about the NASA STI Program Office, see the following:

- Access the NASA STI Program Home Page at <http://www.sti.nasa.gov>
- E-mail your question via the Internet to help@sti.nasa.gov
- Fax your question to the NASA STI Help Desk at (301) 621-0134
- Telephone the NASA STI Help Desk at (301) 621-0390
- Write to:
NASA STI Help Desk
NASA Center for AeroSpace Information
7121 Standard Drive
Hanover, MD 21076-1320

NASA/TP-2003-212641
ARL-TR-2824



Full-Scale Crash Test and Finite Element Simulation of a Composite Prototype Helicopter

*Karen E. Jackson, Edwin L. Fasanella, and Richard L. Boitnott
United States Army Research Laboratory, Vehicle Technology Directorate*

*Karen H. Lyle
Langley Research Center, Hampton, Virginia*

National Aeronautics and
Space Administration

Langley Research Center
Hampton, Virginia 23681-2199

August 2003

Acknowledgments

The authors would like to recognize several organizations, companies, and individuals for their support of this research program. The Advanced Composite Airframe Program (ACAP) helicopter plus initial funding was provided by the U.S. Army Aviation Applied Technology Directorate, located at Ft. Eustis, Virginia. The MSC.Nastran modal-vibration model of the ACAP helicopter was provided by Sikorsky Aircraft and the authors would like to acknowledge Charles Clarke and Joseph Shen of Sikorsky Aircraft for their many helpful discussions concerning the model development. Joe McEntire and Alan Lewis of the U.S. Army Aeromedical Research Laboratory provided crew seats, troop seats, and one anthropomorphic dummy for the crash test. Roy Burrows of H. Koch & Sons provided new MA-16 inertia reels, crew restraints, and the electronic crash sensor unit.

The use of trademarks or names of manufacturers in the report is for accurate reporting and does not constitute an official endorsement, either expressed or implied, of such products or manufacturers by the National Aeronautics and Space Administration or the U.S. Army.
--

Available from:

NASA Center for AeroSpace Information (CASI)
7121 Standard Drive
Hanover, MD 21076-1320
(301) 621-0390

National Technical Information Service (NTIS)
5285 Port Royal Road
Springfield, VA 22161-2171
(703) 605-6000

Contents

List of Tables	v
List of Figures.....	v
Nomenclature.....	x
1. Introduction	1
2. Test Program	3
2.1. Test Objectives.....	3
2.2. Description of the Crash Test Article.....	3
2.3. Lessons Learned From the 1987 Drop Test	6
2.4. Test Article Modifications	7
2.5. Seats, Anthropomorphic Dummies, and Associated Instrumentation.....	10
2.6. Ballast Weight and Center of Gravity	11
2.7. Instrumentation and Data Acquisition.....	11
2.8. Ancillary Experiments	13
2.9. Test Methods	13
3. Summary of Test Results	16
3.1. Sequence of Events	16
3.2. Acceleration Time History Responses	17
3.3. Fuselage Deformations	24
3.4. Hydrodynamic Fuel Tank Pressures.....	24
3.5. Landing Gear Response	25
3.6. ECSU Response	26
3.7. Seat Responses	26
3.8. Occupant Responses	30
3.9. Injury Prediction Criteria	33
3.9.1. Dynamic Response Index	33
3.9.2. Spinal Force	37
3.9.3. Head Injury Criterion.....	38
3.9.4. Whole-Body Acceleration Tolerance.....	39
3.9.5. Injury Assessment Reference Values.....	41
3.9.6. Summary of Injury Assessment	42
4. Model Development.....	42
4.1. Description of the MSC.Nastran Modal-Vibration Model	43
4.2. Conversion of the Modal-Vibration Model to a Crash Model	43
4.3. Description of the Crash Model.....	45
5. Simulation Strategy	47
5.1. Landing Gear Model	47
5.2. Rigid Structural Model	49
5.3. Flexible Structural Model	50
6. Test and Analysis Correlation.....	50
6.1. Sequence of Events	50
6.2. Structural Deformation	52
6.3. Comparison of Velocity Responses.....	54
6.4. Predicted Landing Gear Forces	55
6.5. Comparison of Predicted Acceleration Time Histories With Test Data	55

7. Observations and Lessons Learned	59
7.1. Testing and Instrumentation	59
7.2. Modeling	60
8. Concluding Remarks	62
References.....	64
Appendix—Raw and Filtered Test Data.....	67

List of Tables

Table 1. Airframe Crash Test Sequence	17
Table 2. Peak Vertical Acceleration Values and Corresponding Times at Different Locations	23
Table 3. Dynamic Response Limit Values for Low, Moderate, and High Risk	37
Table 4. Summary of Copilot Head Injury Assessment.....	39
Table 5. Comparison of Copilot Data With IARV.....	41
Table 6. Primary Material Properties in the MSC.Dytran Model of the ACAP Helicopter	46
Table 7. Summary of Major Concentrated Masses in the Finite Element Model.....	46
Table 8. Predicted and Experimental Time Sequence of Events.....	51
Table 9. Predicted and Experimental Velocities at 0.045 and 0.095 s for Nine Locations	55
Table 10. Predicted and Experimental Peak Accelerations at Nine Locations	58
Table A1. Instrumentation Description	67

List of Figures

Figure 1. Photograph of the Sikorsky ACAP crash test article.	4
Figure 2. Schematic of the main landing gear in the Sikorsky ACAP helicopter.....	4
Figure 3. Composite subfloor and details of the lower forward fuselage.	5
Figure 4. Schematic of the Sikorsky ACAP helicopter.....	6
Figure 5. Nose gear configuration before and after modification.....	7
Figure 6. Nose gear energy-absorbing canister and static load versus stroke curve.....	8
Figure 7. Main landing gear drag beam modification.....	9
Figure 8. Main landing gear attachment lug before and after reinforcement.....	10
Figure 9. Selected accelerometer locations on the airframe structure.....	12
Figure 10. Schematic of the camera locations (not to scale).	13
Figure 11. Fuel tank pressure transducers and mounting fixtures.....	14
Figure 12. IDRF gantry structure used to perform crash test of the ACAP helicopter.....	15
Figure 13. Side view of helicopter mounting system.....	16
Figure 14. Front view images from a high-speed camera showing key events.	18
Figure 15. Left-side images from a high-speed camera showing key events.....	18
Figure 16. Posttest photograph of the ACAP helicopter in the final resting position.....	19
Figure 17. Filtered floor-level acceleration responses in three directions at the copilot position.....	19
Figure 18. Filtered vertical floor-level acceleration responses near the crew and troop occupants.....	20
Figure 19. Floor-level velocity responses at the crew and troop locations.	20
Figure 20. Filtered acceleration responses of the pilot and copilot seat floor as measured by the DAS from NASA and USAARL.....	21
Figure 21. Filtered vertical acceleration responses at several locations on the ACAP helicopter.	22
Figure 22. Vertical acceleration peaks (g) on the helicopter. Note that left and right side numbers are averaged.....	23
Figure 23. Posttest photograph showing subfloor deformations (FS 143 and BL 8).....	24
Figure 24. Mid-depth internal fuel tank pressures.	25
Figure 25. Posttest photograph of honeycomb canister halves from the modified nose gear.	25
Figure 26. Interior rear view images of crew seats.	26

Figure 27. Image showing maximum downward motion of the pilot (right crew) at 0.182 s after left tire contact.	27
Figure 28. Posttest photograph of the unpinned pilot seat.	27
Figure 29. Posttest photographs of the copilot (left crew) dummy.	28
Figure 30. Posttest photographs of the right and left troop dummies and seats.	28
Figure 31. Posttest photograph of the inboard wire-bender mechanism of the left troop seat.	29
Figure 32. Filtered vertical acceleration responses of the crew floor, seat pan, and chest.	29
Figure 33. 1000-Hz filtered pilot and copilot head acceleration responses in three directions.	30
Figure 34. Filtered copilot T-1 thoracic acceleration responses in three directions.	31
Figure 35. Filtered vertical chest acceleration responses of four dummies.	31
Figure 36. Filtered forward chest acceleration responses of four dummies.	32
Figure 37. Filtered pilot pelvis acceleration responses in three directions.	33
Figure 38. Filtered seat pan vertical acceleration responses.	33
Figure 39. Restraint system loads for the pilot and copilot.	34
Figure 40. Schematic of the DRI spinal injury model; m is mass in lb-s ² /in., ζ is damping ratio = 0.224, k is spring stiffness in lb/in., δ is deflection in inches, and $a(t)$ is input acceleration in in/s ²	34
Figure 41. Continuous DRI responses of the four dummies.	35
Figure 42. Occupant responses and the continuous DRI model.	36
Figure 43. Axis system used to calculate the combined DRI response.	36
Figure 44. Injury risk assessment for the pilot and copilot dummies.	37
Figure 45. Pilot and copilot vertical lumbar load responses.	38
Figure 46. Resultant acceleration response of the copilot head.	39
Figure 47. Pilot chest and pelvis vertical acceleration data plotted on the Eiband curve.	40
Figure 48. Copilot chest vertical acceleration data plotted on the Eiband curve.	40
Figure 49. Vertical chest acceleration data of the troop dummies plotted on the Eiband curve.	41
Figure 50. MSC.Nastran modal-vibration model of the ACAP helicopter.	43
Figure 51. Finite element model of the ACAP helicopter subfloor.	44
Figure 52. Final crash model of the ACAP helicopter.	45
Figure 53. Schematic of ACAP landing gear, looking aft.	48
Figure 54. Schematic of the landing gear finite element model.	49
Figure 55. Predicted and experimental crash sequence and deformation.	51
Figure 56. Model deformation and posttest photograph of the bulkhead at FS 188.	52
Figure 57. Model and a posttest photograph of deformed subfloor beams.	53
Figure 58. Predicted and experimental velocity responses at three locations.	54
Figure 59. Predicted left, right, and nose gear axial force time histories.	56
Figure 60. Predicted and measured vertical accelerations of the pilot and copilot floor locations.	56
Figure 61. Predicted and measured vertical accelerations at the troop seat floor locations.	57
Figure 62. Predicted and measured acceleration responses for the right and left engines.	57
Figure 63. Predicted and measured acceleration responses of the top of the right main gear and the top of the bulkhead at FS 188.	58
Figure A1. Electrical anomalies in dynamic load cell data.	71
Figure A2. Lumbar load cell data filtered with 60-Hz low-pass digital filter.	71
Figure A3. Unfiltered vertical acceleration response of the left engine with electrical anomalies.	71
Figure A4. Vertical velocity response (integrated vertical acceleration) of the left engine.	71
Figure A5. Acceleration response of the fuselage bulkhead at FS 267.	72
Figure A6. Vertical velocity response of the bulkhead at FS 267.	72

Figure A7. Unfiltered vertical acceleration response of the pilot head.....	73
Figure A8. Unfiltered side acceleration response of the pilot head.....	73
Figure A9. Unfiltered vertical acceleration response of the pilot chest.	73
Figure A10. Unfiltered forward acceleration response of the pilot chest.....	73
Figure A11. Unfiltered side acceleration response of the pilot chest.	73
Figure A12. Vertical acceleration and velocity responses of the pilot pelvis.	74
Figure A13. Unfiltered (left plot) and filtered (right plot) forward acceleration responses of the pilot pelvis.....	74
Figure A14. Unfiltered (left plot) and filtered (right plot) side acceleration responses of the pilot pelvis.	75
Figure A15. Vertical acceleration and velocity responses of the pilot seat pan.....	75
Figure A16. Unfiltered (left plot) and filtered (right plot) forward acceleration responses of the pilot seat pan.	76
Figure A17. Unfiltered (left plot) and filtered (right plot) pilot lumbar load.....	76
Figure A18. Unfiltered (left plot) and filtered (right plot) pilot lap belt load.	76
Figure A19. Unfiltered (left plot) and filtered (right plot) pilot shoulder belt load.	77
Figure A20. Vertical acceleration and velocity responses of the copilot seat pan.....	77
Figure A21. Unfiltered (left plot) and filtered (right plot) forward acceleration responses of the copilot seat pan.	78
Figure A22. Unfiltered (left plot) and filtered (right plot) copilot lap belt load.	78
Figure A23. Unfiltered (left plot) and filtered (right plot) forward acceleration responses of the copilot seat floor.	78
Figure A24. Unfiltered (left plot) and filtered (right plot) side acceleration responses of the copilot seat floor.....	79
Figure A25. Vertical acceleration and velocity responses of the copilot seat floor.....	79
Figure A26. Unfiltered copilot head acceleration time histories in three directions.	80
Figure A27. Unfiltered copilot head pitch rate about the side axis.	80
Figure A28. Unfiltered copilot head/neck force time histories in three directions.....	81
Figure A29. Unfiltered copilot head moment time histories in two directions.....	81
Figure A30. Unfiltered copilot lumbar force time histories in three directions.	82
Figure A31. Unfiltered forward acceleration response of the copilot torso sternum.....	82
Figure A32. Unfiltered vertical acceleration response of the copilot torso sternum.	83
Figure A33. Unfiltered moment responses of the copilot pelvis/lumbar region.....	83
Figure A34. Unfiltered (left plot) and filtered (right plot) forward acceleration responses of the copilot torso.	83
Figure A35. Unfiltered (left plot) and filtered (right plot) side acceleration responses of the copilot torso.....	84
Figure A36. Unfiltered (left plot) and filtered (right plot) vertical acceleration responses of the copilot torso.	84
Figure A37. Unfiltered shear force response of the copilot torso in the forward direction.....	84
Figure A38. Unfiltered shear force response of the copilot torso in the side direction.	84
Figure A39. Unfiltered force response of the copilot torso in the vertical direction.	85
Figure A40. Unfiltered copilot torso moment response about the forward axis.	85
Figure A41. Unfiltered copilot torso moment time history about the side axis.	85
Figure A42. Unfiltered copilot torso moment time history about the vertical axis.	85
Figure A43. Unfiltered (left plot) and filtered (right plot) vertical acceleration responses of the right troop chest.	86

Figure A44. Unfiltered (left plot) and filtered (right plot) forward acceleration responses of the right troop chest.	86
Figure A45. Unfiltered (left plot) and filtered (right plot) side acceleration responses of the right troop chest.....	86
Figure A46. Vertical acceleration and velocity responses of the right troop seat pan.....	87
Figure A47. Unfiltered (left plot) and filtered (right plot) vertical acceleration responses of the left troop chest.	88
Figure A48. Unfiltered (left plot) and filtered (right plot) forward acceleration responses of the left troop chest.	88
Figure A49. Unfiltered (left plot) and filtered (right plot) side acceleration responses of the left troop chest.....	88
Figure A50. Vertical acceleration and velocity responses of the left troop seat pan.	89
Figure A51. Vertical acceleration and velocity responses of the pilot seat floor.....	90
Figure A52. Unfiltered (left plot) and filtered (right plot) forward acceleration responses of the pilot seat floor.	90
Figure A53. Unfiltered (left plot) and filtered (right plot) side acceleration responses of the pilot seat floor.	91
Figure A54. Vertical acceleration and velocity responses of the copilot seat floor.....	91
Figure A55. Unfiltered (left plot) and filtered (right plot) forward acceleration responses of the copilot seat floor.	92
Figure A56. Unfiltered (left plot) and filtered (right plot) side acceleration responses of the copilot seat floor.....	92
Figure A57. Vertical acceleration and velocity responses of the right troop seat floor.....	93
Figure A58. Unfiltered (left plot) and filtered (right plot) forward acceleration responses of the right troop seat floor.	93
Figure A59. Vertical acceleration and velocity responses of the left troop seat floor.	94
Figure A60. Unfiltered (left plot) and filtered (right plot) forward acceleration responses of the left troop seat floor.	94
Figure A61. Unfiltered (left plot) and filtered (right plot) forward acceleration responses of the floor at FS 122.	95
Figure A62. Unfiltered (left plot) and filtered (right plot) forward acceleration responses of the floor at FS 188.	95
Figure A63. Vertical acceleration and velocity responses of the top of the bulkhead at FS 188.	96
Figure A64. Unfiltered (left plot) and filtered (right plot) forward acceleration responses of the top of the bulkhead at FS 188.	96
Figure A65. Vertical acceleration and velocity responses of the bulkhead at FS 255.....	97
Figure A66. Unfiltered (left plot) and filtered (right plot) forward acceleration responses of the bulkhead at FS 255.	97
Figure A67. Vertical acceleration and velocity responses of the bulkhead at FS 267.....	98
Figure A68. Unfiltered (left plot) and filtered (right plot) forward acceleration responses of the bulkhead at FS 267.	98
Figure A69. Unfiltered (left plot) and filtered (right plot) side acceleration responses of the bulkhead at FS 267.....	99
Figure A70. Vertical acceleration and velocity responses of the left engine.	99
Figure A71. Unfiltered (left plot) and filtered (right plot) forward acceleration responses of the left engine.....	100
Figure A72. Unfiltered (left plot) and filtered (right plot) side acceleration responses of the left engine.	100

Figure A73. Vertical acceleration and velocity responses of the right engine.....	101
Figure A74. Unfiltered (left plot) and filtered (right plot) forward acceleration responses of the right engine.	101
Figure A75. Vertical acceleration and velocity responses of rotor head.....	102
Figure A76. Unfiltered (left plot) and filtered (right plot) forward acceleration responses of the rotor head.	102
Figure A77. Vertical acceleration and velocity responses of the tail rotor.	103
Figure A78. Unfiltered (left plot) and filtered (right plot) forward acceleration responses of the tail rotor.....	103
Figure A79. Vertical acceleration and velocity responses of the left main gear hub.....	104
Figure A80. Vertical acceleration and velocity responses of the right main gear hub.	105
Figure A81. Vertical acceleration and velocity responses of the right main gear top.	106
Figure A82. Unfiltered (left plot) and filtered (right plot) pressure responses of the fuel tank (inside left).	107
Figure A83. Unfiltered (left plot) and filtered (right plot) pressure responses of fuel tank (inside right).	107
Figure A84. Unfiltered (left plot) and filtered (right plot) strain responses from the tail continuity gauge.....	107

Nomenclature

ACAP	Advanced Composite Airframe Program
ARL-VTD	Army Research Laboratory, Vehicle Technology Directorate
ATB	Articulated Total Body
$a(t)$	resultant acceleration measured at center of gravity of head as function of time, g
BL	butt line
b	value of multiaxis dynamic injury-risk criterion
CG	center of gravity
CPU	central processing unit
DAS	data acquisition system
DRI	Dynamic Response Index
DRX	maximum DRI in X -axis
DRY	maximum DRI in Y -axis
DRZ	maximum DRI in Z -axis
DRX_L	limit values defined for low, moderate, and high risk in X -axis
DRY_L	limit values defined for low, moderate, and high risk in Y -axis
DRZ_L	limit values defined for low, moderate, and high risk in Z -axis
E	Young's modulus
ECSU	electronic crash sensor unit
FAR	Federal Aviation Regulation
FMVSS	Federal Motor Vehicle Safety Standard
FS	fuselage station
G	shear modulus
HIC	head injury criterion
IARV	Injury Assessment Reference Values

IDRF	Impact Dynamics Research Facility
krad	kiloradian
MIL-STD	Military Standard
NASA	National Aeronautics and Space Administration
NHTSA	National Highway Traffic Safety Administration
SAE	Society of Automotive Engineers
t	time, s
t_1	initial time of HIC integration
t_2	final time of HIC integration
USAARL	United States Army Aeromedical Research Laboratory
WL	waterline
X	global vector defining longitudinal direction from rear to front of aircraft
x	X -axis coordinate
Y	global vector defining lateral direction from left to right of aircraft
y	Y -axis coordinate
Z	global vector defining vertical direction from ground to rotor of aircraft
z	Z -axis coordinate
β	parameter defining general risk of injury
δ_{\max}	maximum deflection
ν	Poisson's ratio
ω_n	natural frequency

Abstract

A full-scale crash test of a prototype composite helicopter was performed at the Impact Dynamics Research Facility at NASA Langley Research Center in 1999 to obtain data for validation of a finite element crash simulation. The helicopter was the flight test article built by Sikorsky Aircraft during the Advanced Composite Airframe Program (ACAP). The composite helicopter was designed to meet the stringent Military Standard (MIL-STD-1290A) crashworthiness criteria. For the crash test, the helicopter was outfitted with two crew and two troop seats and four anthropomorphic dummies. The test was performed at 38-ft/s vertical and 32.5-ft/s horizontal velocity onto a rigid surface. An existing modal-vibration model of the Sikorsky ACAP helicopter was converted into a model suitable for crash simulation. A two-stage modeling approach was implemented and an external user-defined subroutine was developed to represent the complex landing gear response. The crash simulation was executed by using a nonlinear, explicit transient dynamic finite element code. Predictions of structural deformation and failure, the sequence of events, and the dynamic response of the airframe structure were generated and the numerical results were correlated with the experimental data to validate the simulation. The test results, the model development, and the test-analysis correlation are described.

1. Introduction

Advances in software development and computer hardware have progressed such that computer simulations of full-scale aircraft crash events are now possible. Crash analysis codes can be used to influence airframe designs to obtain improved crashworthiness, to aid in certification, to predict occupant responses to impact and assess injury risk, and to evaluate numerous crash scenarios not economically feasible with full-scale crash testing. Further confidence in the predictive capabilities of crash simulation codes will enable aircraft manufacturers to evaluate and improve the crashworthy performance of their airframe designs with less reliance on expensive component or full-scale testing. In the future, the crashworthy performance of seats and airframe systems may be certified by analysis. Currently, the validation of nonlinear, transient dynamic finite element codes through analytical and experimental correlation is an important step in achieving these goals. In fact, the “validation of numerical simulations” was identified as one of five key technology shortfalls during the Workshop on Computational Methods for Crashworthiness held at NASA Langley Research Center in 1992 (ref. 1).

The U.S. Army has been active in supporting the development and utilization of crash modeling and simulation codes for many decades. More than 25 years ago, the U.S. Army sponsored initial development of a kinematic crash analysis code, KRASH, by the Lockheed-California Company (ref. 2). Kinematic codes employ a semiempirical modeling approach that uses lumped masses, beams, and nonlinear springs to represent the airframe structure. These codes rely heavily on test data for definition of spring properties to characterize the crushing behavior of the subfloor, landing gear, and other energy-absorbing components. Good correlation between analytical and experimental data is usually obtained for global parameters, such as engine or landing gear response. However, these codes are unable to predict localized responses, such as the stress level in a skin panel at a particular time during a crash event.

A new generation of crash analysis codes has been developed to accurately simulate the nonlinear, transient dynamic response of airframe structures. These finite element codes, such as LS-DYNA3D (ref. 3), MSC.Dytran (ref. 4), and PAM-CRASH (ref. 5), use an explicit solver, which unlike an implicit code, does not need to repetitively decompose large global stiffness matrices. In addition, efficient beam, shell, and solid elements are used to achieve relatively quick run times for very large models. The new crash analysis codes are capable of modeling nonlinear geometric behavior, including large structural deformations and rotations, and nonlinear material responses. These codes are effective in modeling materials, such as metals, that deform plastically and that have well-known failure mechanisms. However, current and future generations of aircraft will be fabricated of advanced composite materials. The material response and failure behavior of these efficient, high-strength materials are difficult to model. In addition, structural composite materials can exhibit a wide range of material responses, from linear elastic to completely nonlinear anisotropic behavior, depending on the individual fiber and matrix properties and the laminate stacking sequence. Also, laminated composite materials exhibit a wide variety of failure modes, including matrix cracking, fiber failure, and delamination, which can occur singly or in combination. These failure modes can change depending on the type and rate of loading. In general, the initial failure event in a single ply of a composite laminate does not produce catastrophic failure. Consequently, the capability to model the progressive failure of composite materials, from initial damage to ultimate failure, is needed. With the increased application of composite materials in the construction of advanced aircraft and rotorcraft, it is important to build confidence in the computational capabilities of these codes through analytical and experimental validation.

In 1997, the Army Research Laboratory, Vehicle Technology Directorate (ARL-VTD) initiated an activity to establish a standardized and validated structural crash dynamics modeling and simulation capability from a commercial off-the-shelf computer code that would satisfy the need for a crashworthy performance and design evaluation tool. As part of this work, a full-scale crash test of the Sikorsky Advanced Composite Airframe Program (ACAP) residual flight test article was planned to generate experimental data for correlation with the crash simulation. The NASA Aviation Safety Program provided support for the crash test and model validation (ref. 6).

A full-scale crash test of the Sikorsky ACAP flight test article was conducted in June 1999. For the crash test, the aircraft was outfitted with two crew and two troop seats and four instrumented anthropomorphic dummies. The measured test conditions were 38-ft/s vertical and 32.5-ft/s horizontal velocity onto a rigid impact surface with an impact attitude of 6.25° nose-up pitch and a 3.5° left-down roll. Approximately 120 channels of data from the airframe, seats, and dummies were collected at 10 000 samples per second. In addition, two ancillary experiments were performed: evaluation of an electronic crash sensor and measurement of fuel tank dynamic pressures. The complete set of raw and filtered test data is provided in the appendix, following the main report.

A finite element simulation of the full-scale crash test was developed using the nonlinear, explicit transient dynamic code MSC.Dytran. An existing modal-vibration model of the Sikorsky ACAP helicopter was obtained and converted into a model suitable for the impact simulations. A two-stage modeling strategy was implemented, and an external user-defined subroutine was developed to represent the complex landing gear response. Analytical predictions of the sequence of events, structural damage, subfloor crushing, and the acceleration responses of the airframe and large mass items such as the engines and rotor transmission were correlated with the experimental data to validate the crash simulation.

The objectives of this paper are to summarize the results of the full-scale crash test of the Sikorsky ACAP helicopter, to describe the development of the finite element model and the approach used to perform the crash simulation, and to present the model validation through test and analysis correlation.

2. Test Program

A full-scale crash test of the Sikorsky ACAP flight test article was performed at the Impact Dynamics Research Facility (IDRF) at NASA Langley Research Center in Hampton, Virginia. The IDRF is a 240-ft-high gantry structure that has been used for conducting full-scale crash tests of light aircraft and rotorcraft since the early 1970s (refs. 7 and 8). The helicopter was the flight test article built by Sikorsky Aircraft Corporation under sponsorship by the U.S. Army during the ACAP (refs. 9–12). The purpose of the ACAP was to demonstrate the potential of advanced composite materials to save weight and cost in airframe structures while achieving systems compatibility and meeting Army requirements for vulnerability reduction, reliability, maintainability, and survivability. In 1981, the U.S. Army awarded separate contracts to Bell Helicopter Textron and Sikorsky Aircraft Corporation to develop, manufacture, and test helicopters constructed primarily of advanced composite materials. Each company manufactured three airframes that were tested under a variety of static and dynamic conditions to demonstrate compliance with the program objectives. One helicopter airframe from each company was equipped to become a flying prototype (flight test article). The Bell and Sikorsky ACAP static test articles were crash tested in 1987 at the NASA IDRF by the U.S. Army to demonstrate their impact performances and to verify compliance with crash requirements (refs. 10 and 12). The lessons learned from the 1987 crash test of the Sikorsky static test article proved extremely useful in preparations for the 1999 drop test of the residual flight test article.

2.1. Test Objectives

The primary objective of the 1999 crash test was to provide experimental data for validation of an explicit, transient dynamic finite element crash simulation. In addition, the airframe crash test allowed two ancillary experiments to be performed, including evaluation of an electronic crash sensor and measurement of fuel tank dynamic pressures. The resultant velocity of the impact test was 50 ft/s with components of 38-ft/s vertical and 32.5-ft/s horizontal velocity onto a flat concrete surface. This impact condition was chosen for several reasons. First, the Military Standard MIL-STD-1290A (ref. 13) crashworthiness requirement specifies a combined impact condition with 42-ft/s vertical and 27-ft/s horizontal velocity components with a resultant velocity of 50 ft/s. The vertical velocity of the test condition is less than the MIL-STD-1290A specification; however, the resultant velocity (50 ft/s) matches the resultant velocity of the standard. Also, the 38-ft/s vertical velocity component is close to the impact condition of the 1987 drop test of the Sikorsky ACAP static test article that was performed at 39-ft/s vertical velocity (ref. 10). Finally, the planned impact attitude was 5° nose-up pitch with no roll or yaw.

2.2. Description of the Crash Test Article

The crash test article, shown in figure 1, was the residual flying prototype built by Sikorsky during the ACAP. It was designated as the S-75 ACAP utility helicopter. The general configuration of the ACAP airframe is derived from Sikorsky's S-76 commercial aircraft. The dynamic components of the ACAP helicopter, such as the rotor blades, rotor transmission, and engines, are the same as those used on the S-76. However, the airframe and landing gear were completely new designs. Crashworthy design features were an integral consideration during the development process. These features include the main and nose landing gears, the airframe and energy-absorbing subfloor, the crew and troop seats, and the fuel system (ref. 10).

The primary crashworthy features of the Sikorsky ACAP helicopter are the main and nose landing gears. The landing gears are in a fixed tricycle arrangement designed for a 12.25-ft/s vertical velocity for normal landing and 42-ft/s vertical velocity for crash landing. Crash protection is provided by using a



Figure 1. Photograph of the Sikorsky ACAP crash test article.

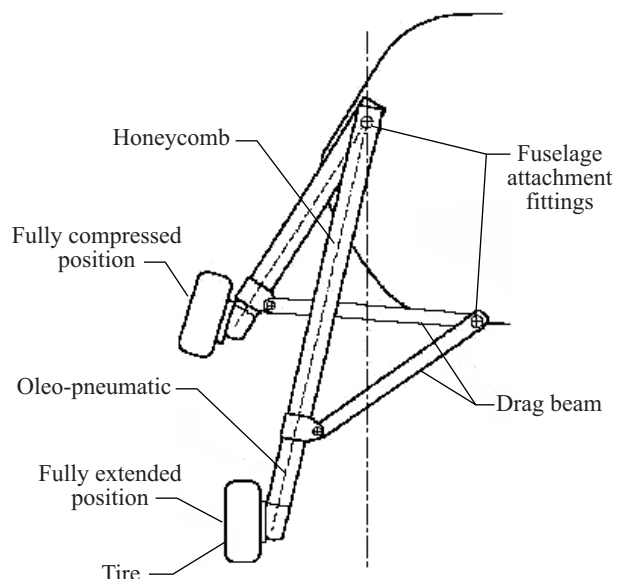


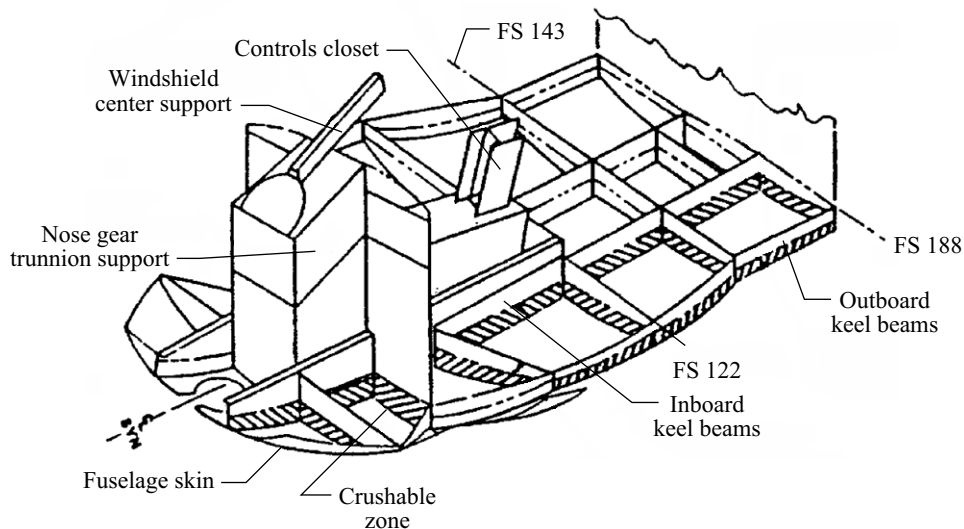
Figure 2. Schematic of the main landing gear in the Sikorsky ACAP helicopter.

two-stage shock strut in which the first stage is a conventional air-oleo design, and the second stage consists of a crushable 25-in-long honeycomb canister. Two shear pin sets were used in the landing gear design: an upper set of two pins and a lower set of four pins. The upper set protects the honeycomb from being crushed until after full 12-in. oleo stroke. The lower set is designed to fail after the honeycomb crushes approximately 1 in. Finally, the attachment fittings that connect the landing gear to the fuselage were designed to exhibit bearing failures (brooming) to absorb additional energy after the gear is fully stroked. The landing gears were designed to remove 80 percent of the kinetic energy of a crash performed at the impact conditions specified in MIL-STD-1290A (ref. 13). Figure 2 is a schematic of the main landing gear and illustrates the gear motion during impact.

Another crashworthy feature of the aircraft is the crushable lower portion of the keel beams and transverse bulkheads. Two inner keel beams and two outer keel beams were located beneath the floor. The keel beams and transverse bulkheads beneath the floor were constructed of two horizontal C-channels, one above the other, with a beaded (or waffle) web geometry, as shown in figure 3(a). The upper channel was constructed of graphite, and the lower 4-in-high beaded web was constructed of Kevlar™. The lower



(a) Posttest photograph of the subfloor consisting of two horizontal C-channels, one above the other, with a beaded (or waffle) web geometry.



(b) Schematic of the lower forward fuselage.

Figure 3. Composite subfloor and details of the lower forward fuselage.

portions of the inner keel and bulkhead beams were a thinner beaded Kevlar™ construction designed to crush and absorb energy. The graphite upper channel was not intended to crush; it was designed to support the floor and to react the crushing loads from the lower Kevlar™ channel. The crushable lower portion of the subfloor is depicted as the hatched area in the schematic of the lower forward fuselage shown in figure 3(b). This figure also depicts the controls closet located between the crew seats and the nose gear trunnion support.

The helicopter used for this crash test, shown in figure 1, had been stored in a warehouse for over 10 years. After the ACAP flight test program, the helicopter was used in a variety of tests, including vibration and gunfire tests, that left the helicopter with damage and missing components. When the helicopter was acquired for crash testing, the original energy-absorbing nose gear was missing and a modified

civil helicopter nose gear was retrofitted to the airframe. The original composite sandwich floor in the cabin had been replaced with a 0.25-in-thick aluminum plate. Fuselage bottom damage and delamination were repaired with 0.125-in-thick aluminum strips bolted to the bottom composite skin along the inboard keel beam. Small individual aluminum strips were also used to join the outboard keel beam and skin. The helicopter was missing both engines and all crew and troop seats. The main energy-absorbing landing gears were in good condition. The left and right honeycomb canisters were removed from the landing gears, inspected, and found to be in good condition. The shear pins that prevent the honeycomb from crushing until crash loads are achieved were also undamaged. In addition, the beaded Kevlar™ keel beams and bulkheads, which are the primary subfloor energy absorbers, were in good condition.

Figure 4 is a schematic of the helicopter; it indicates the coordinate system used for the test and several important locations taken from the manufacturer's specifications: fuselage station (FS), butt line (BL), and waterline (WL). Note that a left-handed coordinate system is used.

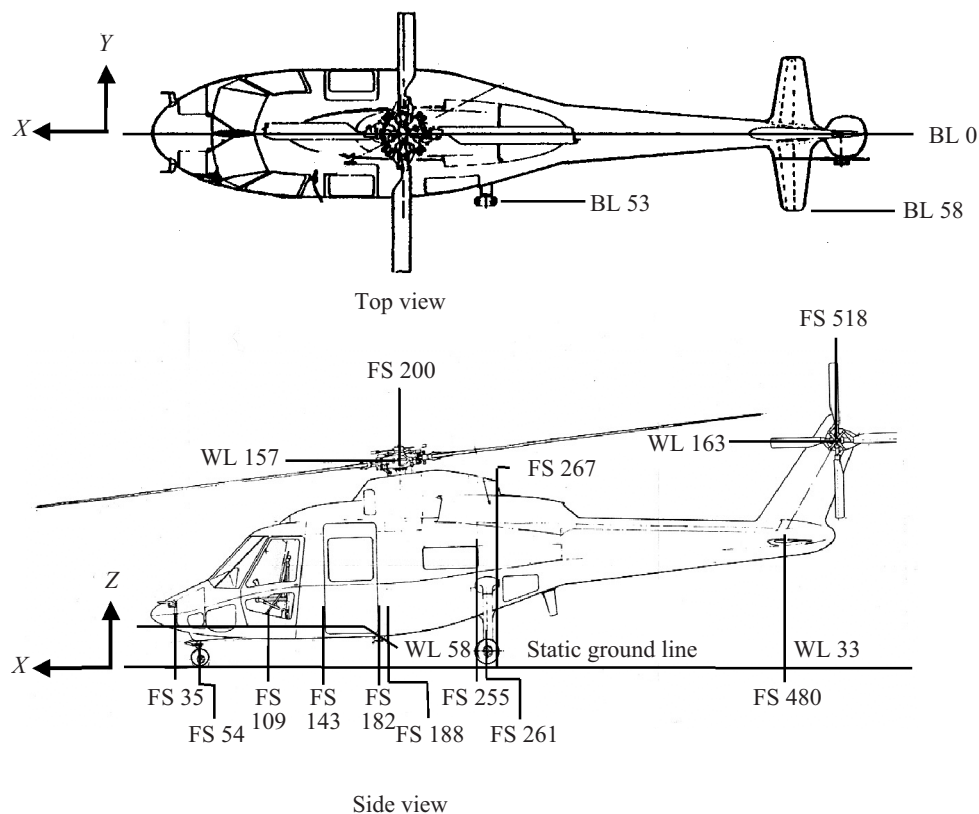


Figure 4. Schematic of the Sikorsky ACAP helicopter.

2.3. Lessons Learned From the 1987 Drop Test

The previous drop test of a Sikorsky ACAP helicopter was conducted on September 17, 1987, at NASA Langley Research Center (ref. 10). In the 1987 test, the static test article was dropped vertically from a height of 23.6 ft for an impact velocity of 39 ft/s with an impact attitude of 10° nose-up pitch and a 10° right-down roll. Based on the results obtained from this test, several structural modifications were identified to improve the crash performance of the helicopter. In the 1987 test, the upper fuselage attachment fittings of the right and left main landing gears failed before the gear absorbed its anticipated

energy contribution. When the right and left gear attachment points failed, the honeycomb stages had stroked 10.6 and 3 in., respectively, which was much less than predicted by computer simulations. The drag beam attachment lug on the right gear also failed. In addition, the nose gear did not function as designed. The nose gear struck the fuselage wheel well, limiting the total nose gear stroke to 4.5 in. The areas that failed in the 1987 test were reinforced prior to the 1999 crash test. These modifications, as described in the next section of the paper, allowed maximum performance of the landing gear system during the 1999 ACAP helicopter crash test.

2.4. Test Article Modifications

A standard, noncrashworthy nose gear was attached to the helicopter when it arrived at the IDRF. Photographs of the nose gear before and after modification are shown in figure 5. In its original configuration, the shimmy damper of the gear would impact the fuselage after stroking less than 1 in. To overcome this problem, the adapter link between the drag beam and the shimmy damper lug was replaced with an attachment connecting the drag beam directly to the lug. This arrangement moved the nose gear lug approximately 5 in. aft, and the gear was demonstrated to stroke freely upward. This geometry resulted in the tire moving forward initially as the gear stroked; however, the gear did not contact the wheel well. The shimmy damper was tightened to prevent the landing gear from rotating at impact.



(a) Before modification.

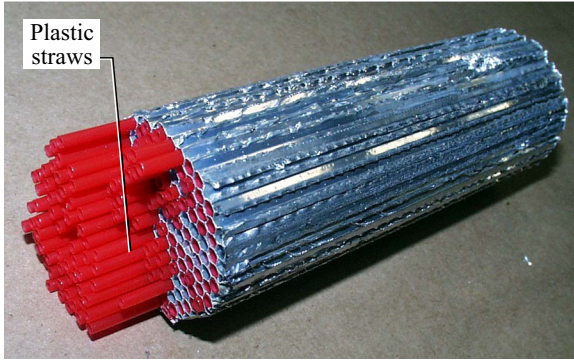


(b) After modification.

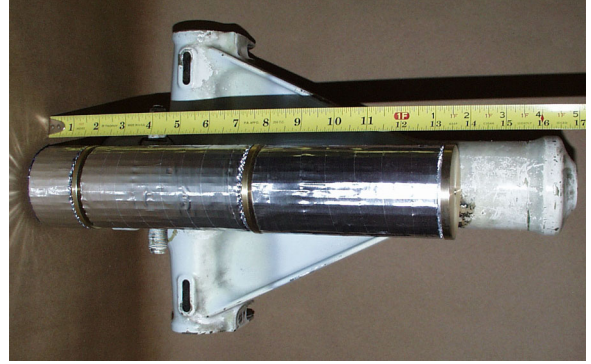
Figure 5. Nose gear configuration before and after modification.

The original ACAP nose gear was designed for 35 in. of stroke at loads between 20000 and 30000 lb to absorb over 700000 in-lb of kinetic energy (ref. 11). The replacement gear was not designed to provide a high level of energy absorption or to withstand a high velocity impact (38 ft/s). The maximum allowable ground reaction force for this gear was less than 9000 lb. Loads over this value might cause the gear to fail. With the load and stroke limitations, this gear could only absorb a small percentage of the energy of the original gear.

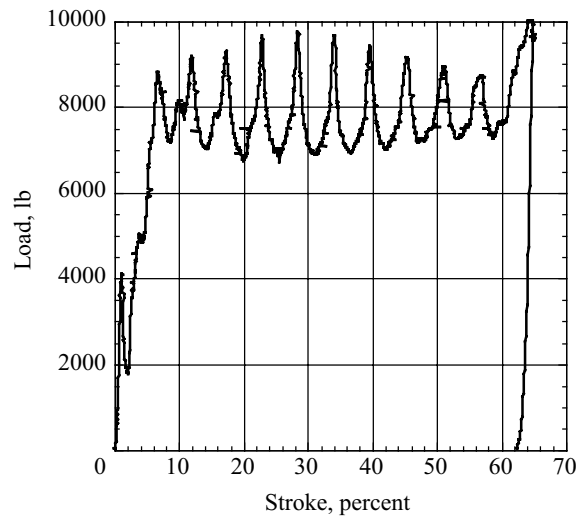
The nose gear was modified to absorb more energy by removing the internal hydraulic components and replacing them with a honeycomb canister. This modification was intended to increase the available stroke and to produce a uniform crushing load. The 13.5-in-high canister consisted of two concentric



(a) Reinforced honeycomb.



(b) Energy-absorbing canister.



(c) Load versus stroke response of energy absorber.

Figure 6. Nose gear energy-absorbing canister and static load versus stroke curve.

aluminum tubes, filled with aluminum honeycomb, each having a wall thickness of 0.0625 in. The inner and outer tubes had diameters of 2.0 and 2.75 in., respectively. To increase the crushing strength, plastic straws were inserted into the cells of the honeycomb that filled the inner tube, as shown in figures 6(a) and (b). The region between the outer and inner aluminum tubes was filled with honeycomb without additional reinforcement. The canister was fabricated in 6-in. segments corresponding to the thickness of the available honeycomb material. Brass end plates were placed between the honeycomb sections. The energy-absorbing canister was designed such that the diameter of the outer aluminum tube was smaller than the diameter of the inside wall of the landing gear, thus permitting the canister to deform freely and buckle without applying high loads to the inside wall of the landing gear. The crushing load was determined from compression tests performed on 6-in-high samples, and the results of these tests are shown in figure 6(c). The crushing load was uniform and the average value was approximately 8000 lb, which is slightly lower than the expected failure load of the gear.

To maximize the energy absorption even further, a disk of 6-lb/ft³ Confor™ rate sensitive polyurethane foam was used in the tire. A solid steel rod was inserted through the original hollow axle to

strengthen the axle. However, even with these modifications, the nose gear could only absorb a small percentage of the energy that the original gear was designed to absorb. For example, assuming the honeycomb stroked 12 in. at 8000 lb, the modified nose gear would remove 96 000 in-lb of energy compared with 700 000 in-lb for the original gear.

The main landing gears were also modified for the test. The ground resonance damper was missing from this helicopter. The damper hydraulically couples the left and right main landing gears to move in opposite directions (± 1 in. from the neutral position) (ref. 11). Rigid extension and retraction spacers were installed to place the ground resonance stage of the landing gears in its middle, or neutral, position. Two shear pin sets were used in the landing gear design: an upper set of two pins and a lower set of four pins. The upper set protects the honeycomb from being crushed until after full oleo stroke (12 in.). The upper pins must shear before any crushing of the honeycomb stage can occur, and the lower pins fail after the honeycomb crushes approximately 1 in. Dynamic tests of the landing gear components showed that the total load of the combined honeycomb crushing and lower pin shearing could cause a high transient load of over 40 000 lb (ref. 11). Because the attachment points failed during the 1987 test, three of the four lower shear pins were removed from the landing gear to reduce the potential for creating high transient loads. The two large shear pins, which are used to protect the honeycomb in low sink-rate crashes, were left in the landing gear.

In the 1987 test, failures of the gear strut and drag beam attachments occurred. The main struts had hollow trunnion pins with a diameter of 1.0 in. These pins were designed for quick removal of the strut and could pull out of the bulkhead attachment bushings if the strut was twisted or sheared. For the 1999 test, the hollow pins were replaced with longer solid steel pins with threads, washers, and hex nuts on the formerly free end. The retaining nuts and washers were located on the outer side of the main landing gear bulkheads. These washers increase the pull-through resistance of the attachment pins. Two 1.125-in-diameter pins, used to attach the drag beam to the fuselage, were replaced with a single 17-in-long, 1.125-in-diameter rod that was threaded on the ends and installed as shown in figure 7. In the 1987 test, failures of the drag beam lug and main gear attachment fittings stopped the crushing of the

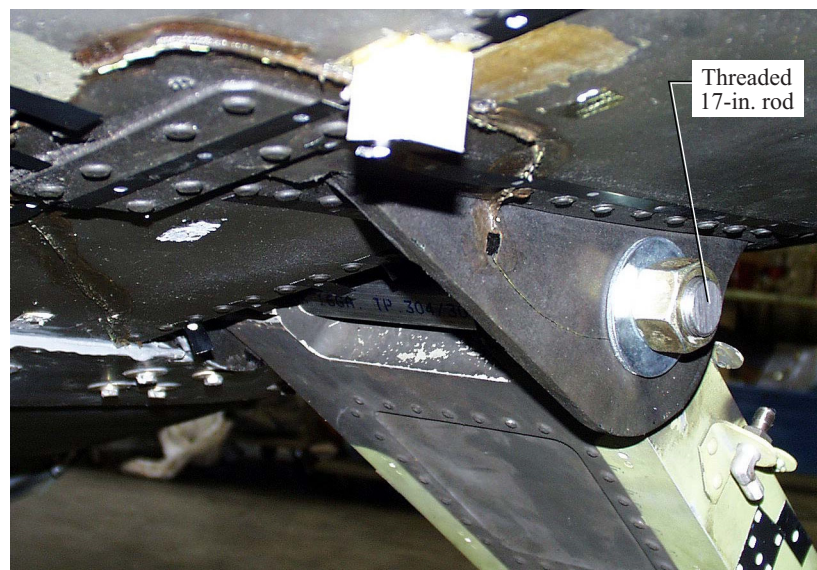
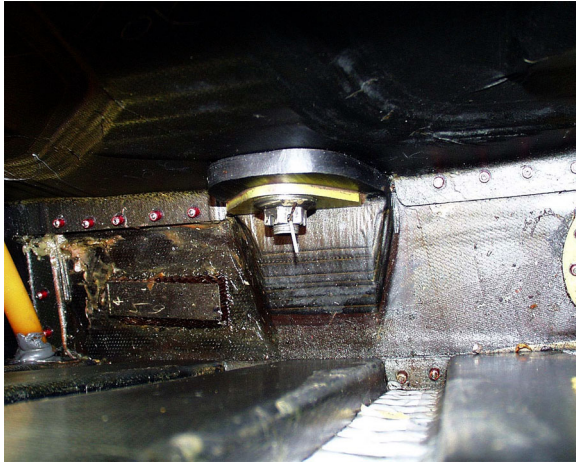
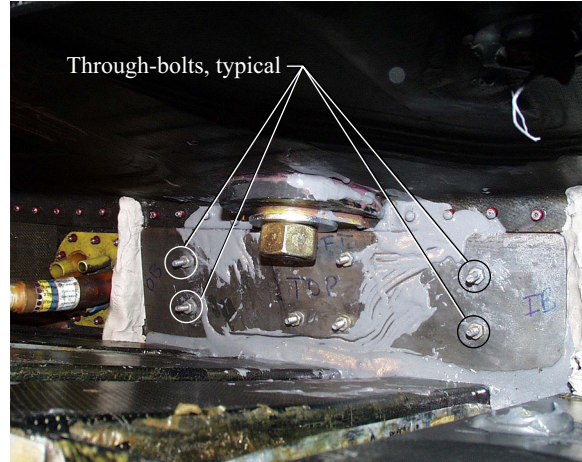


Figure 7. Main landing gear drag beam modification.



(a) Original configuration.



(b) Modified configuration.

Figure 8. Main landing gear attachment lug before and after reinforcement.

honeycomb canisters. A tube was placed around the bolt (1.25-in. inner diameter, 6.5 in. long) between the drag beam lugs to allow both airframe lugs to share any shear load applied to the drag beam. The inboard airframe attachment lugs that failed in the 1987 crash were also reinforced, as shown in the photographs of the original and modified configurations in figure 8. This lug was reinforced by filling the interior area with epoxy and by sandwiching the lug flange with interior and exterior steel plates. Eight through-bolts, shown from the inside of the airframe in figure 8, were used to hold the plates together. These changes were made to keep the main gears attached and functioning as designed.

2.5. Seats, Anthropomorphic Dummies, and Associated Instrumentation

A 50th percentile Hybrid II anthropomorphic test dummy (ref. 14), weighing approximately 170 lb, was used to represent the pilot (right front crew position). The 50th percentile designation indicates that the dummy represents the median height and weight specifications for the average adult male occupant. The dummy was instrumented with triaxial accelerometers located in the head, chest, and pelvis. A lumbar load cell was installed to measure the spinal compressive force. Additional load cells were used to measure the force in the lap and shoulder belts. The pilot was placed in a used commercial military-qualified helicopter seat provided by the United States Army Aeromedical Research Laboratory (USAARL). This seat contained two invertube energy absorbers. New MA-16 inertia locking reels were used with lap and shoulder belts to restrain the dummy during the test. Accelerometers were mounted to the seat pan to measure forward and vertical acceleration. Triaxial accelerometers were located on the floor near the point of seat attachment to the seat rail.

The USAARL supplied a fully instrumented modified 50th percentile Hybrid III dummy (refs. 14 and 15) with a self-contained data acquisition system (DAS) for the copilot (left front crew position). This dummy weighed approximately 198 lb and was the only dummy to be outfitted with a helmet for the test. The modifications to the dummy include an internal DAS incorporated into the pelvis as well as a unique spine. The rigid spine box of the Hybrid III was replaced with a flexible spine consisting of rubber disc segments between each rib level as well as two torsional joints. The head of the Hybrid III dummy was replaced with a Hybrid II head for better representation of the anthropometry features and a more compatible helmet fit.

The self-contained DAS was used to collect data for the copilot dummy, including head accelerations in three directions, T-1 thoracic accelerations in three directions, head pitch rate, C-1 cervical head and neck forces and moments, T-1 thoracic forces and moments, torso sternum accelerations in two directions, and lumbar forces and moments. The T-1 thoracic accelerometers were located at the base of the neck, and the torso sternum accelerometers were located in the front of the chest at the mid-sternum level. Two accelerometers were mounted to the seat pan to measure forward and vertical acceleration, and triaxial accelerometers were located on the floor near the seat attachment to the seat rail. Load cells were installed to measure the dynamic forces in the lap and shoulder belts. In all, the self-contained DAS collected 29 channels of data at 10000 samples per second. The copilot dummy was secured in a used commercial military-qualified helicopter seat of a different design than the pilot seat. This seat contained six “torshock” energy absorbers. An MA-16 inertial locking reel was used in conjunction with the restraint system to constrain the dummy during the test.

The rails for the crew seats had rear longitudinal adjustment holes. Because the fore-aft adjusting pin for the crew seats used in this test was located at the front leg, holes were drilled in the front rail at the average longitudinal location. The seats were also adjusted to the middle vertical positions to allow a maximum vertical stroke of approximately 14.5 in. The seat pan would contact the flexible seat well bottom at a stroke of 13.5 in.

Two ceiling-suspended troop seats with wire-bender energy absorbers were mounted in the rear cabin area. New wire-bender energy absorbers were installed in the troop seats; however, these seats had previously been used in active aircraft and the seating material was in poor condition. The seat pan consisted of a canvas cloth that was worn and oil-stained. Hybrid II 50th percentile anthropomorphic dummies, each weighing approximately 170 lb, were used to represent the right and left troop occupants. Both dummies were instrumented with triaxial accelerometers located in the chest. One accelerometer was mounted to the rear frame of the seat, and two accelerometers were attached to the floor near the troop seats.

2.6. Ballast Weight and Center of Gravity

Ballast weights were added to the aircraft to represent the engines and fuel. The left and right engines were represented with two 25-in-long steel tubes (each weighed 250 lb and had a 12-in. outer diameter and 7/8-in. wall thickness) welded to a steel cradle attached at eight of the original engine attachment points. A 37-in-long (2- by 3-in. cross section) steel bar was welded across the top of the steel tubes. An eyebolt was attached to the steel bar at the centerline of the helicopter for use as a pullback hard point. The entire one-piece assembly represented both engines and weighed 630 lb. Equal amounts of water were added to the left and right fuel tanks to simulate the 1610-lb weight of a full tank. The water filled each tank approximately 80 percent by volume. All four doors, the engine cowling, and the cockpit center console were removed from the aircraft for the test. The rotor head and attached rotor blade masses were present when the helicopter was received. The aircraft weighed 7832 lb in its test configuration. The center of gravity (CG) was measured at FS 198 and BL 0. The vertical CG location was estimated to be at WL 100 based on differences in jack point loads with the aircraft pitched at two attitudes (-0.48° and 1.13°). Note that the vertical CG is difficult to determine accurately due to the small angles involved in the test technique. The manufacturer’s targeted CG location is FS 204, BL 0, and WL 97 (ref. 10).

2.7. Instrumentation and Data Acquisition

Forty-three accelerometers were installed on the airframe, the main and nose landing gears, and the large mass items such as the rotor transmission and engines to measure the dynamic structural response of the helicopter. The accelerometers were oriented in directions perpendicular and parallel to the floor

along the helicopter coordinate system. The vertical accelerometer direction is in the helicopter body axis system and is perpendicular to the fuselage floor. The locations of some of the accelerometers on the structure are shown in figure 9. In addition, 11 string potentiometers (displacement transducers) were installed: 5 on the landing gear and 6 in the subfloor to measure subfloor crushing. A list of all instrumentation is provided in table A1 in the appendix.

The data signals from the individual transducers were routed to a junction box that was attached to an umbilical cable. The umbilical cable ran vertically to an elevation of 220 ft, down a gantry leg, and into the control room located approximately 120 ft north of the impact site. The total length of the umbilical cable was approximately 800 ft. The unavoidably long length of the cable increases the possibility of electrical anomalies in the data. The data were acquired at 10000 samples per second using a 12-bit resolution digital DAS. The data were split into three groups of 32 channels. The 32 channels within a group were sampled simultaneously. To rectify the phase shift between groups, one channel from each group was used to record a common square wave signal.

The crash was recorded on film with 13 high-speed 16-mm instrumentation cameras. These cameras recorded the crash at a nominal rate of 400 frames per second, and each camera was equipped with a 100-Hz timing light generator that generated timing marks on the edge of the film for determining the exact camera filming speed. Ten cameras covered the crash from different ground directions, as indicated in figure 10. Three cameras were mounted onboard with two of these cameras recording motion of the crew seats from the rear of the aircraft. The third onboard camera covered the front of both crew occupants with a fish-eye lens. The three onboard cameras were 28-volt DC powered models, and the ground cameras were AC powered models. Color negative film (ASA 250 daylight) and a 160° shutter were used in the cameras.

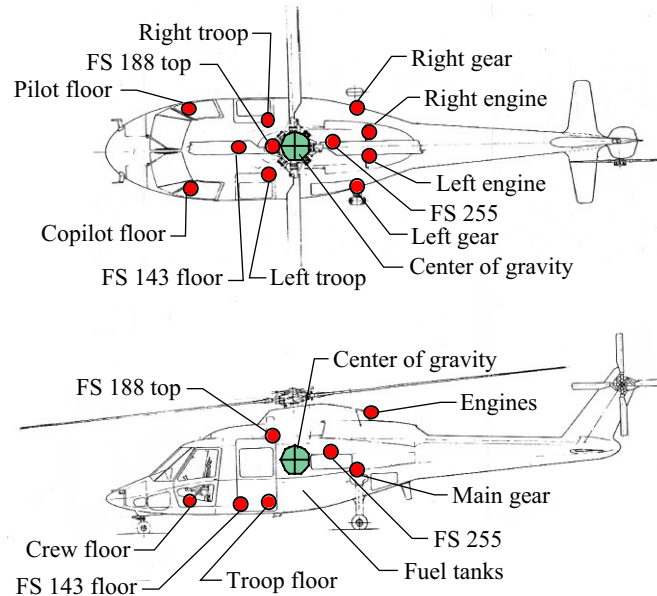


Figure 9. Selected accelerometer locations on the airframe structure.

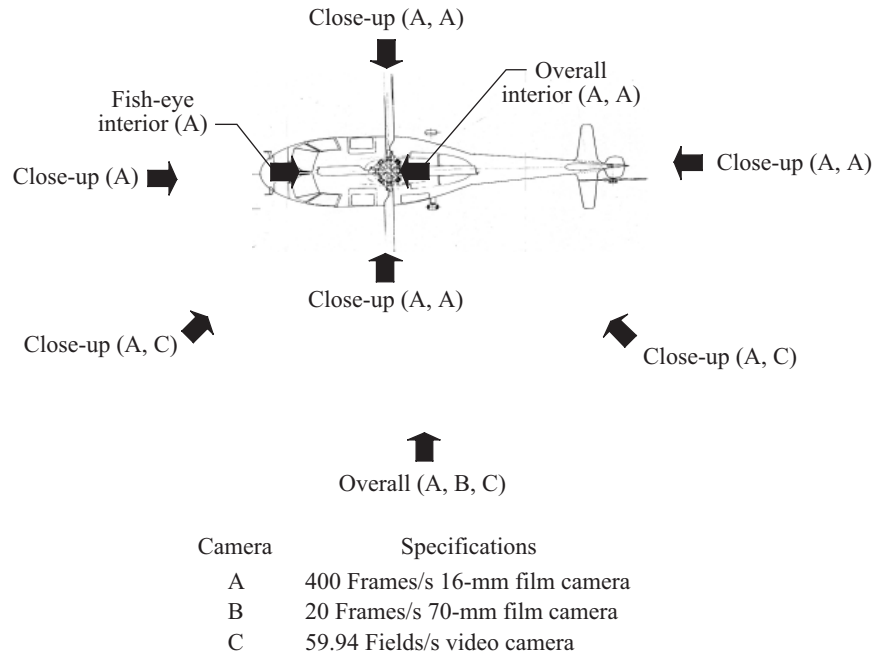


Figure 10. Schematic of the camera locations (not to scale).

2.8. Ancillary Experiments

In addition to obtaining test data for validating the nonlinear transient dynamic crash simulation, two ancillary experiments were performed. A programmable electronic crash sensor unit (ECSU) was mounted on the cabin floor at FS 170, WL 58, and BL 0 near the troop seats. The sensor was typical of the kind that might be used to fire an airbag. For this test, the ECSU was wired to turn on a light as an initiation indicator. The objective of this ancillary experiment was to determine if the ECSU functioned properly during an actual crash environment.

Two pressure transducers were installed in both the left and right fuel tanks to measure the hydrodynamic pressures during impact. The four pressure transducers with their fixtures are shown in figure 11. The bottom fixtures were used in place of the bottom plug to obtain data from the lowest fuel point. Pressure transducers were mounted at an intermediate depth with the L-shaped fixture that was attached to the fuel tank cover panel. The bottom transducers were pointed up, and the mid-depth transducers were pointed to the rear of the aircraft. All internal hoses and gauges were removed from the helicopter fuel tank. The pressure data were obtained for correlation with a fluid-structure analysis to be performed as a follow-on simulation to evaluate the influence of the hydrodynamic pressure pulse on surrounding airframe structure.

2.9. Test Methods

The helicopter was suspended from the IDRF overhead gantry and tested by swinging it pendulum-style into an 8-in-thick concrete impact surface. A general diagram of the crash test method is given in figure 12(a) and a photograph of the IDRF is shown in figure 12(b). The planned vertical and horizontal impact velocities were 38 and 32.5 ft/s, respectively, and the planned impact orientation was 5° nose-up pitch with no roll or yaw. Two main swing cables and a main pullback cable initially supported the helicopter in the pullback or release position. A side view of the cable harness system is shown in

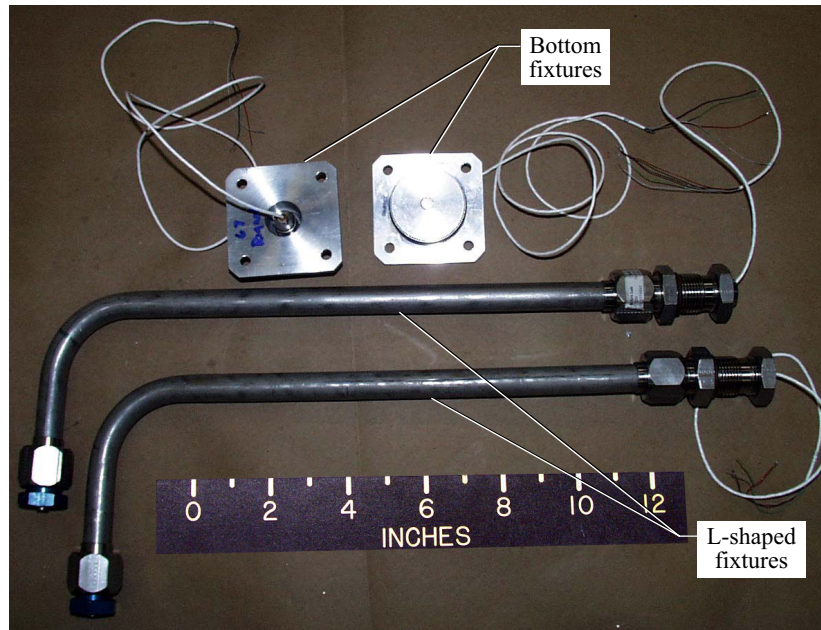
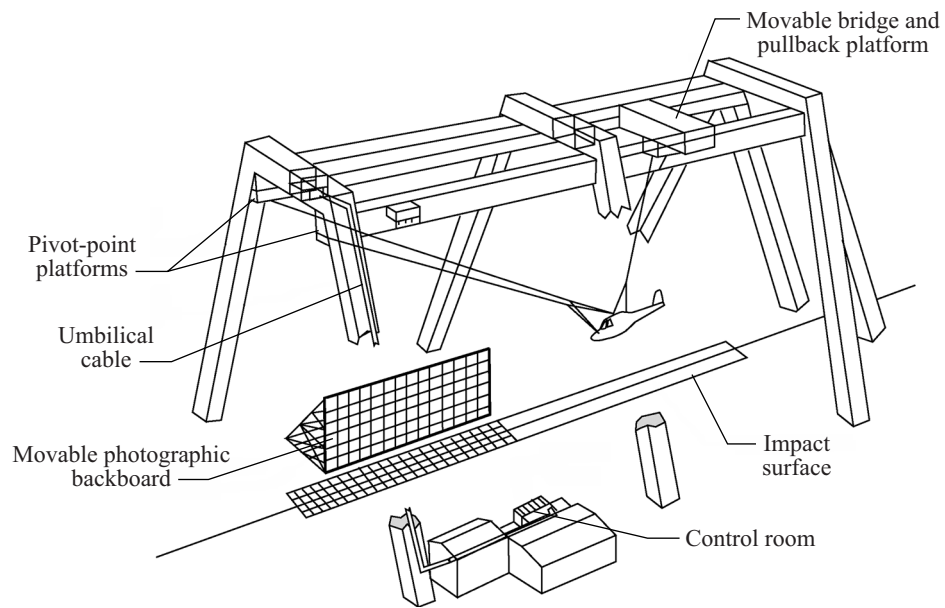


Figure 11. Fuel tank pressure transducers and mounting fixtures.

figure 13. A 15000-lb-capacity winch was used to pull back the helicopter to its release position. The two main swing cables and the main pullback cable each connected through a pear-shaped ring to harnesses attached to hard points on the helicopter. The hard points were located at the nose gear, rotor head, and engine. Because of the intended pitch-only test scenario, the lifting hard points were located on the helicopter centerline (BL 0). The left and right main swing cables each branched out to connect the nose and rotor hard points. The main pullback cable branched out to connect the engine and rotor hard point. The area between the harness cables encloses the CG of the helicopter. At the release position, the main swing and pullback cable extensions, shown as the dotted lines in figure 13, intersect the CG of the helicopter. The main swing cables are set to be perpendicular to the main pullback cable at the release point.

Sufficiently strong hard points had to be incorporated into the existing helicopter structure for lifting the airframe. A steel bar was welded to the two simulated engine masses, and an eyebolt was attached along the centerline. The nose lifting point required the most extensive modifications. The nose hard point was attached to the airframe at the nose gear trunnion axle, as shown in figure 3(b), and at the front bulkhead (FS 35). A top mounting plate and eyebolt that were provided to lift and move the helicopter were used as the rotor head hard point. The cable lengths were determined for the desired crash scenario, and then the helicopter was raised to the necessary drop height with the pullback winch. The swing dynamics, cable lengths, and cable loads were determined from rigid body simulations made by using the computer program Working Model 2D (ref. 16). Just before ground contact of the helicopter, the steel swing cables were severed with pyrotechnic cutters to allow free motion and slide. The details of this test procedure and simulation are described in reference 17. General full-scale crash test procedures are described in reference 7.



(a) Schematic of the IDR.



(b) Photograph of the IDR.

Figure 12. IDR gantry structure used to perform crash test of the ACAP helicopter.

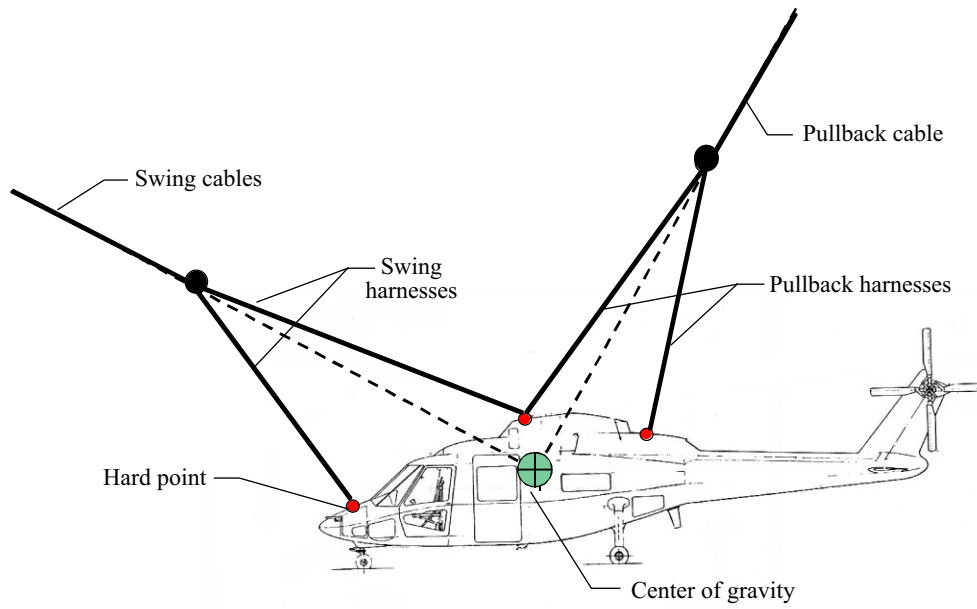


Figure 13. Side view of helicopter mounting system.

3. Summary of Test Results

A summary of the data obtained during the crash test of the Sikorsky ACAP helicopter is provided in this section of the paper. The data are presented in the following categories: sequence of events, acceleration time histories, fuselage deformations, hydrodynamic fuel tank pressures, seat responses, occupant responses, and injury prediction criteria. In this section of the report, only selected channels of the test data are presented to highlight the experimental findings. However, the complete set of unfiltered and, where applicable, filtered test data is included in the appendix. Additional information regarding the 1999 full-scale crash test of the Sikorsky ACAP helicopter can be found in reference 18.

3.1. Sequence of Events

The actual impact attitude of the helicopter (6.25° nose-up pitch and 3.5° left-down roll) was determined from analysis of the high-speed film of the crash test. The helicopter appeared to impact without yaw, but no overhead camera shots were available for confirmation. The swing cables change the helicopter's pitch as it falls. A pitching angular velocity of $9.6^\circ/\text{s}$ (increasing nose-up) at impact was measured from film analysis. This rotational velocity agrees with the value predicted by the Working Model 2D simulation. The film shows that the swing cables were pyrotechnically separated at 0.003 to 0.005 s before the left main landing gear tire made ground contact. The reference time ($t = 0.000$ s) was measured from left tire contact, and the impact orientation was determined at this time.

Motion picture analysis of the high-speed film from 10 exterior and 3 interior cameras and evaluation of the test data were used to determine the event times given in table 1. The film speed of each camera was determined from the 100-Hz timing marks. Eleven of the 13 cameras had film rates between 390 and 402 frames per second. For the other two cameras, one ran consistently at 450 frames per second, while the other camera ran inconsistently. The camera offering the sharpest image of the desired event was used for time determination. In cases where it was difficult to determine an exact time, two or more

Table 1. Airframe Crash Test Sequence

Event	Time, s
Left tire ground contact	0.000
Right tire ground contact	0.012
Left gear oleo maximum stroke (12 in.)	0.044
Right gear shear pin fails	0.045
Right gear oleo bottoms	0.054
Tail cone buckling initiation	0.064
Nose tire ground contact	0.069
Continuity gauge indicates tail cone separation	0.074
Fuselage contact	0.098
Left crew seat (copilot) stroke initiation	0.110
Right crew seat (pilot) stroke initiation	0.111
Left gear maximum honeycomb stroke (13.2 in.)	0.113
Right gear maximum honeycomb stroke (11.8 in.)	0.115
Right seat (pilot) maximum stroke (9 in.)	0.156
Left seat (copilot) maximum stroke (14.5 in.)	0.163
Tail cone ground contact	0.215
Helicopter comes to rest	1.97

camera times were averaged. The values given are only accurate to about 0.0025 s because of the 400 frames per second temporal resolution provided by the cameras. Times for some events such as tire contacts were easily determined within the limitation of the camera frame rate and image resolution. Other events such as fuselage contact were more difficult to determine because none of the cameras were mounted directly on the ground. Where possible, the test data were used to verify the timing of major events determined by the film analysis.

Images from the front and left-side cameras are shown in figures 14 and 15, respectively, beginning with initial contact and finishing after the major impact has occurred. The right gear tire impacted the ground 0.012 s after the left gear tire impacted, and the right gear oleo stroked the maximum (12 in.) at 0.01 s after the left. The honeycomb energy-absorbing stage began stroking immediately after the oleo stage completed its maximum stroke. The upper shear bolt heads could be observed separating in some of the films immediately before the honeycomb started crushing. The honeycomb continued to crush even after the fuselage contacted the ground, as shown in figure 14 and reported in table 1. In figure 16, the helicopter is shown in its final resting position after sliding forward 22 ft 9 in. from the point of impact.

3.2. Acceleration Time History Responses

All experimental and analytical acceleration data that are presented in the paper were filtered using a 60-Hz Butterworth low-pass digital filter to remove the high frequency ringing from the underlying crash pulse, except where otherwise noted. The filtering was performed forward in time, then backward in time to eliminate any undesirable phase shift. The 60-Hz cutoff frequency was chosen because it removes the high frequency oscillations from the data without any distortion in the integrated velocity response. Some of the data channels contained electrical anomalies, as discussed in the appendix. These anomalies can be generated by electromagnetic interference, cross talk between channels, inadvertent overranging of the instrument, nonlinearity caused by exciting the resonance frequency of the accelerometer, and overranging of the instrumentation caused by setting the voltage limits of amplifiers too low, etc. In some cases, filtering of the data can remove these electrical transients. However, filtering can often mask an anomaly, making it appear as real physical data.

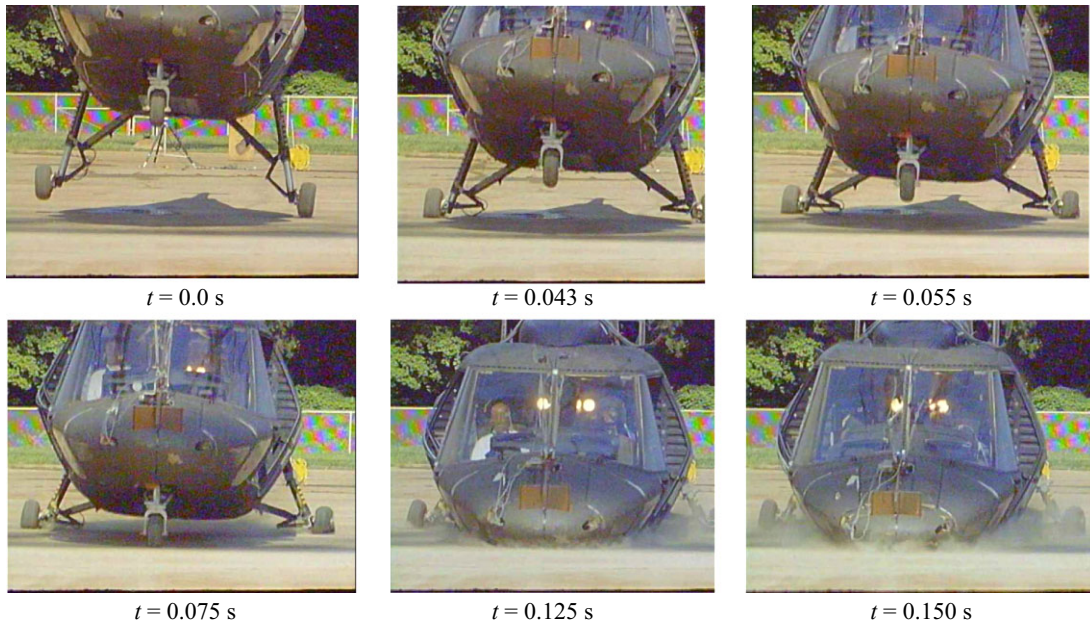


Figure 14. Front view images from a high-speed camera showing key events.

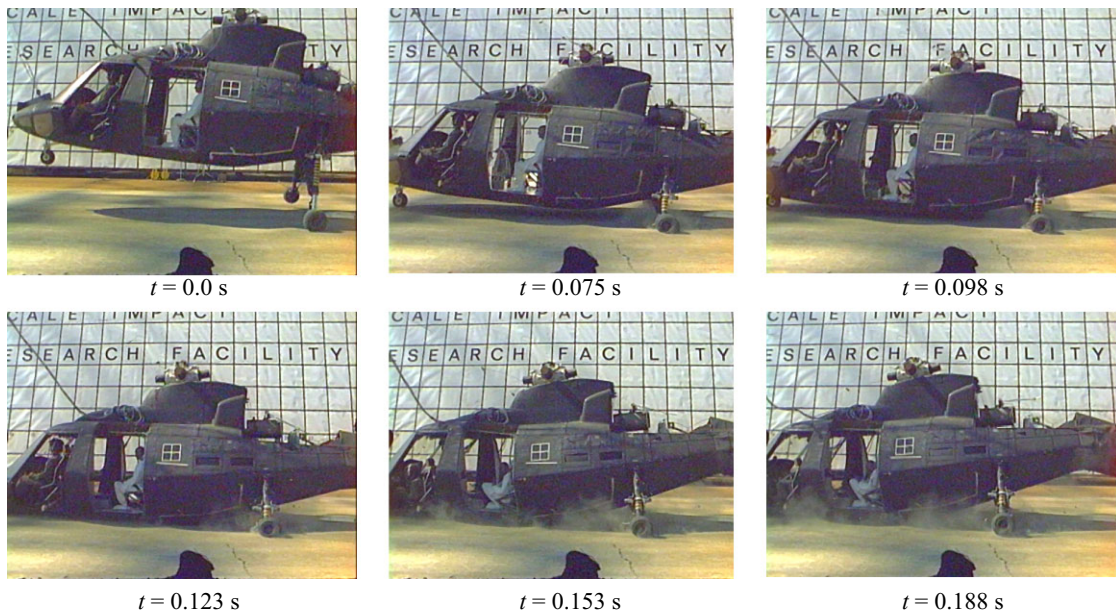


Figure 15. Left-side images from a high-speed camera showing key events.



Figure 16. Posttest photograph of the ACAP helicopter in the final resting position.

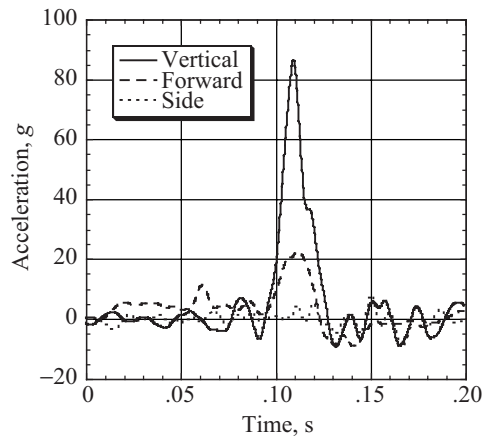
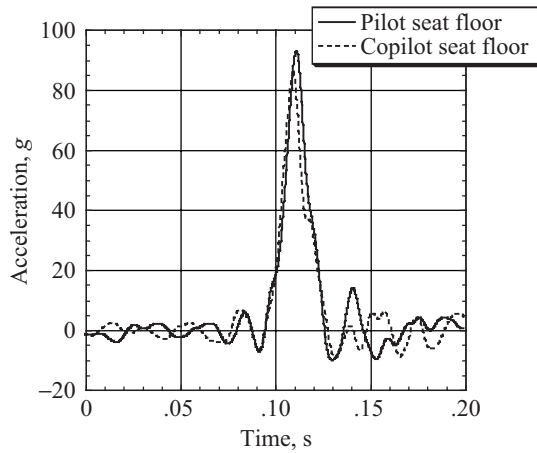


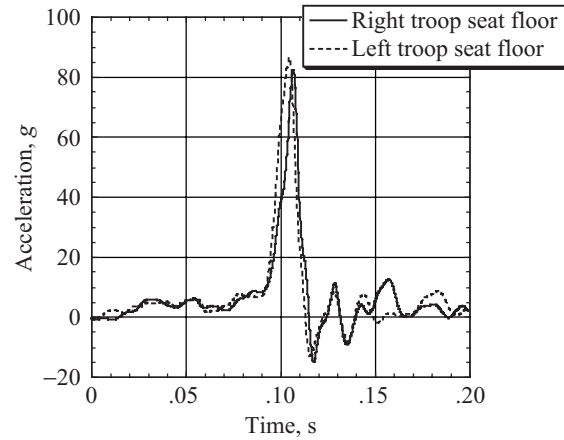
Figure 17. Filtered floor-level acceleration responses in three directions at the copilot position.

The triaxial acceleration responses measured at the copilot floor (FS 109, location shown in figs. 4 and 9) are shown in figure 17. The peak acceleration is four times greater in the vertical direction (up positive) than in the other directions. The forward acceleration peak indicates a slowing down (rear positive) as the landing gear contacts the ground. This rearward acceleration increases with fuselage contact with the concrete. The sideward accelerations are the smallest, and the direction oscillates towards the left and right side (right positive). Vertical floor-level acceleration responses are given in figure 18 at locations near the seat attachment points for the four anthropomorphic dummies. The peak floor accelerations are between 82 and 92g with the floor accelerations at the crew location slightly higher than the troop location. The time histories agree with the photographic crash events discussed in the previous section. During main gear stroking and before fuselage contact, the floor-level accelerations at the troop location (FS 186) are approximately 5g, whereas the floor-level acceleration responses at the crew location (FS 109) oscillate about 0g, as shown in figure 18. However, the acceleration responses at both positions increase rapidly after the fuselage bottom contacts the concrete at 0.098 s.

The differences in the crew and troop floor-level acceleration responses before fuselage contact may be attributed to the close proximity of the troop seats with respect to the main landing gear and the CG of the helicopter. As described previously, the helicopter has an induced pitch angular velocity of 9.6°/s upon impact. Thus, the initial velocity at every longitudinal location on the fuselage is different. The initial velocity can be determined for each location as the sum of the initial vertical velocity of the CG plus or minus the rotational component, which is the pitch angular velocity times the distance from the

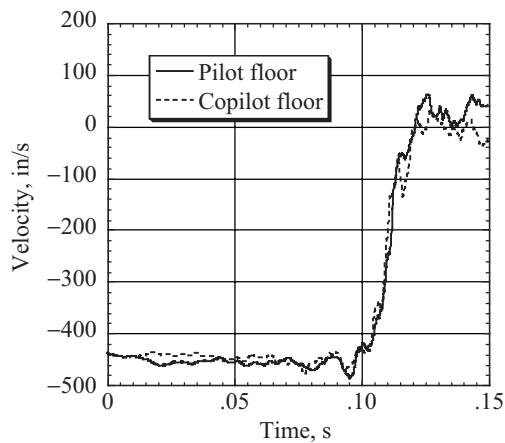


(a) Crew position.

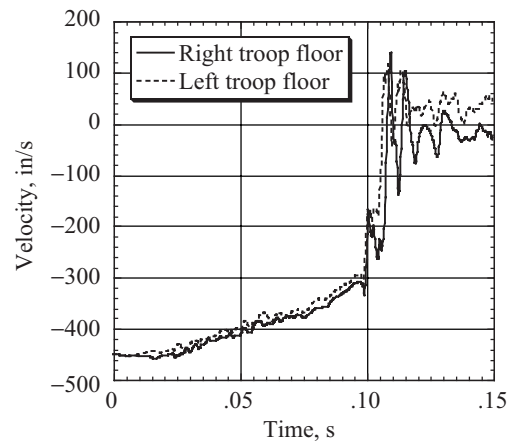


(b) Troop position.

Figure 18. Filtered vertical floor-level acceleration responses near the crew and troop occupants.



(a) Pilot and copilot floor.



(b) Right and left troop floor.

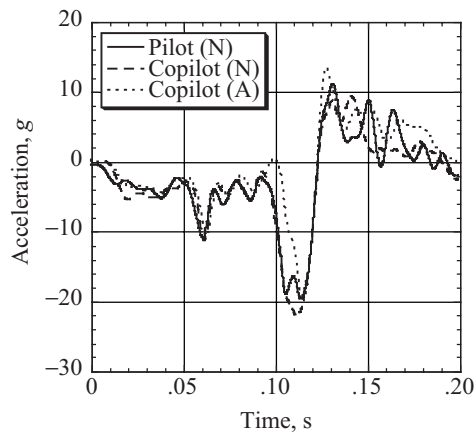
Figure 19. Floor-level velocity responses at the crew and troop locations.

accelerometer location to the CG. The troop seat attachment points are located close to the CG of the aircraft and just above the main landing gear. During main gear stroking, velocity is removed by stable crushing of the honeycomb canisters and a floor-level acceleration of approximately $5g$ is observed. Thus, at the time of fuselage bottom contact with the ground, a significant portion of the initial vertical velocity at the troop floor location has already been removed.

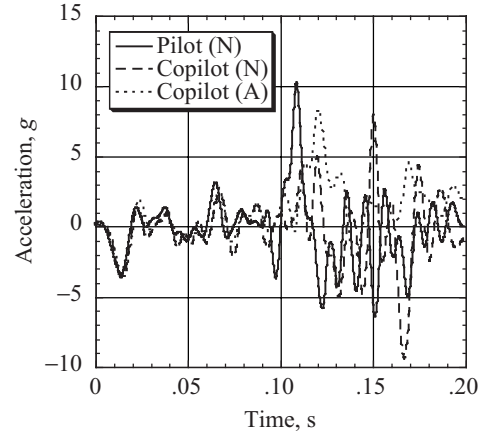
To illustrate this point, the raw acceleration data obtained from accelerometers located on the floor near the crew and troop seat attachment points were integrated to obtain the vertical velocity responses shown in figure 19. The initial velocity used in the integration at the troop location was -450.6 in/s, whereas the initial velocity at the crew floor location was -439.1 in/s. The initial velocities are different because the crew seat attachment points are located about 90 in. forward of the CG location. As a result, the velocity at that location at initial landing gear contact is lower than at the troop seat location. As shown in figure 19, the magnitude of the velocity response of the pilot and copilot floor increases slightly

for the first 0.1 s of the pulse, whereas the magnitude of the velocity response of the right and left troop floor is decreasing during the same time period. At the time of fuselage contact with the ground (0.098 s), the velocity at the pilot and copilot floor is approximately -460 in/s. The corresponding velocity of the right and left troop floor is -300 in/s. Thus, the right and left troop dummies benefited from the energy attenuation achieved from crushing of the aluminum honeycomb stage of the main landing gear. In contrast, the original energy-absorbing nose gear was missing from the ACAP helicopter and a modified civil helicopter nose gear was retrofitted to the airframe. The replacement gear was not designed to provide a high level of energy absorption and failed early upon impact after stroking 9 in.

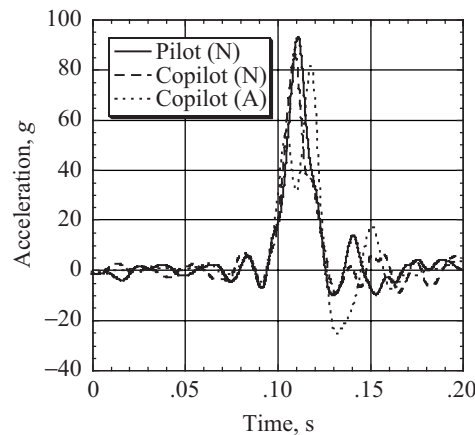
As described previously, accelerometers were installed to record floor-level acceleration responses in three directions using the self-contained DAS in the copilot dummy supplied by the USAARL. In addition, floor-level acceleration responses were measured near the seat attachment points for the pilot and copilot using the DAS from NASA. The filtered acceleration responses for these three locations are shown in figure 20. In the plots, (N) refers to the data recorded by the NASA system, and (A) refers to



(a) Forward acceleration responses.

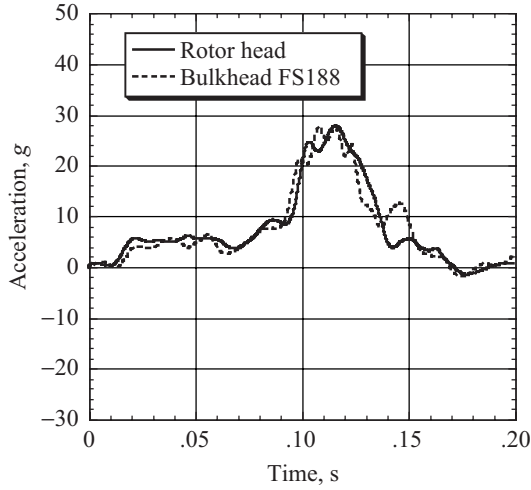


(b) Side acceleration responses.

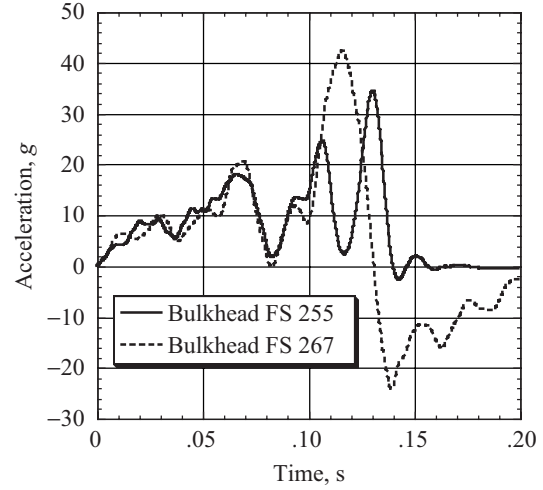


(c) Vertical acceleration responses.

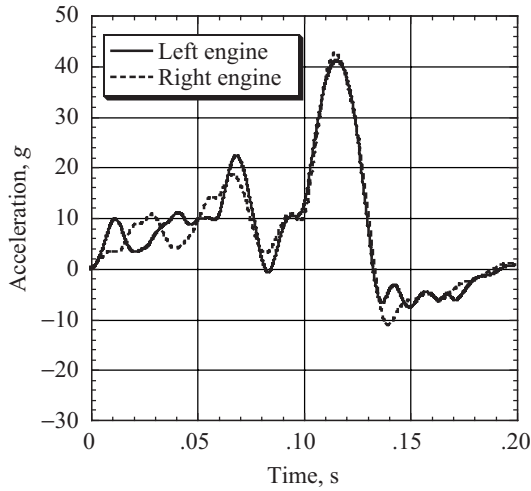
Figure 20. Filtered acceleration responses of the pilot and copilot seat floor as measured by the DAS from NASA and USAARL.



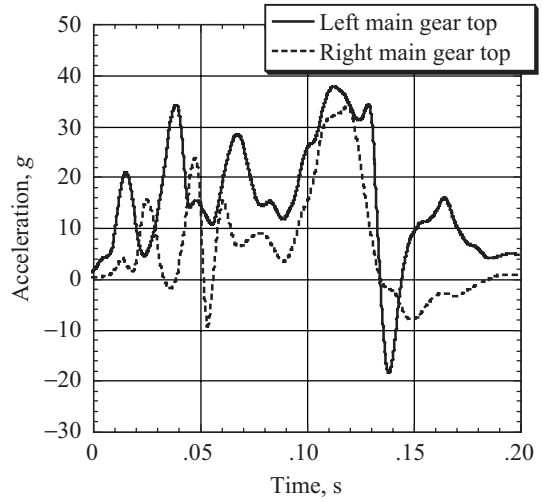
(a) Rotor head and top of the bulkhead at FS 188.



(b) Bulkheads at FS 255 and 267.



(c) Left and right engine.



(d) Top of left and right main landing gear.

Figure 21. Filtered vertical acceleration responses at several locations on the ACAP helicopter.

data recorded by the USAARL system. The floor-level acceleration responses are similar, even though the accelerometers were not mounted in exactly the same location on the floor and the signals were recorded on two different data acquisition systems. These results provide confidence in the quality and validity of the experimental data.

The vertical acceleration responses for several locations on the helicopter airframe are shown in figure 21, including the rotor head (FS 200), the left and right engine (FS 264), the top of the left and right main landing gears (FS 261), and several bulkhead locations. In general, the data indicate that similar responses are obtained from accelerometers located close to one another. For example, the vertical acceleration response of the rotor head has the same shape, magnitude, and pulse duration as the response obtained from the accelerometer located at the top of the bulkhead at FS 188, as shown in figure 21(a).

The vertical acceleration peak values and times are given in table 2, and the vertical acceleration peaks at different helicopter locations are shown graphically in figure 22. When two accelerometers were located at the same FS and WL position, the two BL location values were averaged. The vertical accelerations are highest at the landing gear hubs and are lowest at the tail. The peak accelerations of the overhead masses are much smaller than the floor-level accelerations. This finding is expected because the overhead masses are relatively large and have a greater stopping distance available.

Table 2. Peak Vertical Acceleration Values and Corresponding Times at Different Locations

Accelerometer	Peak acceleration, g	Time, s	FS	WL	BL
Tail rotor mass	19	0.056	480	100	0
Bulkhead FS 188	28	0.108	188	115	0
Rotor head	28	0.117	200	160	12
Copilot seat pan	33	0.112	109	70	-20
Right gear top	34	0.118	261	110	50
Bulkhead FS 255	34	0.130	255	102	0
Left gear top	37	0.113	261	110	-40
Pilot seat pan	41	0.112	109	70	20
Left engine	41	0.115	264	130	-18
Bulkhead FS 267	42	0.117	267	102	0
Right engine	43	0.115	264	130	18
Floor FS 182	65	0.107	182	58	20
Right troop seat floor	83	0.107	176	58	20
Left troop seat floor	87	0.105	176	58	-20
Copilot seat floor	87	0.109	109	58	-30
Nose gear top	88	0.097	54	80	0
Pilot seat floor	92	0.111	109	58	30
Right gear hub	105	0.017	261	37	40
Left gear hub	120	0.008	261	37	-50
Nose gear hub	163	0.079	54	37	0

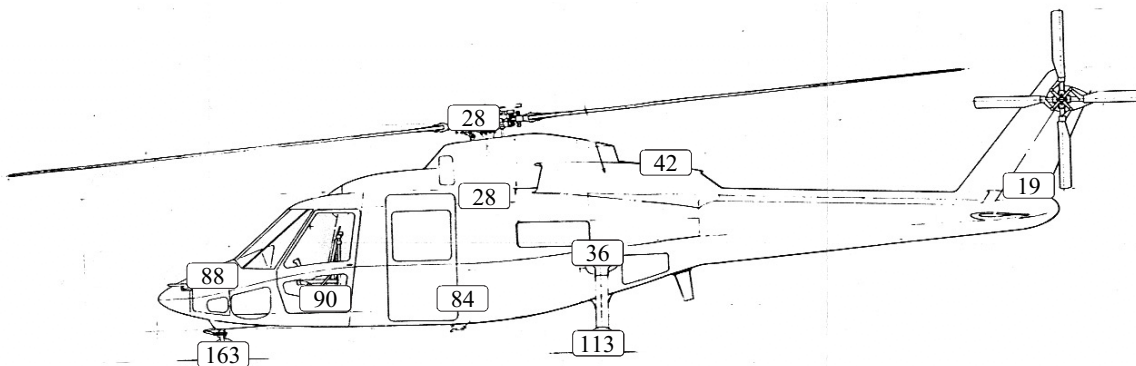


Figure 22. Vertical acceleration peaks (g) on the helicopter. Note that left and right side numbers are averaged.

3.3. Fuselage Deformations

The lower Kevlar™ subfloor keel beams and bulkheads were crushed as shown in figure 23, which features the intersection of the FS 143 bulkhead and the left inboard keel beam at BL 8. The crushing was mainly confined to the 4-in-high Kevlar™ portion that was designed for energy absorption. Only at cabin location FS 122.62 did the upper graphite channel of the subfloor crush. These graphite beams were mainly centered between the inboard keel beams. Crushing was observed in the lower bulkheads (FS 123, 143, 175, and 188) and in the lower left and right inboard keel beams (BL 8). No deformations were observed in the outboard keel beams (BL 25), which are approximately 1.75 in. higher and considerably thicker than the inboard keel beams. Unfortunately, the string potentiometers did not function properly and no transient displacement time histories for subfloor crushing are available. Sixty-three holes were drilled in the floor, and depth measurements to the inside skin were made before and immediately after the crash. The holes were sufficiently small to not adversely affect the structural response of the floor. The cabin floor bowed upward in the center after impact. The deformations from these measurements were generally below 1 in. Posttest measurements were taken with the upper floor removed, but the helicopter had been moved from the crash site and placed on a cart. These measurements reveal that the Kevlar™ subfloor deformations ranged from about 0.25 in. at the center rear of the cabin (FS 188) to about 1.5 in. at the center of the floor at FS 143.

Damage to the roof frames occurred in the cockpit area only (FS 105). Failure also occurred in both transmission supports at FS 188 and 215. The side frames (FS 143 and 122) exhibited some damage. The controls closet, which is located between the crew seats at FS 122, had failures approximately 12 in. below the ceiling. Despite these failures, cockpit and cabin areas had a minimal loss of volume.

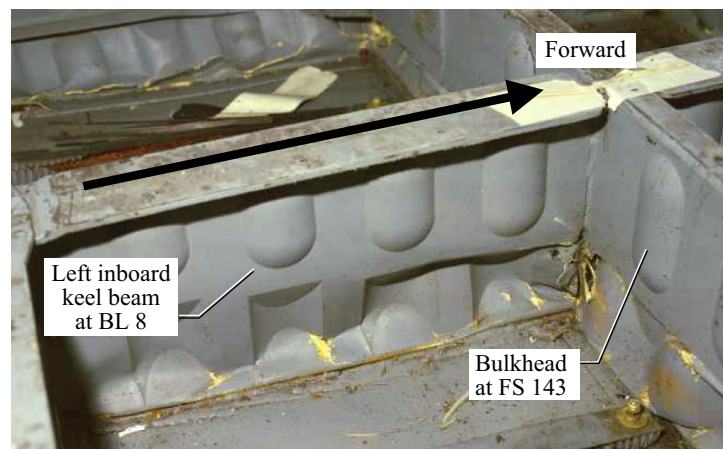


Figure 23. Posttest photograph showing subfloor deformations (FS 143 and BL 8).

3.4. Hydrodynamic Fuel Tank Pressures

The internal pressures were measured in each of the fuel tanks at the very bottom and at a mid-depth location. The bottom transducers, which were pointed upward, provided data only until fuselage contact with the ground, at which time the instrumentation wires were compressed and data were lost. The two mid-depth transducers were pointed aft and were 9.75 in. and 10.25 in. (left and right tanks) below the static level water surface. The pressure time histories recorded by the mid-depth transducers are shown in figure 24 for the right and left fuel tanks. Pressure responses between the right and left tanks showed

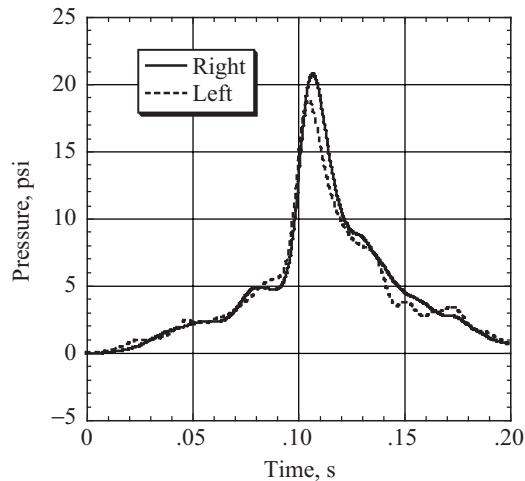


Figure 24. Mid-depth internal fuel tank pressures.



Figure 25. Posttest photograph of honeycomb canister halves from the modified nose gear.

little variation and these data are reasonable when compared with other reported fuel tank pressures (ref. 19). The pressure peaks occur at approximately the same time as the vertical floor acceleration peaks. The fuel tanks did not experience any leaks after the impact.

3.5. Landing Gear Response

Following the test, the honeycomb canister was removed from the nose gear and cut in half. A photograph of the crushed canister is shown in figure 25. The crushing of the inner tube, which was originally reinforced by inserting plastic straws into the honeycomb cells, is visible. The brass end plates, which were placed between the 6-in-long honeycomb sections, can be seen in the photograph. Posttest measurements indicated that the nose gear crushed 9 in. of the total 13.5 in. original height. The drag beam attachment of the nose gear failed during the test. Both of the main landing gears exhibited 12 in. of stroke in the oleo-pneumatic stages. Posttest measurements indicated that the crushable honeycomb

stages of the left and right gears stroked 13.2 in. and 11.8 in., respectively, of the 25-in. original height available. The modifications made to the main landing gears proved to be effective in allowing the gears to absorb the maximum amount of energy without premature fitting failures.

3.6. ECSU Response

In the test, the ECSU was located on the floor at FS 170, which is closer to the troop location than to the crew. Photographs from an interior film series are given in figure 26. The flash used as an initiation indicator in the ECSU experiment was very helpful in obtaining time synchronization between the exterior and interior cameras. The first indication of flash occurred at 0.063 s after initial tire contact. Because the filtered accelerations at the crew locations oscillate around zero and the velocity is relatively constant during this time interval, the crew station in this crash scenario would not be a good location for an ECSU that uses a change in velocity and filtered acceleration to initiate firing of an airbag.

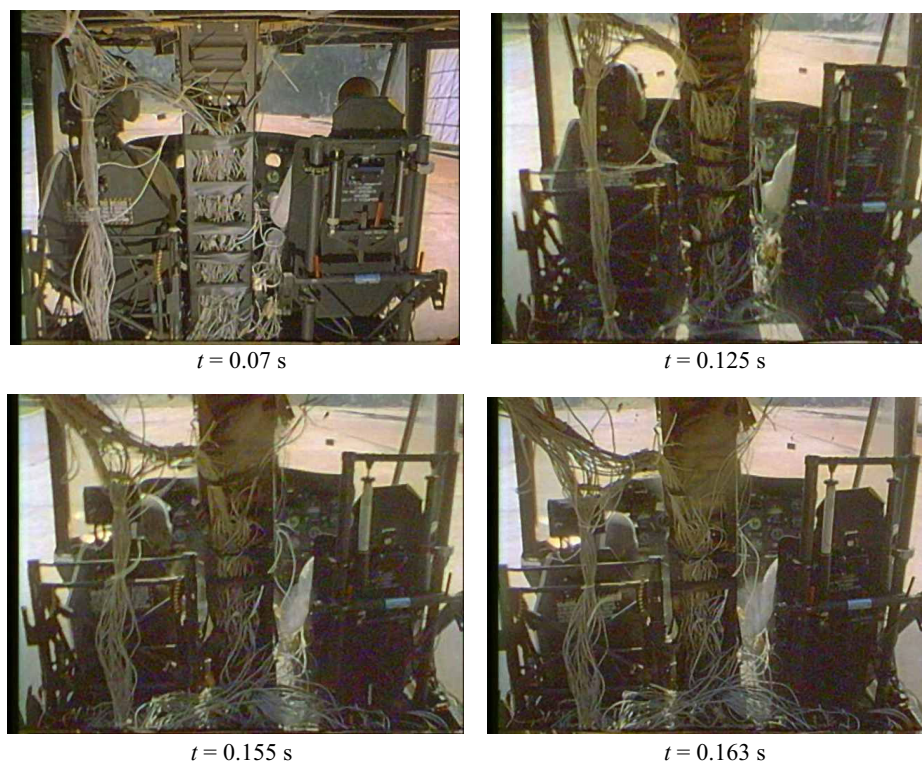


Figure 26. Interior rear view images of crew seats.

3.7. Seat Responses

The crew seats did not start stroking until after fuselage contact. The maximum downward motion of the pilot (right crew) occurred 0.182 s after initial contact, as shown in figure 27, which was obtained from the high-speed film. The slack and stretch in the restraint systems allowed the head and torso of both dummies to rotate forward. The MA-16 inertia reels were not manually locked before the test. After the test, both inertia reels were found locked.

Posttest measurements indicated that the pilot seat stroked approximately 9 in. of the total 14.5 in. available. The outboard pin attaching the pilot seat to the seat rail either was not properly engaged in the



Figure 27. Image showing maximum downward motion of the pilot (right crew) at 0.182 s after left tire contact.

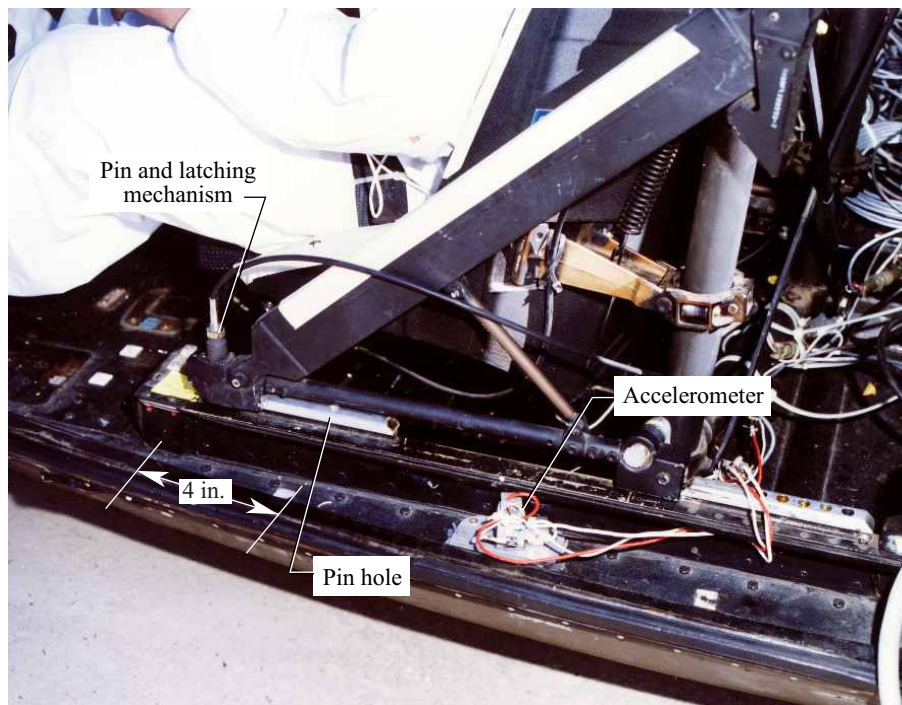


Figure 28. Posttest photograph of the unpinned pilot seat.

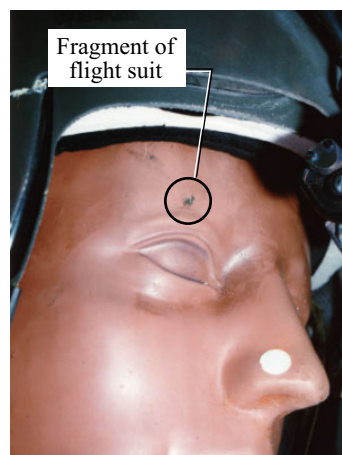
seat rail hole or came loose during the impact. Without the outboard pin restraint, the seat rotated inward about the remaining inboard pin and the seat pan struck the front seat well frame instead of stroking down into the well. The posttest position of the pilot seat is shown in figure 28. The pin moved approximately 4 in. forward of its original location.

A posttest photograph of the copilot dummy and left crew seat is shown in figure 29(a). During examination of the copilot after the test, a fragment of flight suit cloth was found on the right side of the dummy's forehead, as shown in figure 29(b). This discovery provides further evidence that the natural slack in the restraint system allowed the dummy's head to rotate over and strike its knee. The copilot seat essentially "bottomed out" with approximately 14.5 in. of stroke. In addition, there was evidence that the seat pan impacted the bottom of the seat well.

Posttest photographs of the right and left troop dummies and seats are shown in figure 30. The seat pan cloth was torn in both troop seats, allowing the buttocks of both dummy occupants to displace



(a) Copilot and seat.



(b) Close-up of copilot's face.

Figure 29. Posttest photographs of the copilot (left crew) dummy.



(a) Right troop.



(b) Left troop.

Figure 30. Posttest photographs of the right and left troop dummies and seats.

downward through the seat frame. As a result, the wire-bender energy absorbers exhibited minimal stroking. As shown in figure 31, the inboard wire-bender of the left troop seat stroked approximately 1 in., while the displacements of the other wire-benders were considerably less. During impact, a large downward deflection of the helicopter's roof at the wire-bender suspension location is shown in the high-speed film coverage. This roof deflection also limited the stroking of the wire-bender mechanism. The film indicates that the buttocks of the troop dummies may have contacted the cabin floor.

The vertical acceleration responses of the pilot floor, seat pan, and chest locations are given in figure 32(a). The pilot's energy-absorbing seat reduced the vertical acceleration peak from 93g on the floor to approximately 40g at the seat pan. The chest acceleration peak is slightly lower at 36g and is delayed

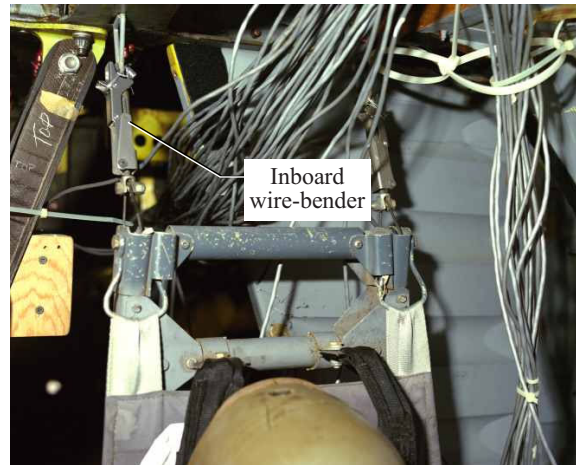
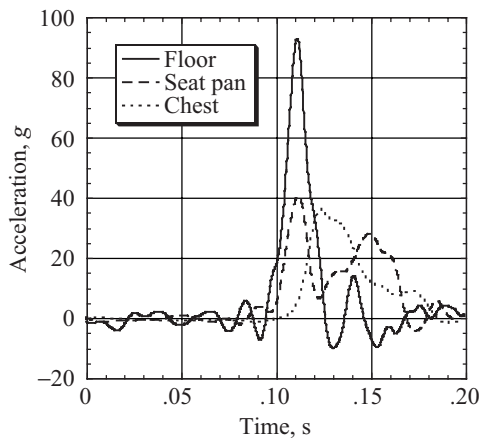
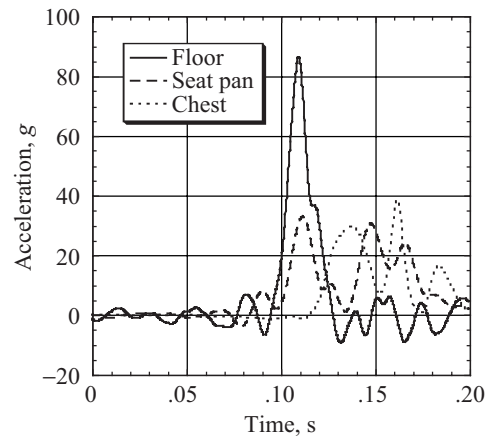


Figure 31. Posttest photograph of the inboard wire-bender mechanism of the left troop seat.



(a) Pilot acceleration responses.



(b) Copilot acceleration responses.

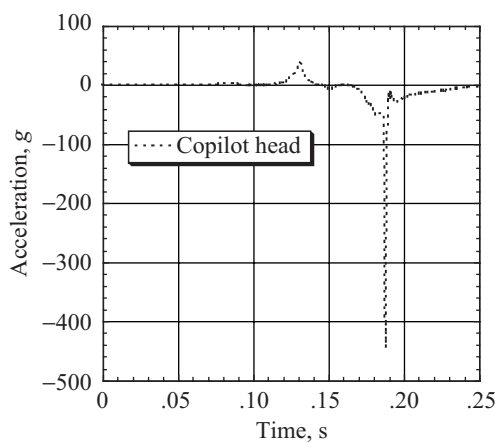
Figure 32. Filtered vertical acceleration responses of the crew floor, seat pan, and chest.

in time by about 0.01 s. The vertical acceleration time histories at the copilot floor, seat pan, and chest locations are plotted in figure 32(b). The copilot's energy-absorbing seat reduced the vertical acceleration peak from 85.6g on the floor to approximately 33g at the seat pan. The chest acceleration peak is of the same magnitude as the seat pan response, but is delayed in time by about 0.025 s. Thus, the peak acceleration of the pilot and copilot seat pans was 53g lower than the equivalent floor-level acceleration peak.

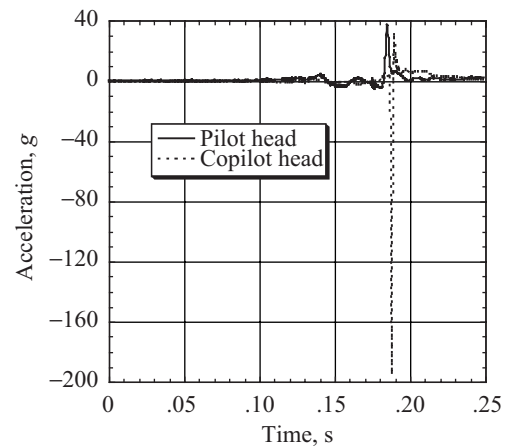
The crew seat pan accelerations are higher than desired for occupant survivability. As discussed previously, the original crashworthy nose gear was not available for this test. If it had been available, the combination of nose gear crushing plus seat stroke might have lowered these acceleration levels. The retrofitted standard nose gear that was used in the test did not provide sufficient energy attenuation and failed prematurely. The timing of events given in table 1 indicates that the pilot seat stopped stroking at 0.156 s, perhaps because of the seat well impact. The seat stroke stop time correlates with the second peak acceleration time for the seat pan response. This second peak acceleration (28g) is lower than the first (40g), which occurs while the seat is still stroking.

3.8. Occupant Responses

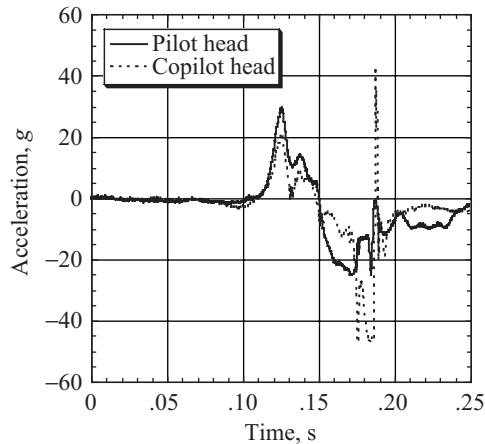
The head acceleration responses of the pilot and copilot dummies are plotted in figure 33 in the forward, side, and vertical directions. Only the copilot forward head response is shown in figure 33(a) due to anomalies in the pilot data. The acceleration data were filtered using a zero-phase low-pass digital filter with a cutoff frequency of 1000 Hz, which is the recommended filter for head accelerations according to SAE J211/1 (ref. 20). The acceleration responses indicate that the copilot experienced a high-magnitude, short-duration spike at 0.188 s during the pulse, as a result of a head strike. High-speed film coverage shows that at 0.188 s the copilot's head came in contact with his knees. A head strike is further indicated by a bit of green flight suit fabric that was found embedded in the forehead of the dummy slightly above the right eyebrow. The dummy's head most likely contacted the right knee. The film shows the head still moving downward between the knees for an additional 0.017 s before rebounding upward.



(a) Forward acceleration.



(b) Side acceleration.



(c) Vertical acceleration.

Figure 33. 1000-Hz filtered pilot and copilot head acceleration responses in three directions.

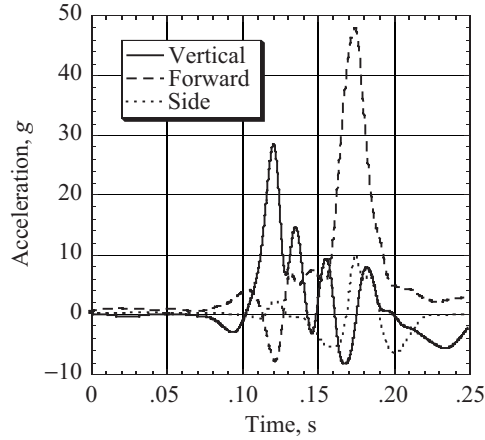
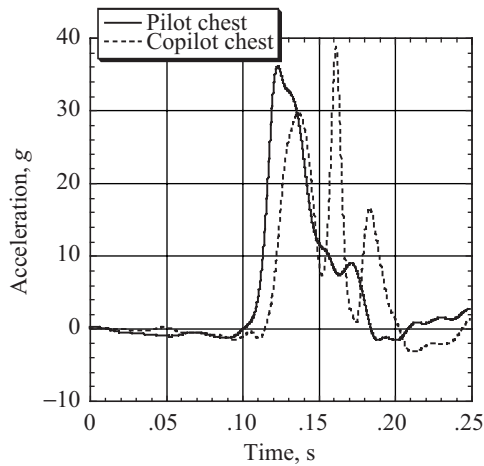
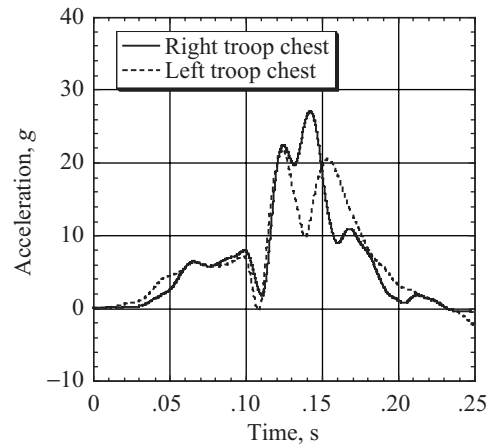


Figure 34. Filtered copilot T-1 thoracic acceleration responses in three directions.



(a) Pilot and copilot.

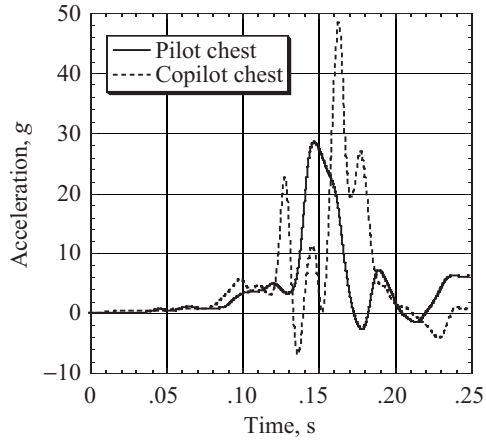


(b) Right and left troop.

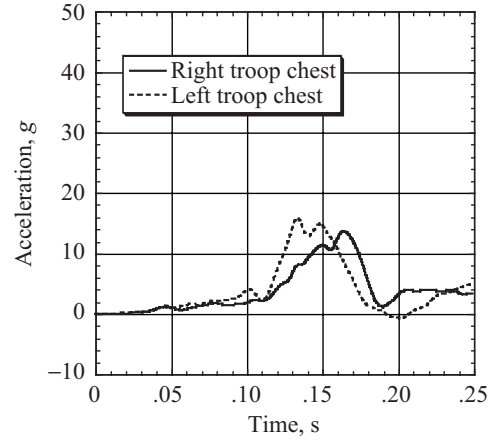
Figure 35. Filtered vertical chest acceleration responses of four dummies.

The filtered acceleration responses of the copilot torso are shown in figure 34 for the forward, side, and vertical directions. The T-1 thoracic accelerometers were located at the base of the neck of the copilot dummy. The pilot dummy was not instrumented at this location; consequently, no comparison with the copilot test data is possible. Unlike the head acceleration data, these data were filtered with a zero-phase low-pass digital filter with a cutoff frequency of 60 Hz. The effect of the head strike experienced by the copilot dummy is evident in the large 48g peak in the forward acceleration response shown in figure 34. In comparison, the peak vertical acceleration is 28g.

Plots of the vertical chest acceleration responses of the pilot and copilot, and the right and left troop dummies are shown in figure 35. In general, the pilot and copilot dummies experienced higher peak accelerations than the troop occupants. Plots of forward chest acceleration responses of the pilot, copilot, and the right and left troop dummies are shown in figure 36. Again, the pilot and copilot experienced significantly higher peak acceleration responses than did the troop dummies. Differences in the shape and



(a) Pilot and copilot chest.



(b) Right and left troop chest.

Figure 36. Filtered forward chest acceleration responses of four dummies.

magnitude of the pilot and copilot chest responses in both the vertical and forward directions are noted in figures 35(a) and 36(a). In general, the copilot data exhibit a noisier response with more oscillations than the pilot data. The variations cannot be attributed to differences in the vertical and forward floor-level pulses, which are shown in figures 18(a) and 20(a), respectively. The pilot and copilot seat pan acceleration responses have the same magnitude and overall shape, as well (see fig. 32). Therefore, the varying responses must be attributed to differences in the Hybrid II (pilot) and the modified Hybrid III (copilot) dummies.

The chest acceleration responses of the crew and troop dummies (shown in figs. 35 and 36) appear to be counterintuitive. The plots indicate that the troop occupants experienced lower forward and vertical chest acceleration responses than the crew occupants, even though the crew dummies were seated in energy-absorbing seats that exhibited between 9 and 14.5 in. of stroking and the troop seats had minimal stroking. The explanation for this behavior is that the troop dummies, which were located near the main landing gears, benefited from the energy attenuation achieved from crushing of the aluminum honeycomb stage. In contrast, the crew dummies were seated near the nose gear, which was a retrofitted standard gear that was not designed to provide a high level of energy absorption. In the crash test, the nose gear failed early upon impact after providing 9 in. of stroke.

The filtered acceleration responses of the pilot pelvis are shown in figure 37 for the forward, side, and vertical directions. The copilot dummy was not instrumented with pelvic accelerometers; consequently, no comparison with the pilot test data is possible. The filtered vertical seat pan acceleration responses of the pilot, copilot, and troop seats are shown in figure 38. Note that the data for the troop seats were obtained from accelerometers placed on the rear seat frame because the troop seats contained a canvas seat pan. The acceleration pulse shapes are similar for the pilot and copilot seat pans and for the right and left troop seat frames.

The restraint systems of both the pilot and copilot dummies were instrumented to measure lap and shoulder belt loads. The lap and shoulder belt responses are plotted in figure 39. Only the pilot shoulder belt response is shown in figure 39(b) due to anomalies in the copilot data. The Federal Aviation Regulations (FAR 27.562(c)) specify that where upper torso straps are used for crewmembers, tension loads in

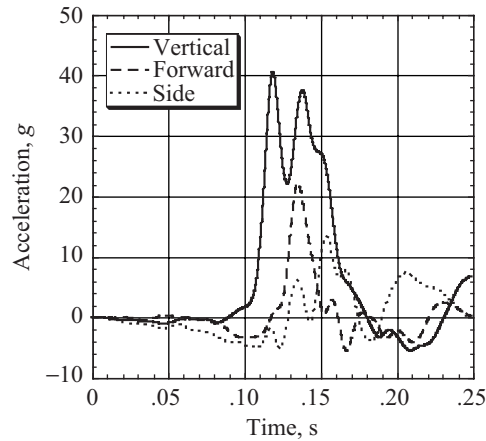
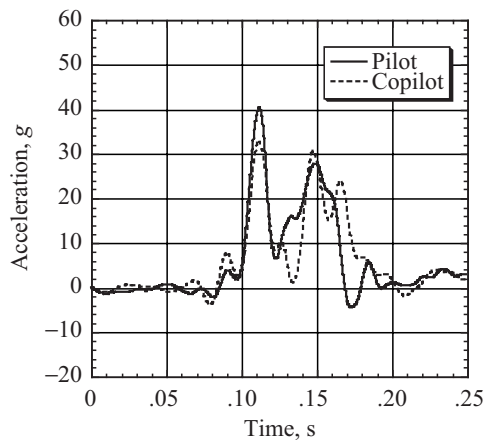
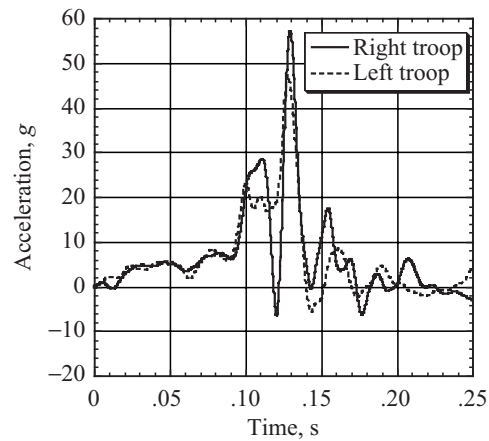


Figure 37. Filtered pilot pelvis acceleration responses in three directions.



(a) Pilot and copilot.



(b) Right and left troop.

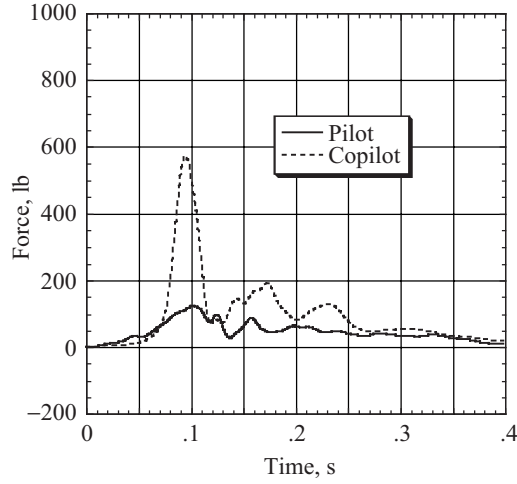
Figure 38. Filtered seat pan vertical acceleration responses.

individual straps must not exceed 1750 lb; if dual straps are used for restraining the upper torso, the total strap tension loads must not exceed 2000 lb (ref. 21). The restraint loads measured in the crew dummies did not exceed these limits. The troop restraint systems were not instrumented.

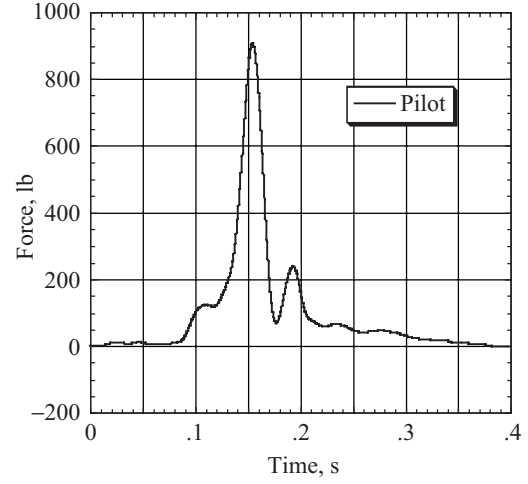
3.9. Injury Prediction Criteria

3.9.1. Dynamic Response Index

One commonly used injury prediction model is the Dynamic Response Index (DRI) (ref. 22). The DRI is derived from a simple one-dimensional lumped-mass spring damper system, as depicted in figure 40. This model was developed at the Air Force Wright Laboratory to estimate the probability of compression fractures in the lower spine due to acceleration in a pelvis-to-head direction, as might be



(a) Pilot and copilot lap belt.



(b) Pilot shoulder belt.

Figure 39. Restraint system loads for the pilot and copilot.

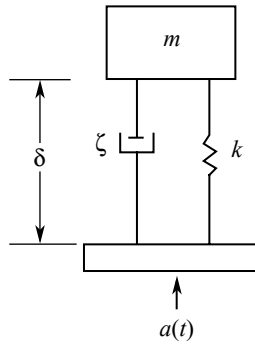


Figure 40. Schematic of the DRI spinal injury model; m is mass in lb-s²/in., ζ is damping ratio = 0.224, k is spring stiffness in lb/in., δ is deflection in inches, and $a(t)$ is input acceleration in in/s².

experienced by aircrew during ejection seat incidents. The DRI is calculated from the following equation, which is based on the schematic shown in figure 40:

$$\text{DRI} = \frac{\omega_n^2 \delta_{\max}}{g} \quad (1)$$

where δ_{\max} is the maximum deflection in inches, ω_n is the natural frequency equal to $\sqrt{k/m} = 52.9$ radians/s, and g is the acceleration of gravity equal to 386.4 in/s². Unfiltered vertical acceleration responses of the four seat pans were used as input acceleration, $a(t)$, to compute the DRI. The continuous DRI time histories for each occupant are shown in figure 41. The maximum DRI values (ranging from 22.3 to 30) for the crew and troop dummies are provided in figure 41. Operational data from ejection seat incidents indicate that the spinal injury rate for these DRI values is from 40 to well over 50 percent (see refs. 23 and 24). In fact, DRI values above 24 have not been correlated with either operational or cadaver spinal injury rate.

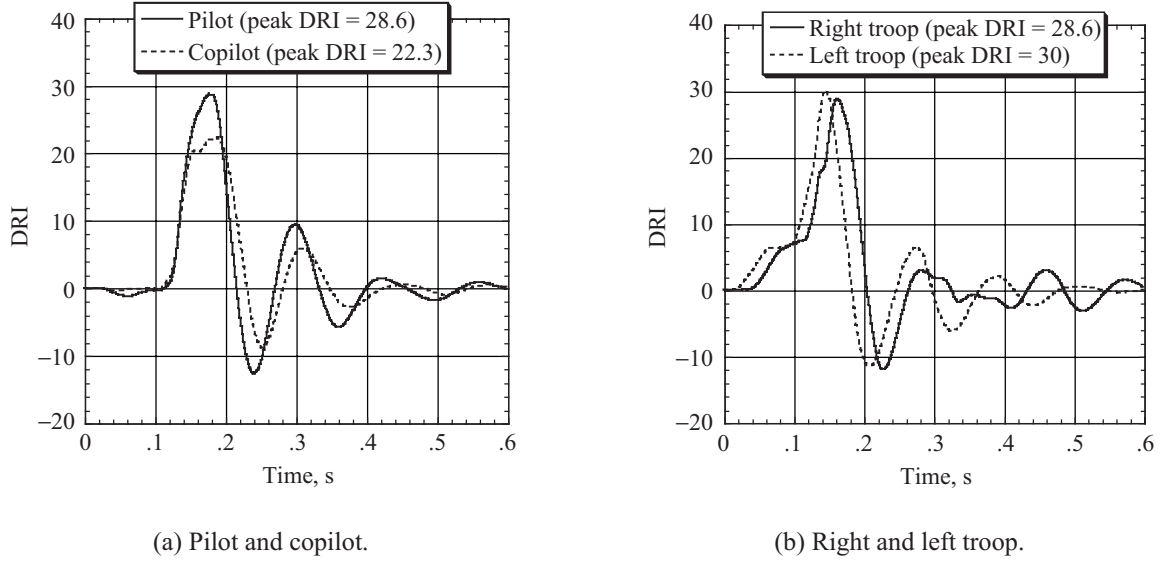


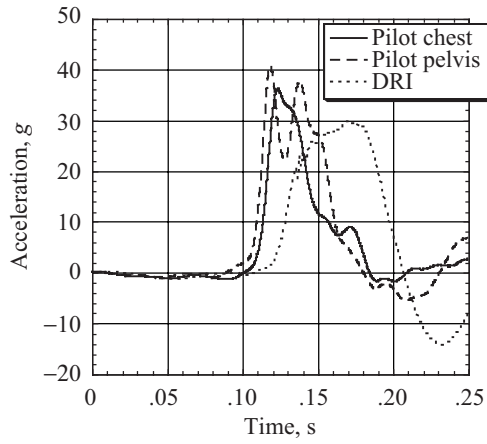
Figure 41. Continuous DRI responses of the four dummies.

Occupant acceleration data are compared with the continuous DRI responses in figure 42. For the pilot, both the chest and pelvis filtered vertical acceleration responses are compared with the DRI (fig. 42(a)). For the copilot and the two troops, only the filtered vertical acceleration response of the chest is compared with the DRI (figs. 42(b), (c), and (d)). In general, the DRI model underpredicts the peak accelerations of the pilot and copilot responses, and it overpredicts the peak accelerations of the troop responses. Also, the time of occurrence of peak acceleration is delayed for the DRI model in comparison with the test data. The continuous DRI data for the troop occupants must be viewed with caution because the cloth seat pan was torn during the test, allowing the buttocks of the troop dummies to displace through the seat frame. Consequently, the vertical acceleration response of the seat frame is not likely to be a good indicator of occupant response or injury potential.

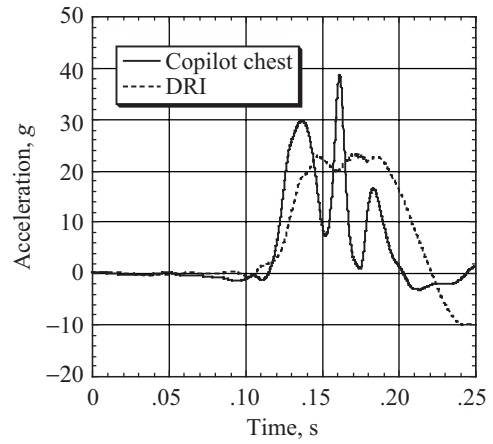
The one-dimensional DRI model has obvious limitations for application to impact scenarios involving multidirectional acceleration components. Consequently, a more comprehensive method, which was developed to account for acceleration components in the three orthogonal axes on the human occupant, was applied (ref. 25). The FORTRAN program DYNRESP (ref. 26), obtained from NASA Johnson Space Center, was used to calculate the dynamic response and injury risk assessment of a seated occupant by analyzing the measured x , y , and z linear accelerations of the seat. These directions are defined in figure 43. The dynamic response of the occupant is modeled by a mass, spring, and damper system attached to the seat. Each orthogonal axis is modeled with a different spring-damper representation. The general risk of injury, β , is determined from the DRI values in the three axes and the defined dynamic response limits in these directions, as indicated in the following equation:

$$\beta = \left[\left(\frac{DRX}{DRX_L} \right)^2 + \left(\frac{DRY}{DRY_L} \right)^2 + \left(\frac{DRZ}{DRZ_L} \right)^2 \right]^{1/2} \quad (2)$$

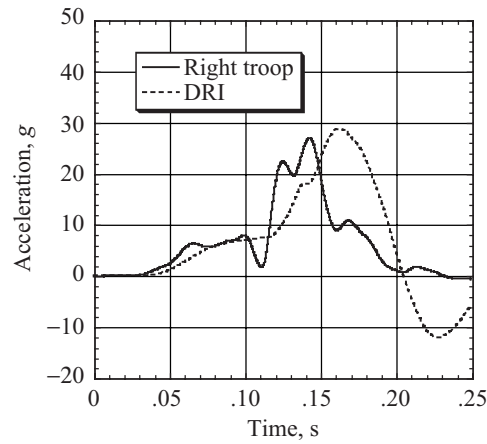
where DRX , DRY , and DRZ are the maximum DRI values for the X -, Y -, and Z -axes; DRX_L , DRY_L , and DRZ_L are the limit values defined for low, moderate, and high risk. The injury-risk criterion β is



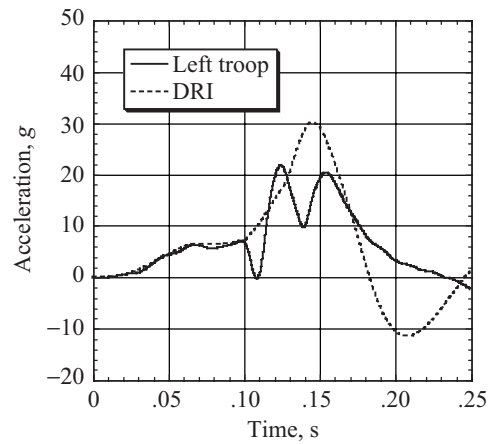
(a) Pilot chest and pelvis data and DRI.



(b) Copilot chest data and DRI.



(c) Right troop chest data and DRI.



(d) Left troop chest data and DRI.

Figure 42. Occupant responses and continuous DRI model.

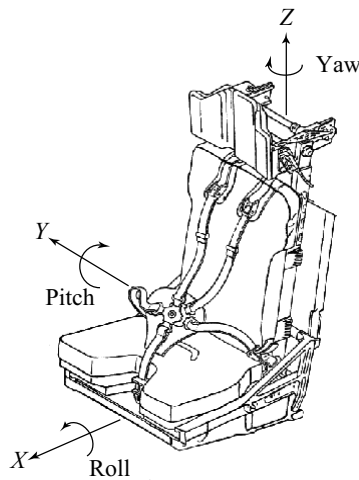


Figure 43. Axis system used to calculate the combined DRI response.

Table 3. Dynamic Response Limit Values for Low, Moderate, and High Risk

Risk level	DRX_L		DRY_L		DRZ_L	
	$DRX > 0$	$DRX < 0$	Conventional restraint	Side panels	$DRZ > 0$	$DRZ < 0$
Low	35	28	14	15	15.2	9
Moderate	40	35	17	20	18	12
High	46	46	22	30	22.8	15

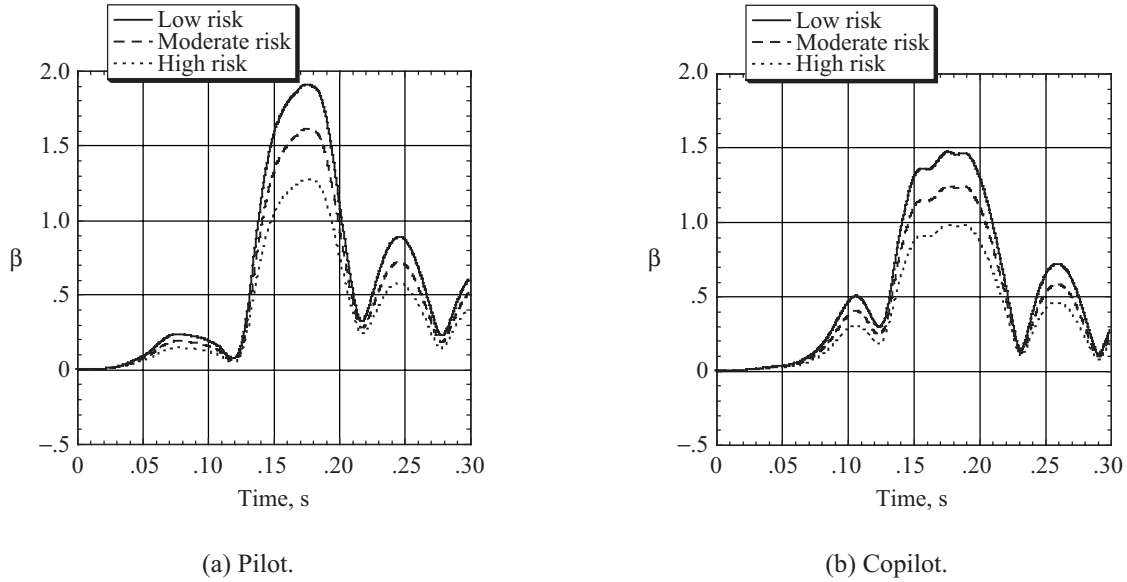


Figure 44. Injury risk assessment for the pilot and copilot dummies.

calculated for each risk level. Values of β greater than 1.0 indicate that the occupant exceeded that level of risk. Different dynamic response limit values, listed in table 3, are used for low, moderate, and high risk (ref. 25).

This model was applied by inputting the forward (x) and vertical (z) components of acceleration obtained from the pilot and copilot seats into the dynamic response model described by equation (2). No side component of acceleration was input because it was not measured in the test. Data from other locations indicate that the side accelerations were minimal and therefore the omission of this component should not significantly affect these computations. The results of this injury risk assessment are shown in figure 44. For the pilot, all three of the risk assessment curves exceeded the threshold value of 1.0, indicating a high risk of injury. For the copilot, the high risk curve is close to 1.0, but does not exceed the threshold. Thus, the results indicate a moderate risk of injury for the copilot.

3.9.2. Spinal Force

A second injury assessment criterion, defined in FAR Part 27.562(c) (ref. 19), is that spinal load should not exceed 1500 lb. Both the pilot and copilot dummies were instrumented with lumbar load cells to measure force along the spine. A plot of lumbar load versus time is shown in figure 45 for the pilot

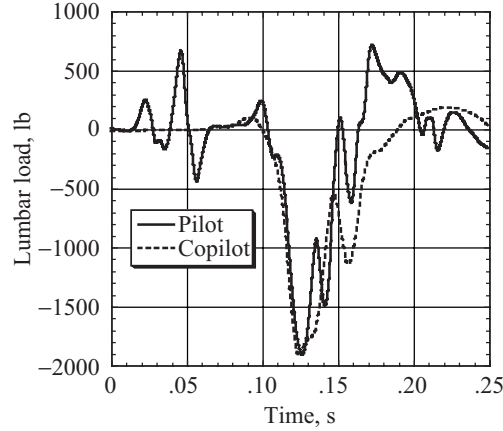


Figure 45. Pilot and copilot vertical lumbar load responses.

and copilot dummies. Initially the load is tensile, perhaps from the forward motion of the dummy as the helicopter slows down horizontally. The maximum compressive loads measured for the pilot and copilot dummies are 1912 and 1921 lb, respectively. These loads occur during fuselage floor impact and about 0.005 s after the peak pelvis vertical acceleration. They exceed the 1500-lb threshold for spinal injury that is the maximum load for civil seat certification (ref. 21).

3.9.3. Head Injury Criterion

The Federal Motor Vehicle Safety Standard (FMVSS) 208 (ref. 27) includes a head impact tolerance specification called the head injury criterion (HIC) (ref. 28). The HIC was originally developed as a modification of the Wayne State University Tolerance Curve (ref. 29) and is calculated as

$$\text{HIC} = \left\{ (t_2 - t_1) \left[\frac{1}{t_2 - t_1} \int_{t_1}^{t_2} a(t) dt \right]^{2.5} \right\} \quad (3)$$

where t_1 is the initial time of integration, t_2 is the final time of integration, and $a(t)$ is the resultant acceleration in g measured at the CG of the head. The FMVSS 208 establishes a maximum value of 1000 for the HIC, which is associated with a 16-percent risk of serious brain injury. It also specifies that the time interval used in the integration ($t_2 - t_1$) should not exceed 0.036 s. Limitations in using the HIC have been documented in the literature (ref. 30), including a study that found that the critical time duration used in the HIC calculation should be equal to or less than 0.015 s (ref. 28). For this evaluation, both time intervals are used in the HIC calculation.

The resultant head acceleration response was calculated for the copilot dummy occupant, as shown in figure 46. For the pilot, only the vertical and side components of acceleration were available because the forward acceleration channel was lost after 0.15 s. Consequently, no HIC calculation was attempted for the pilot. As shown in figure 46, the copilot experiences a peak acceleration of almost 500g at 0.188 s. The duration of this acceleration spike is approximately 0.003 s. The data shown in figure 46 were used to calculate HIC values for time intervals of 0.036 and 0.015 s. The initial time, t_1 , used in the HIC calculations was varied systematically from the beginning of the pulse to determine the maximum value of HIC.

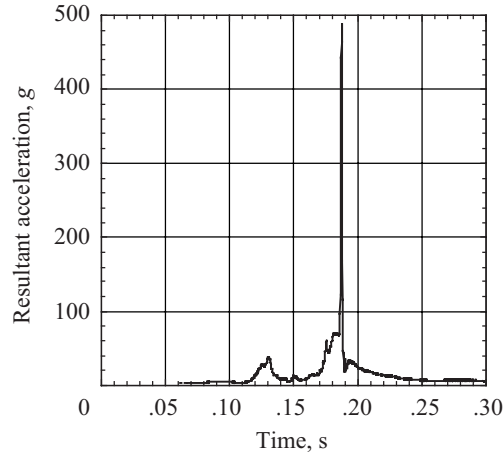


Figure 46. Resultant acceleration response of the copilot head.

Table 4. Summary of Copilot Head Injury Assessment

Head injury data	Copilot
Peak head resultant acceleration, g.....	486.7
Time of occurrence of peak acceleration, s	0.188
Calculated HIC for time duration of 0.036 s	713
Initial time, t_1 , for max HIC with 0.036 s duration, s	0.172
Calculated HIC for time duration of 0.015 s.....	1185
Initial time, t_1 , for max HIC with 0.015 s duration, s	0.175

The results of the HIC analysis, shown in table 4, indicate that the copilot experienced a head impact during the crash test. The copilot HIC values were 713 and 1185 for time intervals of 0.036 and 0.015 s, respectively. These results also confirm the need to evaluate HIC for different time intervals. In this case, the higher value of HIC (greater than 1000) was found using the shorter (0.015 s) time interval.

3.9.4. Whole-Body Acceleration Tolerance

The crew and troop occupant acceleration responses are compared with the whole-body acceleration tolerance curve established by Eiband (ref. 31). The Eiband acceleration tolerance levels were determined from sled impact tests on human volunteers, pigs, and chimpanzees that were conducted for a single input acceleration pulse in the lateral, longitudinal, and vertical directions. Because the ACAP helicopter crash test was performed under combined velocity conditions, the results of this comparison must be viewed with caution. In addition, the Eiband curve was determined for a trapezoidal-shaped input acceleration pulse consisting of three phases: a ramp up phase to a uniform acceleration phase followed by a ramp down phase. The duration and magnitude of the uniform phase of the acceleration pulse is then plotted on the Eiband curve. However, the vertical acceleration responses of the crew and troop occupants are generally sinusoidal in shape. Consequently, the procedure outlined in reference 32 was used, in which a line of constant acceleration is drawn horizontally intersecting the pulse data. Next, the durations of any acceleration data exceeding that value are calculated and summed to determine the total amount of time in which the constant acceleration level was exceeded. This process was initiated for a constant acceleration level of 2.5g and repeated for increasing values of acceleration in intervals of 2.5g

until the maximum value was reached. The resulting acceleration versus duration data are plotted on the Eiband curve for each occupant response, shown as the dashed and dotted lines in figures 47–49.

The pilot chest and pelvis vertical acceleration data are plotted on the Eiband curve in figure 47. Both curves transition from the area of voluntary human exposure into the area of moderate injury. Similar trends are seen for the copilot chest and the right and left troop chest vertical acceleration data that are plotted on the Eiband curve in figures 48 and 49, respectively. These results indicate that, based on the Eiband whole-body acceleration tolerance curve, all of the dummy occupants onboard the Sikorsky ACAP helicopter experienced a moderate risk of injury during the crash test.

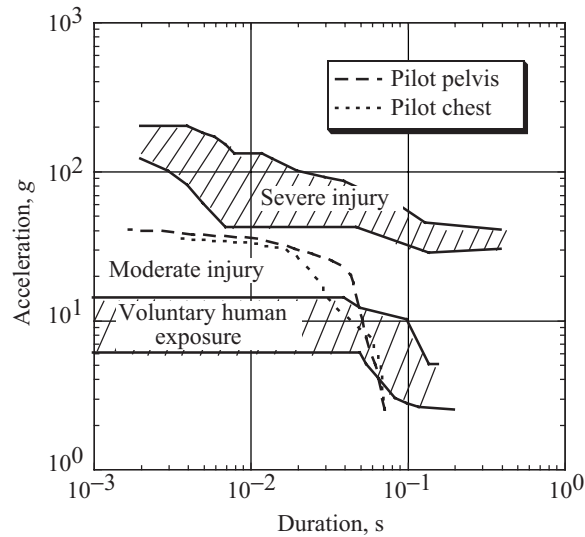


Figure 47. Pilot chest and pelvis vertical acceleration data plotted on the Eiband curve.

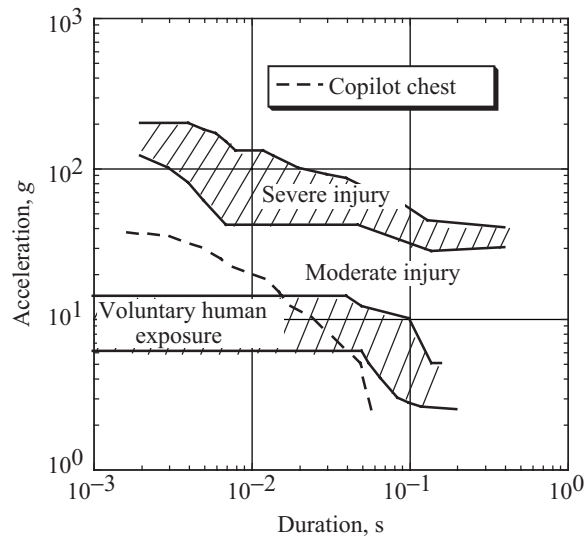


Figure 48. Copilot chest vertical acceleration data plotted on the Eiband curve.

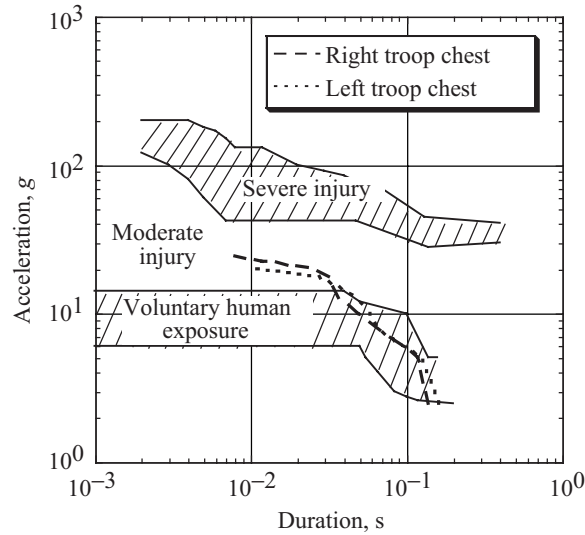


Figure 49. Vertical chest acceleration data of the troop dummies plotted on the Eiband curve.

3.9.5. Injury Assessment Reference Values

Injury Assessment Reference Values (IARV) are provided in reference 33 for restrained Hybrid III dummy occupants. Injury guidelines are specified for the head (HIC requirement with a pulse duration less than or equal to 0.015 s); the head/neck interface including flexion and extension bending moments, axial tension and compression forces, and fore/aft shear force; chest acceleration and deflection; and femur, knee, and tibia loads. The applicable injury guidelines are listed in table 5 along with corresponding measurements from the modified Hybrid III anthropomorphic dummy representing the copilot. The results shown in table 5 are for a midsize (50th percentile) male occupant. The IARV have been proposed to the National Highway Traffic Safety Administration (NHTSA) as guidelines for assessing injury potentials associated with measurements made with Hybrid III-type adult dummies. The IARV refer to a human response level below which a specified injury is considered unlikely to occur for the given size individual. The data for the copilot dummy are less than the IARV limits listed in table 5 with the exception of head/neck tensile force and HIC. These results are indicative of head and neck injury as a result of a head strike.

Table 5. Comparison of Copilot Data With IARV

Parameter	Units	50th male IARV limits	Copilot dummy data
Head/neck interface			
Flexion moment	in-lb	1684	518
Extension moment	in-lb	505	146
Shear (fore/aft)	lb	247	246
Tension	lb	247	617.5
Compression	lb	247	217.5
Chest acceleration (resultant), 0.003 s	g	60	3 peaks > 60g of 0.0015 s duration
Head ($t_2 - t_1 \leq 0.015$ s)	HIC	1000	1185

3.9.6. Summary of Injury Assessment

It is evident from the copilot head and T-1 thoracic acceleration responses, plotted in figures 33 and 34, respectively, and from the head and neck forces listed in table 5 that the copilot dummy experienced a head strike during the crash test. As mentioned previously, a small piece of cloth was found on the right side of the dummy's forehead that appeared to originate from an impact with the dummy's knee. The actual head strike with the dummy's knee could be seen in the high-speed film, which showed that the copilot's head and upper torso experienced a large downward translation and forward rotation during the test. The HIC values determined from the resultant head acceleration of the copilot ranged from 713 to 1185 depending on the time interval used in the calculation. For the midsize Hybrid III dummy, HIC values greater than 1000 are indicative of a 16-percent risk of serious brain injury. The maximum one-dimensional DRI value of 22.3 for the copilot was the lowest of any of the four dummy occupants, yet still indicates a 50-percent risk of spinal injury. The spinal force measured for the copilot was 1921 lb, which exceeded the 1500-lb injury threshold. In addition, the copilot chest acceleration data fall into the region for moderate injury on the Eiband whole-body acceleration tolerance curve.

Without the forward component of head acceleration, it was not possible to perform a HIC assessment for the pilot occupant. However, the other injury criteria indicate that the pilot experienced moderate to severe injury. The maximum DRI for the pilot was 28.6, indicating a greater than 50-percent risk of spinal injury. The risk assessment for the pilot using the combined dynamic response model shown in equation (2) indicated that each of the low, moderate, and high risk curves exceeded the threshold value. The maximum lumbar load measured for the pilot was 1912 lb, exceeding the 1500-lb limit for spinal injury. Finally, the pilot chest and pelvic vertical acceleration data fall into the region for moderate injury on the Eiband whole-body acceleration tolerance curve.

Because the troop dummies were less heavily instrumented than the crew dummies, fewer occupant response data are available for performing an injury risk assessment. However, the DRI values for these occupants ranged from 28.6 to 30, indicating a greater than 50-percent risk for spinal injury. However, these values must be viewed with caution because the canvas seat pans in the troop seats failed during the test allowing the buttocks of the dummies to displace through the seat frames. The vertical chest acceleration data of the left and right troop dummies fall into the area of moderate risk on the Eiband whole-body acceleration tolerance curve.

The assessment of occupant injury indicates that the ACAP helicopter crash test resulted in a moderate to high level of risk for injury overall. Although some injuries would likely have occurred in this crash, the probability of fatalities is considered small. Additional information on the occupant responses and risk assessment can be found in references 34 and 35.

4. Model Development

The commercial code MSC.Dytran (ref. 4) was used for the crash simulation of the ACAP helicopter. MSC.Dytran is a three-dimensional finite element code that was developed to accurately simulate the nonlinear, transient dynamic response of airframe structures. Features of the code include:

1. An element library with 2-noded rod and beam elements; 3- and 4-noded shell elements; 4-, 6-, and 8-noded solid elements; spring and damper elements; and concentrated masses.

2. A number of material models and state equations representing a wide range of material behavior including a crushable foam constitutive model, laminated composite material properties for beam and shell elements, and a general user-defined material model.
3. An explicit time integration technique that is conditionally stable over a restricted range of integration time step sizes.
4. Contact algorithms that allow gaps and sliding of material interfaces with friction.

In addition, the code can be used to simulate highly complex fluid-structure interaction problems through the coupling of a Lagrangian processor for structural modeling with an Eulerian processor for modeling the fluid. The MSC.Dytran input deck format was developed to be compatible with the structural analysis code, MSC.Nastran (ref. 36).

4.1. Description of the MSC.Nastran Modal-Vibration Model

An MSC.Nastran model of the ACAP helicopter that was originally developed for correlation with modal-vibration data was obtained from Sikorsky Aircraft Corporation (ref. 37). This model, shown in figure 50, had approximately 5000 nodes, 9500 elements, 220 material models including many different composite materials, and over 700 different property cards. The elements included 5453 shell elements, 1956 beam elements, 1770 rod elements, and 372 concentrated masses. Because this model was originally used for modal analysis, extensive modifications were required to convert it into a model suitable for crash analysis.

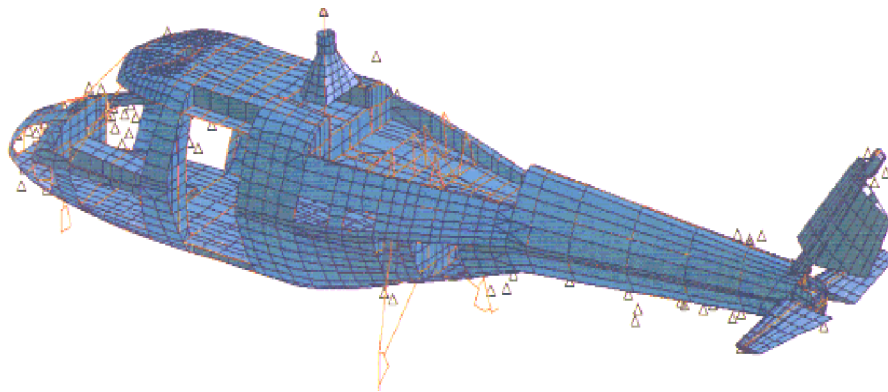


Figure 50. MSC.Nastran modal-vibration model of the ACAP helicopter.

4.2. Conversion of the Modal-Vibration Model to a Crash Model

The initial work in converting the modal-vibration model to an input deck suitable for crash simulation concentrated on combining elements, deleting unnecessary elements, and redscretizing the model. The original linear elastic material property cards had to be modified to include yield stress, strain hardening, density, and maximum strain to failure, as appropriate. The finite element mesh of the tail cone was greatly simplified, and the elements representing the stabilizer and rudder were removed. A transition mesh was developed to connect the coarse mesh of the tail cone to the finer mesh of the fuselage cabin. Many of the original triangular elements were combined and converted to quadrilateral elements. Triangular elements are not recommended for models that undergo large displacements, as they are typically too stiff.

In the original MSC.Nastran model, the inertial properties of the structural model were input by using concentrated masses, i.e., no material densities were assigned to the elements. In converting the model for crash simulation, most of these concentrated masses were removed and material densities were assigned to the elements. Other concentrated masses were modified or added to represent actual lumped masses on the helicopter, including the rotorcraft transmission, engines, anthropomorphic dummies, seats, fuel, instrumentation boxes, batteries, and cameras.

The elements in the original modal-vibration model representing the main and nose landing gears were removed. An external user-written subroutine was developed to calculate the main landing gear forces as a function of velocity and stroking distance including both the oleo-pneumatic and the crushable honeycomb stages. The original crashworthy nose gear of the ACAP helicopter had been removed and replaced with a noncrashworthy standard nose gear. Modifications were required to make the existing nose gear more crashworthy. The hydraulic fluid was drained, and a thin-walled aluminum tube with a honeycomb core was inserted inside the gear to provide some energy absorption. The modified nose gear was modeled as a spring having a constant spring force of 8000 lb to represent the crush strength of the honeycomb-filled aluminum tube. A more detailed description of the landing gear model is provided in section 5.1, "Landing Gear Model."

Because the original modal-vibration model was too detailed in some regions and too coarse in other regions, some rediscritization of the mesh was performed. One of the main energy-absorbing devices for the structure was the crushable lower portion of the keel beams and subfloor bulkheads. There were two inner keel beams and two outer keel beams beneath the floor. The keel beams and transverse bulkheads beneath the floor were constructed of two horizontal C-channels, one above the other, with a beaded (or waffle) web geometry. The upper channel was constructed of graphite and the lower 4-in-high beaded web was constructed of Kevlar™. The outer keel beams were very thick and did not crush in the test. The lower portions of the inner keel and bulkhead beams were fabricated of a thinner beaded Kevlar™ construction designed to crush and absorb energy. In the original modal-vibration model, the crushable Kevlar™ web was modeled using 4-in-high shell elements with longitudinal beam elements to represent the flanges of the C-sections. The Kevlar™ shell elements representing the keel beam and the bulkheads were rediscritized by dividing each original shell element vertically into four shell elements. This representation, shown in figure 51, allowed crushing to occur.

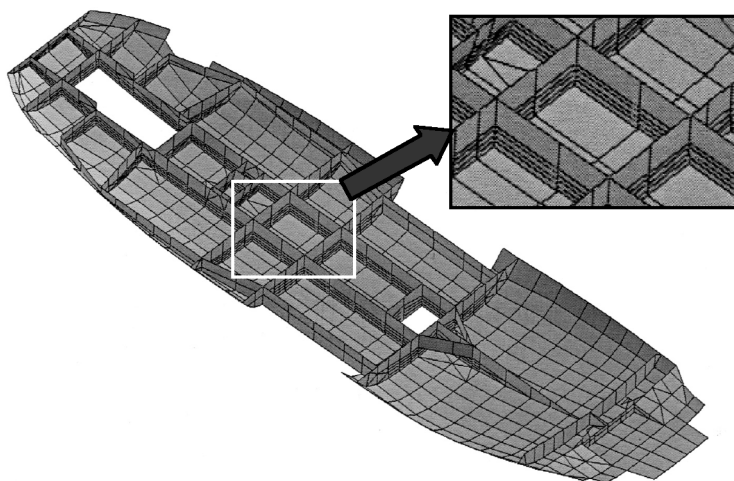
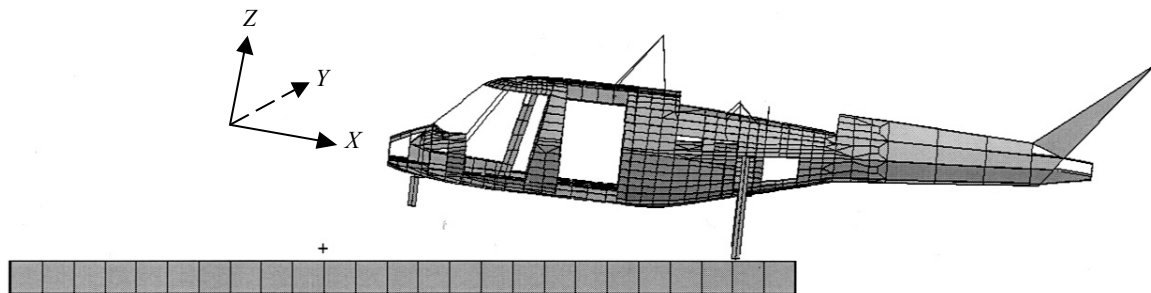


Figure 51. Finite element model of the ACAP helicopter subfloor.

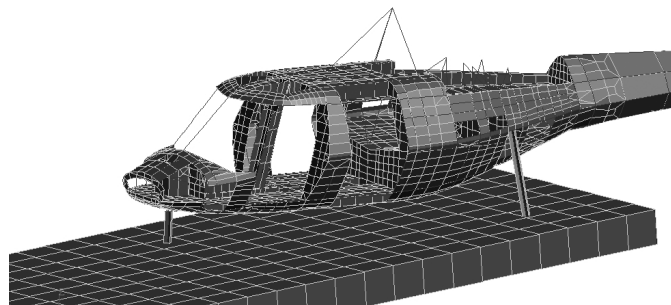
Following the extensive modifications, the ACAP helicopter crash model executed with a time step of approximately $1.9 \mu\text{s}$. The model was run many times to track down the elements controlling the time step. These elements were then combined with other elements to increase the time step to an appropriate duration to allow a reasonable run time for the model. The MSC.Patran commercial software package was used with the MSC.Dytran “preference” to build and modify the finite element crash model and to post-process the results (ref. 38).

4.3. Description of the Crash Model

The final crash model of the ACAP helicopter is shown in figure 52. The model consists of 4128 grid points and 7346 elements, including 3118 beam and rod elements, 3283 quadrilateral shell elements, 695 triangular shell elements, and 250 solid elements that represent the impact surface. The number of different material property cards was reduced from 219 in the MSC.Nastran modal-vibration model to 34 in the MSC.Dytran crash model. The primary material properties are listed in table 6. In addition, the number of different property cards for shell elements was significantly reduced by combining many of the *PCOMP* cards. The *PCOMP* cards are used in MSC.Dytran to specify the material properties and orientations of each ply in a laminated composite shell element. (Please note that words that appear italicized and in all caps refer to specific cards used in the MSC.Dytran input deck.) Also, the total number of concentrated masses in the model was reduced from 372 in the modal-vibration model to 98 in the crash model. The 98 concentrated masses represent actual lumped masses used in the experiment, as indicated in table 7. In the final crash model, the structural elements weighed 2838 lb and the concentrated masses weighed 5160 lb, for a total weight of 7998 lb.



(a) Side view.



(b) Three-quarter view.

Figure 52. Final crash model of the ACAP helicopter.

Table 6. Primary Material Properties in the MSC.Dytran Model of the ACAP Helicopter

Material	Formulation	Density, lb-s ² /in ⁴	Young's modulus, psi	Shear modulus, psi	Poisson's ratio	Yield stress, psi	Hardening modulus, psi
Steel	<i>DMATEP</i>	0.000756	29e6	NA	0.3	100 000	10 000
Aluminum	<i>DYMAT24</i>	0.000267	10.5e6	NA	0.33	35 000	NA
Titanium	<i>MAT1</i>	0.00041	16e6	6.2e6	NA	NA	NA
Graphite-epoxy tape	<i>MAT8</i>	0.000148	$E_1 = 18\text{e}6$ $E_2 = 1.1\text{e}6$	$G_{12} = 0.62\text{e}6$	$\nu_{12} = 0.3$		
Graphite-epoxy fabric	<i>MAT8</i>	0.000148	$E_1 = 9.45\text{e}6$ $E_2 = 9.45\text{e}6$	$G_{12} = 0.53\text{e}6$	$\nu_{12} = 0.05$		
Kevlar™ fabric	<i>MAT8</i>	0.000129	$E_1 = 3.4\text{e}6$ $E_2 = 3.4\text{e}6$	$G_{12} = 0.21\text{e}6$	$\nu_{12} = 0.19$		
Aluminum core 5052	<i>MAT8</i>	0.00022	$E_1 = 100$ $E_2 = 100$	$G_{12} = 100$ $G_{13} = 32\,000$ $G_{23} = 16\,200$	$\nu_{12} = 0.3$		
Nomex™ core	<i>MAT8</i>	0.0001	$E_1 = 100$ $E_2 = 100$	$G_{12} = 100$ $G_{13} = 4\,000$ $G_{23} = 2\,600$	$\nu_{12} = 0.3$		
Glass core	<i>MAT8</i>	0.00017	$E_1 = 100$ $E_2 = 100$	$G_{12} = 100$ $G_{13} = 43\,000$ $G_{23} = 20\,000$	$\nu_{12} = 0.3$		
E-glass tape	<i>MAT8</i>	0.00017	$E_1 = 5.4\text{e}6$ $E_2 = 2.05\text{e}6$	$G_{12} = 0.38\text{e}6$	$\nu_{12} = 0.23$		
Graphite winding	<i>MAT8</i>	0.00015	$E_1 = 18.9\text{e}6$ $E_2 = 1.3\text{e}6$	$G_{12} = 0.63\text{e}6$	$\nu_{12} = 0.31$		

Table 7. Summary of Major Concentrated Masses in the Finite Element Model

Description	Weight, lb
Pilot dummy and seat	279.3
Copilot dummy and seat	315.5
Right and left fuel tank (805 lb each)	1610.0
Nose gear	52.0
Lifting hard point in the nose	98.0
Right and left main gear (122 lb each)	244.0
Right and left engine (315 lb each)	630.0
Main gearbox	832.0
Tail mass	69.0
Main rotor hub mass	352.6
Right and left troops and seats (180 lb each)	360.0
Miscellaneous	317.6
Total	5160.0

A flat plate consisting of 250 solid elements with fixed bottom nodes was added to the model to represent the impact surface. A master-surface to slave-node contact was defined between the flat impact surface and the nodes in the structural model. The initial conditions including the pitch and roll angle and the translational and rotational velocities were determined from measurements made from the high-speed video and from motion picture analysis of the high-speed film. A right-handed coordinate system was used in the helicopter model with the X -axis positive from nose to tail, Z -axis positive up, and Y -axis positive to the right, as illustrated in figure 52. The nominal impact conditions are 38.5-ft/s vertical velocity, 32-ft/s longitudinal velocity, 9.6°/s pitch angular velocity (rotating nose up and tail down due to swing), 6.25° nose-up pitch, and 3.5° left-down roll. For this simulation, it was more expedient to adjust the position of the impact surface rather than the structural model to account for the roll and pitch attitude. The position of the CG of the helicopter model was determined to be $x = 203.7$ in., $y = 0$ in., and $z = 87$ in. Note that these dimensions are given in reference to the manufacturer's FS, BL, and WL coordinate system that is shown in figure 4.

5. Simulation Strategy

To perform the simulation, a two-stage modeling approach was employed in which a rigid structural model of the helicopter was executed during deformation of the landing gear. At 0.045 s before fuselage contact, the x -, y -, and z -locations of all grid points and the corresponding nodal velocities in the rigid model were output to a file. These initial conditions were then input as the starting point of the flexible model simulation. This rigid-to-flexible approach was used to significantly decrease the central processing unit (CPU) time required to complete the simulation, and because the rigid model made the introduction of the pitch angular velocity easier. The landing gear model, rigid structural model, and flexible structural model are discussed in the following subsections.

5.1. Landing Gear Model

For impacts on hard surfaces, an accurate simulation of the energy-absorbing response of the landing gear is imperative to predict the impact response of the fuselage. The landing gear stroking not only reduces the fuselage impact speed, but can also change the impact attitude. The stroking of the landing gear, which typically lasts 0.1 s, generally produces lower acceleration levels than the fuselage impact, resulting in primarily elastic deformations to the fuselage. These considerations enabled use of a rigid fuselage model during most of the time that the landing gear was stroking. The time step for a rigid model is typically an order of magnitude larger than that for the flexible model; therefore, the required clock time to perform a simulation is reduced by an order of magnitude. For the model presented here, the CPU time was reduced by a factor of eight. Additional details regarding the landing gear modeling can be found in reference 39.

A schematic of the ACAP main landing gear as viewed aft of the aircraft is shown in figure 53. The main gears were designed with a two-stage, energy absorption approach. For landings within the normal operational range, an oleo-pneumatic energy absorber was incorporated. For severe or crash landings, additional energy is absorbed through stable crushing of an aluminum honeycomb column within the gear. The transfer from the oleo-pneumatic to the honeycomb stage is accomplished by shear pin failures based on a predetermined force. The orientation of the gear with respect to the fuselage remains nearly constant while the oleo-pneumatic stage is stroking. The initial angle with respect to the vertical, as shown in figure 53, is 11.8°. As the honeycomb crushes, the gear rotates outward an additional 20°. The drag beam controls the gear rotation.

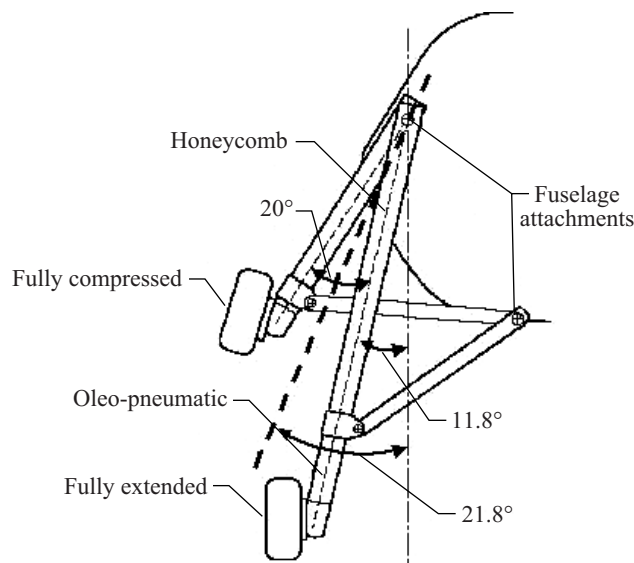


Figure 53. Schematic of ACAP landing gear, looking aft.

To simplify the finite element model of the main landing gear mechanism as much as possible, the angle of the landing gear was fixed with respect to the aircraft vertical axis. Therefore, the translational and rotational motions of the gear have been replaced with purely translational motion. The angle was determined by bisecting the angle through which the gear strokes, or $11.8^\circ + 0.5 \times 20^\circ = 21.8^\circ$, as shown in figure 53.

Initially, the landing gear model was to be developed by using a number of rigid joints, such as sliding, rotational, ball, and universal joints that are currently available as standard capabilities in commercial codes. However, these joints can become unstable when large forces, such as those experienced by the landing gear during a severe impact, are applied. For this reason, these built-in joints were replaced in the model with a component containing a single spring element with a user-defined force response to represent both the oleo-pneumatic and crushable honeycomb stages, and several beam elements that were used to define the correct gear geometry and to distribute the constraint forces, as illustrated in figure 54(a). In general, the spring force equation can be dependent on the relative displacement and the relative velocity of the connected nodes. This flexibility allows a user-defined spring to simulate the response of the velocity-dependent oleo-pneumatic stage and the crushable honeycomb stage, which depends only on displacement. A FORTRAN subroutine was written to simulate the force applied to the fuselage by the main landing gears as they stroke. The equations defining the oleo-pneumatic portion are found in appendix A of the *KRASH 85 User's Guide* (ref. 2). The equations account for the air spring friction, hydraulic damping, and coulomb friction. The values for the various parameters defining the ACAP main landing gear were taken from information supplied by the airframe manufacturer.

The transition from oleo-pneumatic to honeycomb crushing results from the shear pin failures in the test article. Because the oleo-pneumatic friction forces are dependent on the velocity, an extremely large, short-duration force is applied at the initiation of contact. For this reason, the simulation was not able to use the computed force to determine the transition. As an alternative, the displacement (stroke) of the oleo-pneumatic portion was used to trigger the transition. The crushing of the honeycomb stage is represented by a constant force of 28000 lb. After fuselage contact, the force due to the landing gear is reduced to zero as an approximation of the transfer of the load from the gear to the fuselage belly.

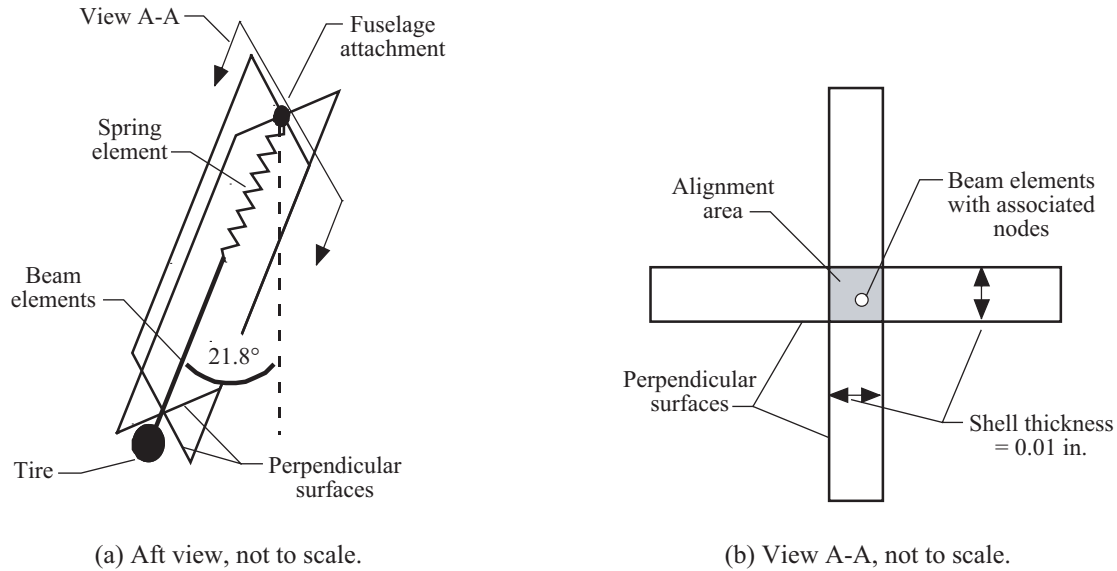


Figure 54. Schematic of the landing gear finite element model.

Alignment of the landing gear model relative to the aircraft can be a challenging modeling problem. For this simulation, nodal alignment was accomplished by creating four contact surfaces on the outer surface of two perpendicular plates. Each perpendicular plate was modeled with a rigid quadrilateral shell element. The nodes of the spring and beam elements forming the landing gear model were then constrained to remain within the intersecting region of the perpendicular shells, as illustrated in figure 54(b). The thickness of the alignment shells was set to provide sufficient stability without creating extremely large contact forces. For the results presented in this paper, the shell thickness was 0.010 in.

As described previously, the original crashworthy nose gear had been replaced with a noncrashworthy standard nose gear, and modifications were required to make the replacement nose gear more crashworthy. The retrofitted nose gear was modeled as a spring having a constant spring force of 8000 lb to represent the crush strength of the honeycomb-filled aluminum tube that was inserted inside the gear.

5.2. Rigid Structural Model

A rigid structural model was created by changing all material properties for all elements to *MATRIG*, except for those elements forming the landing gear. *MATRIG* is a specific material property card in MSC.Dytran that allows elements to be defined as rigid bodies for which mass and moments of inertia are determined by the element geometry and material density. Once *MATRIG* is defined for an element, it cannot deform and the code simply tracks the kinematic motion of the element as the simulation progresses. As described in the previous section, landing gear forces were computed by using an external subroutine. This procedure allowed quick runs (of approximately 1-hr duration) to refine the correlation of the sequence of events and to ensure that the landing gear subroutine accurately predicted the gear forces. For this model, it was important to ensure that the location of the CG and moments of inertia matched the experimental values closely. The rigid model was executed for a duration of 0.045 s after left gear tire contact. The archive files generated by the rigid model were postprocessed in MSC.Patran with user-written commands to create files containing nodal velocities and nodal positions at 0.045 s. The nodal position file, which had the new *GRID* locations for each node, was input into the flexible model using the *INCLUDE* statement. The velocity file was read into the flexible model by an external user-written FORTRAN subroutine.

The choice of 0.045 s as the transition time between the rigid and flexible simulations requires some explanation. Ideally, the rigid simulation would be executed to a point in time just prior to fuselage contact with the ground, which occurred at 0.098 s. Then the transition to a flexible model would be performed to capture the fuselage deformations after that time. This approach would have been used had the fuselage exhibited only rigid body motion from the time of left tire contact to fuselage contact. However, as indicated in table 1, the tail cone began to buckle at 0.064 s. Thus, it was necessary to adjust the transition time to better capture the tail cone response. Also, the shear pin in the right main landing gear failed at 0.045 s, at which point the landing gear response was modeled with a constant spring force representing the crushing of the honeycomb stage. Finally, the time of 0.045 s is approximately half of the time between left gear tire contact and fuselage contact.

5.3. Flexible Structural Model

The flexible structural model was the same as the rigid model except for the following modifications. The material cards were nonrigid, the initial *GRID* coordinates were the same as the nodal positions of the rigid model at 0.045 s, and the initial velocities were the nodal velocities output from the rigid model at 0.045 s. Also, during this latter stage of the analysis, each landing gear force was modeled by using the appropriate constant honeycomb crushing force, 8000 lb for the nose gear and 28000 lb for the right and left main gears. The transition occurred without incident except for a slight discontinuity that occurred when the flexible model was initiated due to the sudden onset of the landing gear honeycomb force. Several techniques to minimize this discontinuity (the acceleration spike at the transition point from rigid to flexible models) were investigated, such as ramping the honeycomb force over multiple time steps. However, none of these approaches was completely effective.

The flexible model included the effects of gravity; however, friction of the impact surface was not included. Friction is difficult to measure experimentally, and would only be significant after fuselage contact. Because friction was not modeled, no results are shown for the longitudinal (forward) or lateral (side) directions. To run the flexible model for 0.1 s real time (from 0.045 to 0.145 s) required approximately 12 CPU hours on a Sun Ultra Enterprise 450 workstation computer. The flexible model is more computationally intense than the rigid model, which required approximately 30 minutes to run a 0.045-s simulation. Additional information regarding the development of the crash model and the modeling approach may be found in references 39–42.

6. Test and Analysis Correlation

6.1. Sequence of Events

An important correlation between the crash simulation and the experimental data is a comparison of the predicted and measured sequence of events. The comparison, shown in table 8, indicates that the simulation correctly predicted the timing of right gear contact, nose gear contact, tail cone failure, and the peak accelerations of four different locations on the helicopter. In most cases, the simulation predicted the event timing within ± 0.007 s. Events occurring earlier than 0.045 s were predicted by using the rigid model, and events occurring after 0.045 s were predicted using the flexible model. Comparisons of the predicted helicopter motion with pictures of the actual crash scenario are shown in figure 55 for time steps of 0.0, 0.05, 0.1, and 0.15 s. The predicted motion of the helicopter agrees well with the observed crash scenario.

Table 8. Predicted and Experimental Time Sequence of Events

Event	Measured test result, s	Simulation, s
Left main gear tire contact	0.0	0.0
Right main gear tire contact	0.012	0.016
Shear failure of the right gear pins	0.045	0.045
Nose gear tire contact	0.069	0.068
Apparent separation of tail cone	0.074	0.075
Time of peak acceleration:		
Left troop seat floor	0.105	0.110
Right troop seat floor	0.107	0.114
Copilot floor	0.110	0.115
Right engine	0.116	0.117

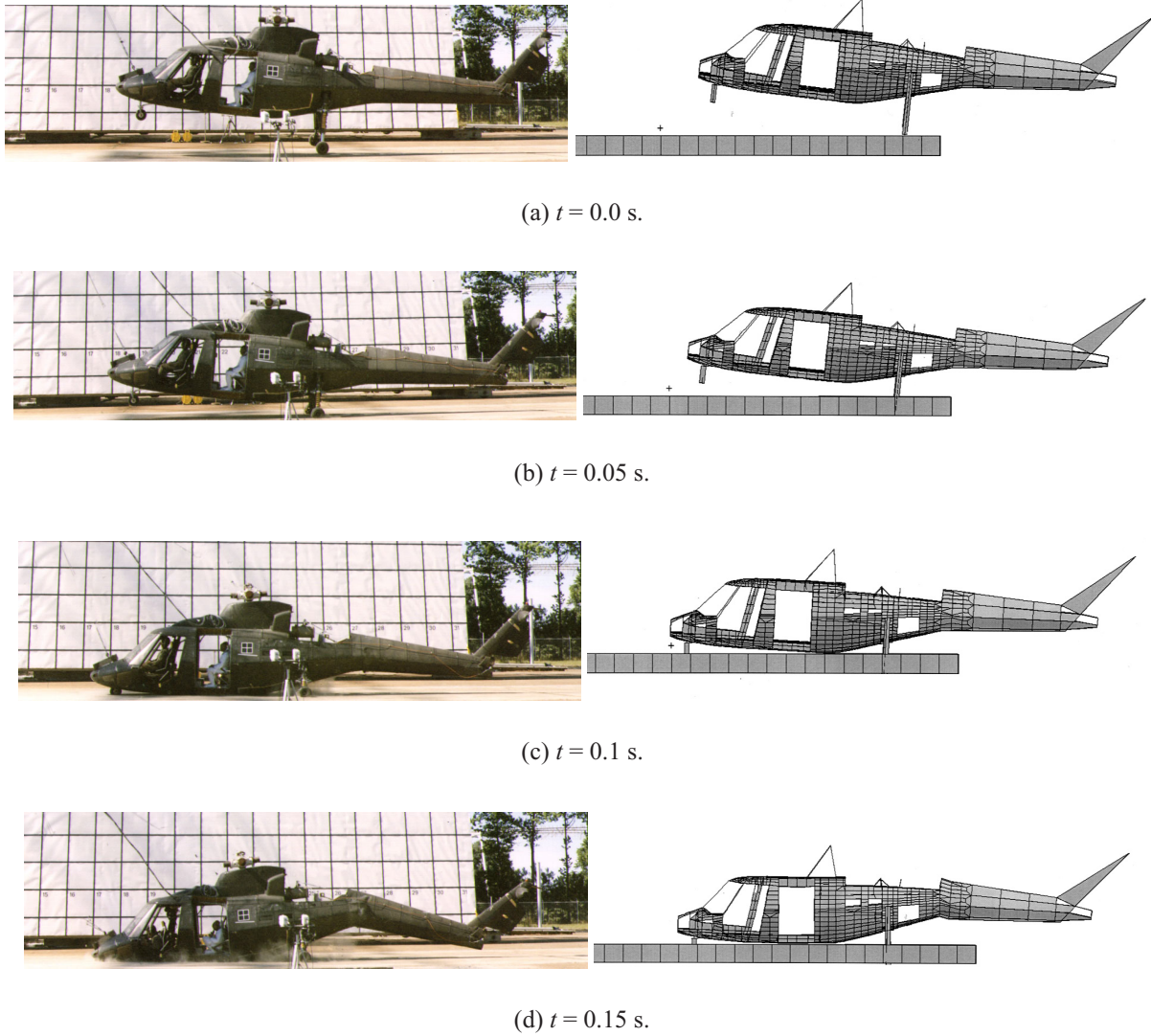
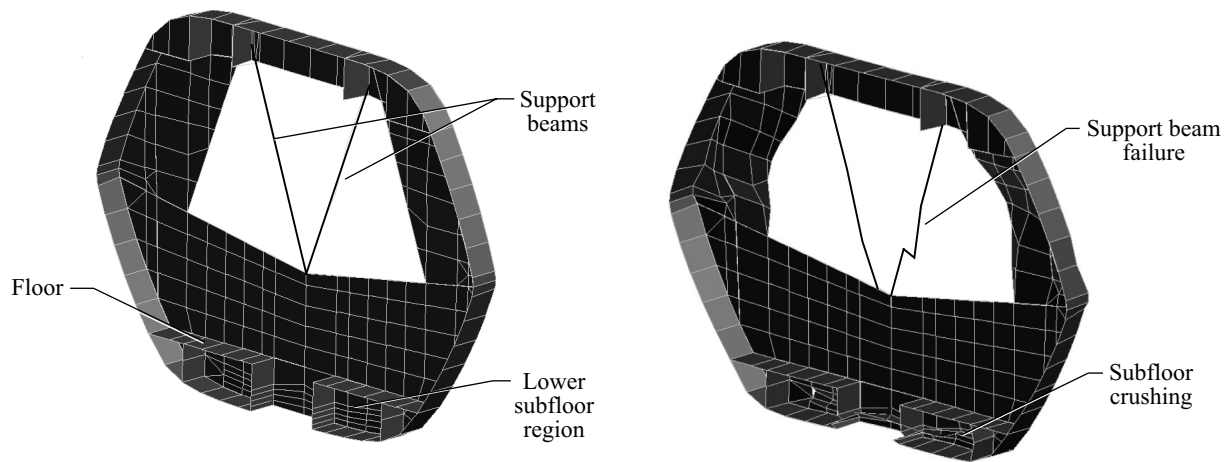


Figure 55. Predicted and experimental crash sequence and deformation.

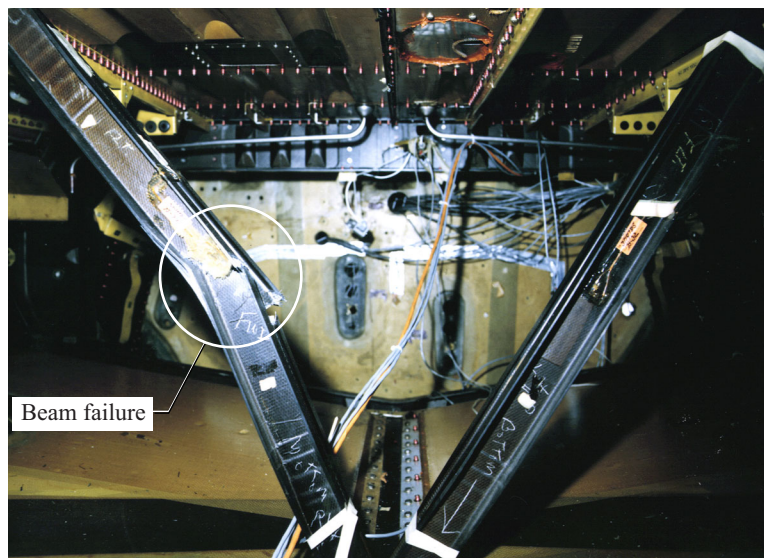
6.2. Structural Deformation

Several discrete structural failures occurred during the crash test, including failures of the ceiling beams in the fuselage cabin, the support beams for the overhead engines and transmission, and the separation of the tail from the fuselage. For example, the undeformed model of the bulkhead at FS 188 is shown in figure 56(a). This bulkhead is located behind the rear of the cabin and beneath the overhead rotor transmission. The model of the bulkhead consists of a ring of shell elements representing the outer skin, with one row of horizontal shell elements representing the floor. The two support beams that form the “V” in the center of the bulkhead were modeled with beam elements and are illustrated with dark lines. The failure of one of the support beams, as predicted by the model at time 0.125 s, is shown in figure 56(b). The buckling of the lower portion of the subfloor is also apparent in the figure. An example of a support beam failure from a posttest photograph is shown in figure 56(c).



(a) Model of the bulkhead and the subfloor located at FS 188 prior to impact.

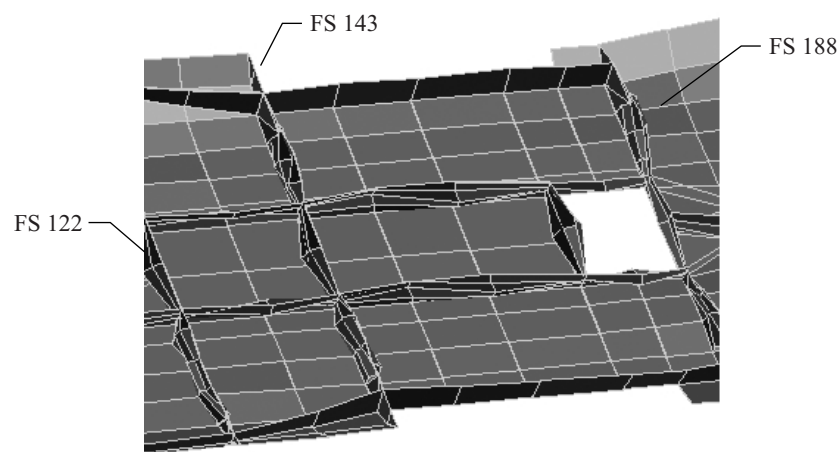
(b) Model showing subfloor crushing and overhead mass support beam failure at 0.125 s.



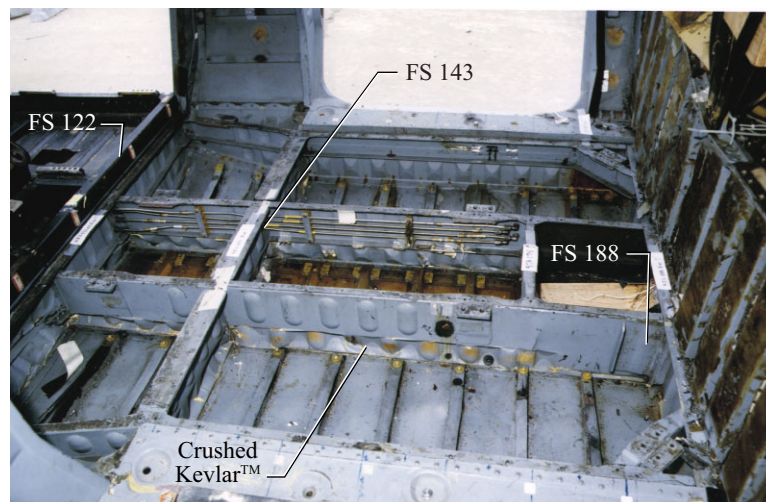
(c) Overhead mass support structure showing posttest damage.

Figure 56. Model deformation and posttest photograph of the bulkhead at FS 188.

One emphasis of this modeling effort was an accurate prediction of the subfloor crushing response. Unfortunately, the displacement transducers that were intended to measure the dynamic subfloor deformation malfunctioned and did not provide data. Consequently, only the posttest floor displacement measurements were available for comparison with predictions. Because no dynamic crush was measured, only a qualitative comparison can be given. The predicted crush of the lower Kevlar™ portion of the subfloor is shown in figure 57(a). For clarity, the upper noncrushing graphite portion of the subfloor is not shown. The initiation of crushing occurred at FS 188 at time 0.105 s, which is shortly after contact of the bottom of the helicopter with the impact surface. At time 0.125 s, all of the inner keel beams exhibit buckling and crushing, as indicated in figure 57(a). An examination of the posttest ACAP fuselage showed that the Kevlar™ subfloor had permanent crush of about 0.25 in. at FS 188. The crush increased forward to a maximum of 1.5 in. at FS 143. The permanent crush at FS 122 ranged from 0.5 to 1.0 in. A photograph of the subfloor from FS 188 through FS 143, shown in figure 57(b), highlights the actual posttest deformation.



(a) Model of the lower portion of the subfloor region at 0.125 s.

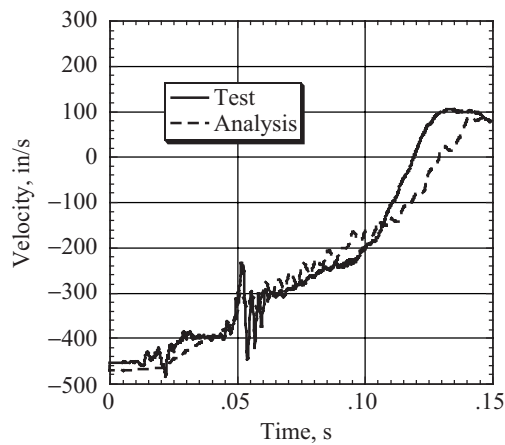


(b) Photograph of the helicopter subfloor between FS 122 and 188.

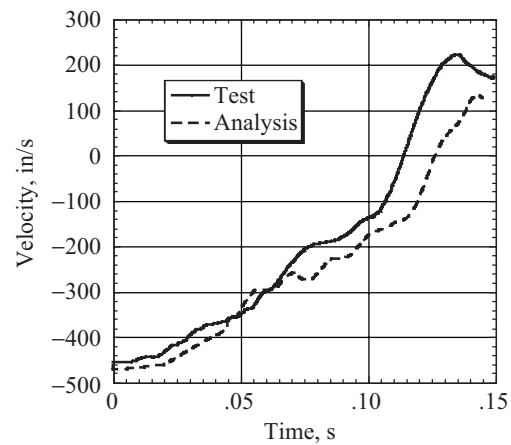
Figure 57. Model and a posttest photograph of deformed subfloor beams.

6.3. Comparison of Velocity Responses

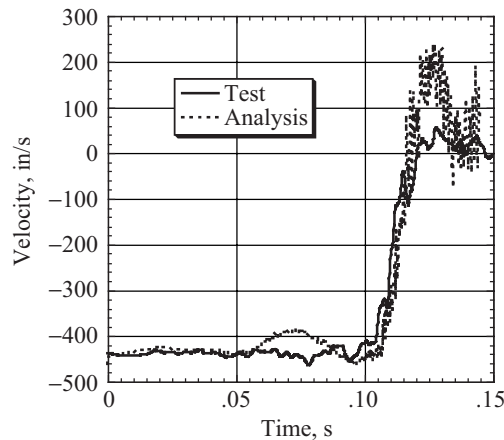
Predicted and measured vertical velocity responses for the top of the right gear, the right engine, and the copilot seat floor are shown in figure 58. The responses were predicted by the rigid structural model from 0.0 to 0.045 s and by the flexible model at 0.045 s to the end of the simulation. The experimental responses were obtained from integration of the accelerometer data. The oscillatory behavior observed in the experimental velocity response of the right main gear at 0.045 s is attributed to failure of the shear pin, which indicates the transition between the oleo-pneumatic stage and the crushable honeycomb stage, as shown in figure 58(a). The absence of oscillations at other locations indicates that this dynamic response remained local to the landing gear attachment. A similar oscillatory response is seen in the predicted velocity response of the right main gear. These vibrations are due to the impulse of the landing gear loads being applied at full load at the start-up of the flexible simulation at 0.045 s. The transition from the rigid to the flexible model is not trivial and can cause considerable problems if not properly administered.



(a) Right main gear.



(b) Right engine.



(c) Copilot seat floor.

Figure 58. Predicted and experimental velocity responses at three locations.

Table 9. Predicted and Experimental Velocities at 0.045 and 0.095 s for Nine Locations

Location	Velocity (in/s) at $t = 0.045$ s			Velocity (in/s) at $t = 0.095$ s		
	Test	Analysis	Percent difference	Test	Analysis	Percent difference
Pilot seat floor	-447.1	-456.4	-2.0	-483	-470.2	2.7
Copilot seat floor	-444.4	-436.3	1.8	-452.6	-458.5	-1.3
Right main gear (top)	-403.5	-382.5	5.2	-232.5	-181.3	22
Right engine	-362.6	-361.4	0.3	-158.2	-209.4	-32.4*
Left engine	-353.8	-361.3	-2.1	-155	-201.4	-29.9*
Right troop floor	-415.8	-411.9	0.9	-312.3	-319.3	-2.2
Left troop floor	-405.3	-403.2	0.5	-299.7	-311.4	-3.9
Rotor head	-393.6	-393.1	0.1	-271.1	-262.3	3.2
Floor at FS 182	-412.3	-399.6	3.1	-311.4	-277.8	10.8

*Electrical anomalies in the right and left engine acceleration responses caused errors in the integrated velocity responses.

Discrete velocity values at 0.045 and 0.095 s for the predicted and experimental velocity responses at nine different locations on the airframe are provided in table 9. These times were chosen for their significance in the simulation and in the sequence of events. The time of 0.045 s was chosen because it is the transition time between the rigid and flexible simulations, and 0.095 s was chosen because it is just prior to fuselage contact with the ground. The percentage differences listed in table 9 were obtained by subtracting the experimental value from the analytical value, then normalizing the difference by the experimental value. Thus, a positive percent difference represents an underprediction of the data, and a negative value represents an overprediction.

The velocity data from the rigid simulation at 0.045 s agree extremely well with the experimental values, within ± 5 percent. However, by the time of fuselage contact, some significant deviations have occurred, most notably for the right and left engine locations. Normally, one would consider that these errors are a result of inaccuracies in the model; however, in this case, the differences are due to electrical anomalies in the test data that adversely influenced the integrated velocity responses. A further discussion of data anomalies is provided in the appendix. The floor-level velocity responses for the crew and troop seat locations and at FS 182 agree well with the test data at both 0.045 and 0.095 s. The accuracy of the predicted floor-level responses is more important than at other locations because the floor-level acceleration pulse is transmitted through the seats to the occupants.

6.4. Predicted Landing Gear Forces

The predicted landing gear forces for the main and nose gears are shown in figure 59. The left gear tire impacts at time 0.0, the right gear at 0.016 s, and the nose gear at 0.068 s. These times correlate well with the measured values shown in table 8, which are 0.0, 0.012, and 0.069 s, respectively. The time between left and right gear contact is somewhat longer for the simulation than for the experiment because the main landing gears are farther apart in the model at the time of initial contact, as described in section 5.1, "Landing Gear Model."

6.5. Comparison of Predicted Acceleration Time Histories With Test Data

To remove the high frequency ringing from the low frequency crash pulse, both the predicted and experimental acceleration data were filtered by using a zero-phase 60-Hz digital low-pass Butterworth

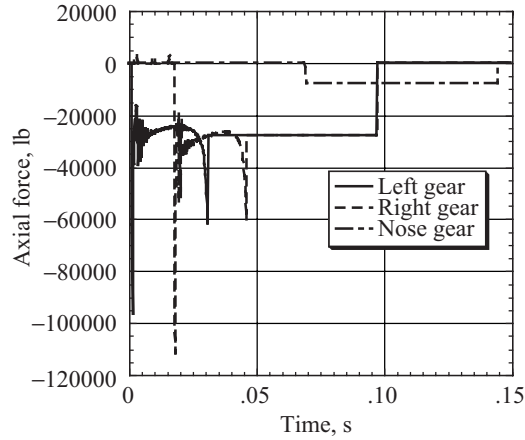
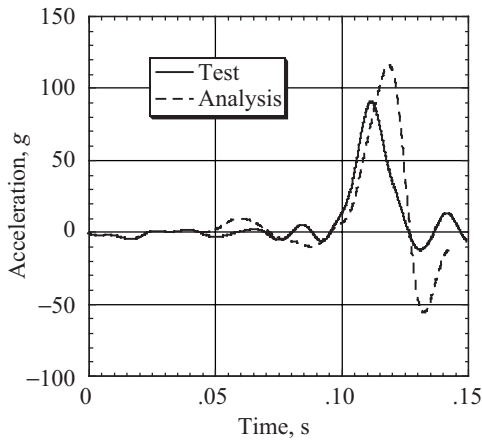
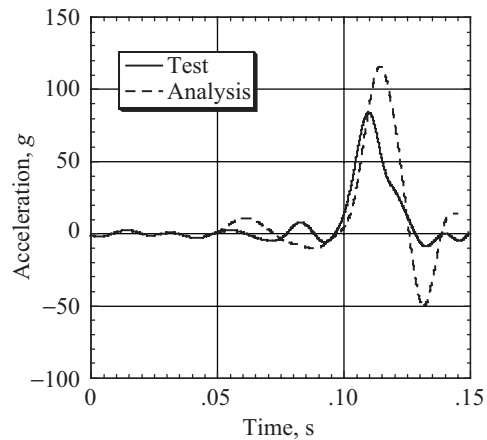


Figure 59. Predicted left, right, and nose gear axial force time histories.



(a) Pilot floor.

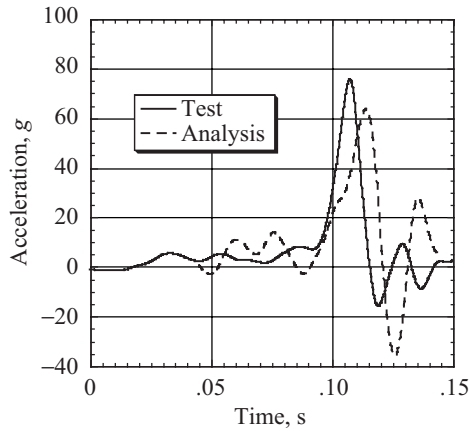


(b) Copilot floor.

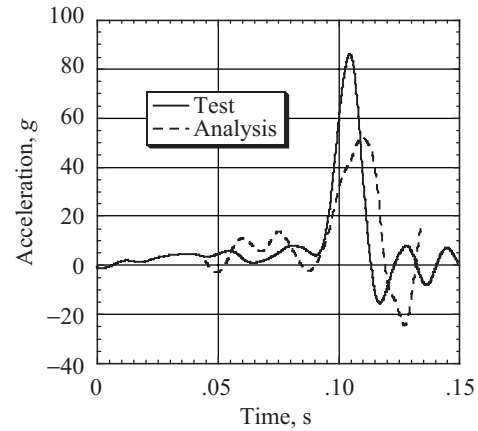
Figure 60. Predicted and measured vertical accelerations of the pilot and copilot floor locations.

filter generated by the mathematical code MATLAB (ref. 43). To produce zero-phase distortion in time, the algorithm was applied both forward and backward in time. The 60-Hz cutoff frequency was chosen because this frequency removes the high frequency oscillations from the data without any distortion in the integrated velocity response.

The accurate prediction of the floor-level acceleration responses is important because this information is needed for the proper design and evaluation of crashworthy seats. The predicted and measured vertical acceleration responses for the pilot and copilot seat floor locations are shown in figure 60. The experimental data are shown from time zero, corresponding to the time of left gear contact. The predicted values were obtained from the flexible model, which was initiated at 0.045 s. The time of initiation and the duration of the acceleration pulses compare quite favorably. The predicted peak acceleration for the pilot floor location was 115g, while the experimental value is 90g. For the copilot floor, the predicted peak acceleration (115g) also exceeded the experimental value (83g). In general, the predicted time of peak acceleration is somewhat delayed when compared with the experimental value. However, the simulation accurately predicted the pulse duration at both the pilot and copilot floor locations.

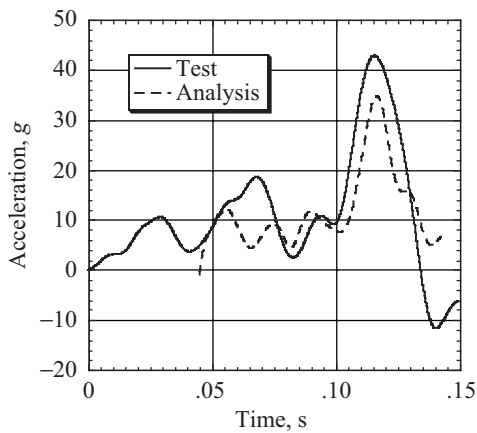


(a) Right troop seat floor.

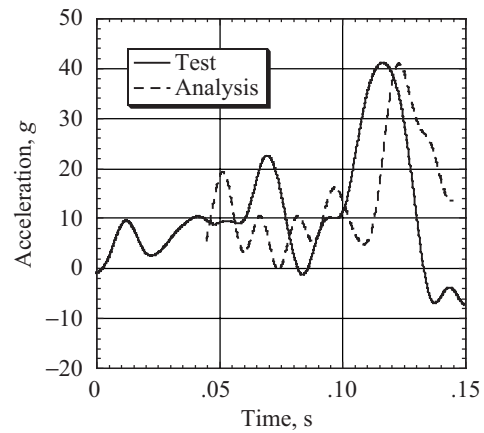


(b) Left troop seat floor.

Figure 61. Predicted and measured vertical accelerations at the troop seat floor locations.



(a) Right engine.

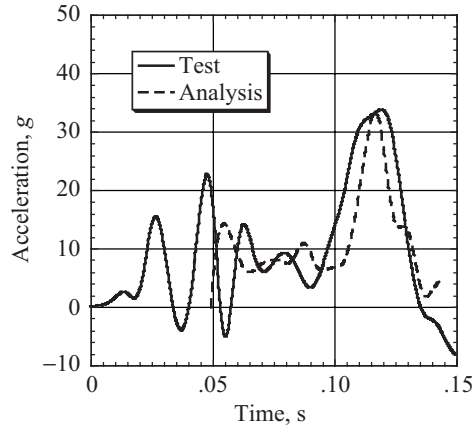


(b) Left engine.

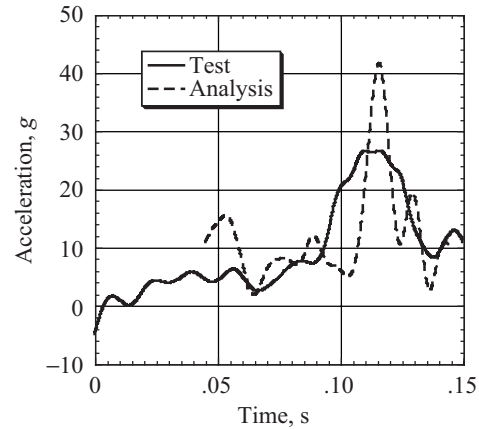
Figure 62. Predicted and measured acceleration responses for the right and left engines.

In contrast to the overprediction of crew floor accelerations, the predicted peak acceleration for the right troop seat floor was slightly lower ($64g$) than the experimental value ($75g$), as shown in figure 61(a). The predicted peak acceleration of the left troop seat floor ($51g$) was about 40 percent lower than the measured acceleration ($85g$), as shown in figure 61(b).

The acceleration time histories for the right and left engine masses are given in figure 62. The predicted and experimental peak accelerations for the right engine occurred at the same time, but the predicted peak value was slightly lower in magnitude than the experimental peak. Conversely, the predicted peak acceleration for the left engine matched the experimental magnitude ($41g$); however, the response was out of phase by 0.01 s.



(a) Top of right main gear.



(b) Top of bulkhead at FS 188.

Figure 63. Predicted and measured acceleration responses of the top of the right main gear and the top of the bulkhead at FS 188.

Table 10. Predicted and Experimental Peak Accelerations at Nine Locations

Location	Peak acceleration, g		
	Test	Analysis	Percent difference
Pilot seat floor	90.1	115.6	-28.4
Copilot seat floor	82.8	114.9	-38.8
Right main gear (top)	33.8	33.2	1.6
Right engine	42.8	34.7	18.9
Left engine	40.9	40.7	0.5
Right troop floor	75.4	63.6	15.7
Left troop floor	85.6	51.7	39.6
Rotor head	27.4	47.1	-71.8
Floor at FS 182	61.1	53.7	12.1

The predicted and measured vertical acceleration responses of the top of the right main landing gear and the top of the bulkhead at FS 188 are shown in figures 63(a) and (b), respectively. The comparisons shown in figures 60–63 are favorable, except for the bulkhead acceleration at FS 188. The predicted acceleration response at FS 188 is of shorter duration and higher magnitude than the measured acceleration. This result indicates that the model was too stiff in this location. A large number of vertical rod elements were used to model the fuselage wall and bulkhead at FS 188 in the original modal-vibration model. For the crash model, all rod elements in the subfloor were either removed or replaced with beam elements because rod elements are too stiff to represent the actual structural crash behavior. However, the rod elements in this location (FS 188) were not removed during conversion of the modal-vibration model due to time constraints. Because the upper rod elements at FS 188 were not removed, the model had a higher stiffness and exhibited less deformation than the actual structure, which contributed to the over-prediction of the peak acceleration.

A comparison of predicted and experimental peak acceleration values is shown in table 10 for the same nine locations used in the velocity comparisons that are listed in table 9. The data shown in table 10 do not reflect differences in phasing, i.e., time of occurrence of the peak acceleration values. The data

were obtained from the plots of filtered analytical and experimental data, and the same low-pass digital filter was used for both sets of data. As shown in table 10, the predicted peak acceleration values of five of the nine locations are within 20 percent of the experimental data. All of the predicted values are within ± 40 percent of the experimental data with the exception of the rotor head location.

The large overprediction in the peak acceleration of the rotor head may be attributed to two factors. First, as mentioned previously, a large number of vertical rod elements in this location were not removed during the conversion of the original modal-vibration model to a crash model. Because rod elements are generally too stiff, the model of the rotor head region exhibited less deformation than the actual structure, which contributed to the overprediction of the peak acceleration. Another factor that may have contributed to the large difference in peak acceleration at the rotor head location is the fact that the mass and inertial properties of the troop seats and occupants were represented as concentrated masses that were attached to nodes on the floor in the rear cabin area. However, in the test article the troop seats were mounted directly to the ceiling, just under the rotor head location. As indicated previously, a large downward deflection of the helicopter roof at the location of the wire-bender suspension system was observed in the high-speed film coverage. Because the mass of the troop seats and occupants was not accurately located in the model, this load path was not represented.

7. Observations and Lessons Learned

Some of the specific issues that influenced the test-analysis correlation are discussed in this section of the paper. The discussion is divided into two parts: issues related to the testing and instrumentation, and issues related to the modeling.

7.1. Testing and Instrumentation

The crash performance of the helicopter was adversely affected by the absence of the original energy-absorbing nose gear. As mentioned previously, a standard noncrashworthy nose gear was modified to maximize its energy absorption capabilities and mounted on the aircraft. Even with the retrofit, the energy-absorbing capabilities of the modified nose gear were only a small fraction of the capabilities of the original gear. As a result, the floor-level acceleration responses in the crew locations were higher in magnitude than those in the troop locations. Consequently, higher occupant loads were seen for the crew occupants than for the troop occupants, even though the crew occupants were secured in energy-absorbing seats.

The pendulum-style swing test that was used in conducting the ACAP helicopter crash test has been used successfully in performing numerous full-scale aircraft crash tests (ref. 7). However, one artifact of the testing technique is that it introduces a pitch angular velocity to the airframe. This rotational velocity must be considered in the simulation as an initial condition, just as the translational velocity components must be considered. The introduction of the rotational velocity was another factor that motivated the rigid-to-flexible modeling approach as it offered a fairly simple means of incorporating the pitch angular velocity.

Another testing issue was the complicated attitude of the airframe at initial ground contact. The intended impact attitude was 5° nose-up pitch, but the actual impact attitude was 6.25° nose-up pitch and 3.5° left-down roll. The higher than expected nose-up pitch angle resulted in a higher impact velocity in the crew floor location due to slapdown. Also, the roll condition resulted in uneven crushing of the landing gear and a minor slapdown on the right side of the airframe. Thus, the impact attitude affected the dynamic response of the airframe and had to be included in the simulation. The impact attitude at initial contact was accounted for in the model by adjusting the position of the impact surface.

The availability of test results from a 1987 vertical drop test of the Sikorsky ACAP helicopter (static test article) was a tremendous help in retrofitting the airframe to maximize its crashworthy performance. These retrofits were highly successful and resulted in increased crushing of the honeycomb stages of the main landing gear by preventing premature failures of the gear strut and drag beam attachments.

The instrumentation plan for the full-scale crash test specified 61 accelerometers, 5 load cells, 4 pressure transducers, 11 displacement transducers, and 1 strain gauge. In addition, the instrumented 50th percentile modified Hybrid III anthropomorphic dummy provided by USAARL contained 29 total channels of instrumentation. Of the 61 accelerometers, 15 were used in the three Hybrid II anthropomorphic dummies to record head, chest, and pelvic acceleration responses. Of the remaining 46 accelerometers, 23 were oriented in either the forward or side directions, leaving only 23 vertical accelerometers available for correlation with the analytical data. Note that the forward and side channels were not used for correlation because it would have been necessary to incorporate friction in the model and the coefficients of friction were unknown. Of the 23 vertical accelerometers, 4 were located on the crew and troop seats that were not physically represented in the model. Another 4 accelerometers did not provide data due to malfunctions; thus, only 15 channels were available for correlation. With the aid of hindsight, it is evident that additional vertical accelerometers were needed to more thoroughly characterize the airframe structural response. In addition, some redundancy in the instrumentation scheme would have helped verify the quality and accuracy of the test data.

Also, the 11 displacement transducers (string potentiometers) failed to provide data. Consequently, neither dynamic crushing of the subfloor nor displacement of the landing gear stages was measured. Another type of instrument to record dynamic displacement measurements during a crash test needs to be used to provide this important test data.

A large percentage of the instrumentation was used to characterize the seat and occupant response, because this information was needed to provide an accurate assessment of human injury potential. The data show that the crew and troop occupants experienced a loading environment that put them at moderate to high risk of injury. In addition, the data demonstrate that the copilot experienced a head strike, likely due to contact with his knees, resulting in a 16-percent probability of brain injury. Ultimately, the primary objective of crashworthiness is to increase survivability and minimize injury of the occupants. Although moderate to severe injuries would likely have occurred in this crash, the probability of a fatality is considered small.

Finally, another factor that affected the test data was the long umbilical cable used to send the analog signals from the airframe to the computers in the control room at the IDRF. This cable was approximately 800 ft long, which introduced electrical noise and other anomalies into the data. Currently, this technique for data acquisition during a full-scale crash test has been replaced by using onboard digital DAS units, which have proved to be extremely effective in subsequent full-scale crash tests performed at the IDRF.

7.2. Modeling

The focus of the crash simulation was to predict the impact response of the composite airframe, including the energy-absorbing main and nose landing gear. In addition, an effort was made to capture all of the initial conditions including impact velocity and pitch rate, as well as the pitch and roll impact attitude. However, several simplifying assumptions were required. For example, although an induced pitch angular velocity was determined, any roll or yaw rate was assumed to be zero.

The presence of the two-stage landing gear added tremendous complexity to the crash simulation and required the integration of a kinematic landing gear model with the structural finite element model. Developing the landing gear model and determining a method of maintaining its alignment required considerable resources and focused attention away from further refinements of the structural finite element model. The long length of time (approximately 0.1 s) between initial landing gear contact and fuselage contact was one reason that the two-stage, rigid-to-flexible modeling approach was implemented. The initial modeling approach was that, during stroking of the landing gear, the airframe was to be modeled as a rigid body. Then, just prior to fuselage contact, the nodal positions and velocities were to be written to a file and used as the initialization for the flexible model. However, this approach had to be modified because deformation and buckling of the tail cone occurred soon after initial landing gear contact. As a result of the tail cone failure, the modeling approach was changed such that the rigid model was executed for only 0.045 s. The two-stage, rigid-to-flexible modeling approach was implemented as the most efficient means of simulating the landing gear response. In addition, the transition between rigid to flexible models caused a slight discontinuity that occurred when the flexible model was initiated due to the instantaneous onset of the full landing gear force. Several techniques to minimize this discontinuity (an acceleration spike at the transition point from the rigid to flexible models) were investigated, such as ramping the honeycomb force over multiple time steps. However, none of these approaches were completely effective.

The rigid-to-flexible modeling approach, along with the other simplifications, did introduce some inaccuracies into the model. For example, during the crash test, the tail deformed and began to fail soon after the landing gear forces were applied and before fuselage contact with the ground. However, in the current modeling approach, the fuselage tail was represented as a rigid body for the first 0.045 s of the simulation. Consequently, the simulation did not predict the deformation of the tail from initial contact to 0.045 s. The rigid-to-flexible modeling approach was used because it offered an efficient means of introducing the pitch angular velocity. Another approach to account for the angular velocity would have been to write an external subroutine to calculate the initial x -, y -, and z -components of velocity in the global axis system for each node in the model.

It is often difficult to use the raw, or even the filtered, acceleration responses to understand the physics of the impact event. In most cases, it is better to examine and compare the velocity responses. Kinetic energy is proportional to velocity squared, hence inaccuracies in velocity are quite important. Because the helicopter had a pitch rate about the CG induced by the pendulum-swing test method, each longitudinal point on the helicopter had a different vertical component of velocity. Any inaccuracy in the landing gear forces, landing gear mechanism, and in the landing gear and tire friction (which was ignored) during the rigid body phase causes not only the CG velocity to be incorrect, but also the rotational velocity about the CG to vary incorrectly. The results shown in table 9 indicate that the model predicted the experimental velocities at nine different locations on the airframe extremely well. In particular, the predicted floor-level velocity responses closely matched the test data at both 0.045 and 0.095 s. The accuracy of the predicted floor-level responses is more important than at other locations because the floor-level acceleration pulse is transmitted through the seats to the occupants.

The results shown in table 10 appear to raise questions regarding the accuracy of the analytical results. However, several factors must be considered in the evaluation of these data. Correlation between analytical predictions generated from a crash simulation and transient dynamic test data is not straightforward. In general, dynamic data obtained from a full-scale crash test contain high frequency oscillations that often mask the underlying crash pulse. Also, the frequency responses of the transducer, DAS, and the actual ACAP helicopter are not the same as the frequency response of the model. Typically, the predicted responses contain more high amplitude, high frequency oscillations than the experimental data. In

addition, because the model is undamped, the high frequencies do not decay. Consequently, even though the same low-pass digital filter is applied to both the analytical and experimental data, an equivalent level of filtering is not achieved because both the frequency content and amplitude of the analytical and experimental data are different.

In the model, the seats and occupants were represented by using concentrated masses. However, this approximation does not accurately represent the loading provided to the floor and surrounding structure by the actual energy-absorbing seats. Essentially, the approach of modeling the seats and occupants as concentrated masses assumes that they behave as lumped masses attached directly to the floor. In fact, the inertial loading provided by the occupants is partially decoupled from the floor through the energy-absorbing seats. The only means of correcting this deficiency is to physically model the seats by using beam, shell, and spring elements and to simulate the anthropomorphic dummies by using a human occupant simulation code such as MADYMO (ref. 44) or Articulated Total Body (ATB) (ref. 45). This approach, which is now possible due to more efficient computer resources, would have added considerable complexity to the model and was not attempted.

Given all of the factors that can influence the test-analysis correlation, it is obviously a difficult task to quantify the overall accuracy of the crash simulation. In the present paper, the approach has been to present the model deformations and the predicted velocity and acceleration responses at several locations and compare these results with test data. In most cases, the crash simulation predicted the overall shape, magnitude, and duration of the experimental responses well. Where large discrepancies occurred, an attempt was made to verify the test data first and then to examine the model to understand the analytical results. Two recent publications, references 46 and 47, address the subject of test-analysis correlation. At this time, other methods to assess the correlation accuracy between analytical data generated from a detailed finite element crash simulation and transient dynamic test data are being investigated.

8. Concluding Remarks

This paper describes the full-scale crash test and simulation of a prototype composite helicopter. The test was performed at the Impact Dynamics Research Facility (IDRF) at NASA Langley Research Center in Hampton, Virginia. The helicopter was the flight test article built by Sikorsky Aircraft during the U.S. Army Advanced Composite Airframe Program (ACAP). The primary objective of the test was to obtain experimental data for validation of a nonlinear, explicit transient dynamic crash simulation. In addition, the airframe crash test served as a test bed for ancillary experiments including evaluation of a crash sensor and measurement of fuel tank dynamic pressures. The test conditions were 38-ft/s vertical and 32.5-ft/s horizontal velocity onto a flat, rigid impact surface with a 6.25° nose-up pitch and 3.5° left-down roll impact attitude. The crash test generated approximately 120 channels of data characterizing the seat and occupant responses, as well as the airframe structural response. In addition, the crash test was recorded with 13 high-speed 16-mm cameras. The high-speed films were essential in understanding the timing of the sequence of events that occurred during the crash test.

For the test, the aircraft was outfitted with two crew and two troop seats, and four instrumented anthropomorphic test dummies. The pilot (right crew) was a 50th percentile Hybrid II male dummy that was placed in a used commercial military-qualified helicopter seat that contained two invertube energy absorbers. The copilot (left crew) was a 50th percentile modified Hybrid III male dummy with a self-contained data acquisition system (DAS). The copilot dummy was secured in a used commercial military-qualified helicopter seat of a different design than the pilot seat. This seat contained six “torshock” energy absorbers. Two 50th percentile Hybrid II male dummies were used for the right and left troop occupants. These dummies were seated in ceiling-suspended troop seats with wire-bender

energy absorbers and were mounted in the rear cabin area. The occupant response data collected from the two crew and two troop anthropomorphic dummies were compared with existing human injury prediction criteria. These injury models include the Dynamic Response Index (DRI), the head injury criterion, the spinal load requirement defined in Federal Aviation Regulation Part 27.562(c), and a comparison of the occupant vertical acceleration data with the Eiband whole-body acceleration tolerance curve. The assessment of occupant injury indicates that the ACAP helicopter crash test resulted in a moderate to high level of risk for injury overall. Although some injuries would likely have occurred in this crash, the probability of fatalities is considered small.

A finite element model of the Sikorsky ACAP helicopter was developed by using the nonlinear, explicit transient dynamic code, MSC.Dytran. The objective of the crash simulation was to evaluate the capabilities of a commercial finite element code in predicting the response of a composite airframe subjected to impact loading through test and analysis correlation. The crash model of the ACAP helicopter was developed from an existing MSC.Nastran modal-vibration model of the helicopter. Considerable modifications were required to convert the original modal-vibration input deck to a model suitable for crash simulation.

Following the model conversion and modification, a two-stage, rigid-to-flexible simulation strategy was used to generate analytical predictions. Due to the relatively long pulse duration, a rigid fuselage model was executed in which an external user-written subroutine was used to compute the response of the landing gear, including both the oleo-pneumatic and crushable honeycomb stages. At 0.045 s, the nodal displacements and velocities were output. Then, a flexible structural model was executed with the nodal displacements and velocities of the rigid fuselage model used as initial conditions. This two-stage modeling approach worked well except for a slight discontinuity that occurred when the flexible model was initiated due to the sudden onset of the landing gear forces.

The initial correlation between the finite element simulation and the experimental results was a comparison of the sequence of events. In general, the simulation accurately predicted the time of right main gear contact, nose gear contact, tail cone failure, and the timing of the peak accelerations of the left and right troop seat floor, copilot floor, and the right engine locations within ± 0.007 s.

Comparisons of the predicted and experimental velocity responses were made for the right engine, the right main landing gear, and the copilot seat floor. Good agreement was obtained for all three locations. To further illustrate the velocity comparisons, the percentage differences between the predicted and experimental velocities at 0.045 and 0.095 s were calculated for nine difference locations on the airframe. These times were chosen for their significance in the simulation and in the sequence of events. The time of 0.045 s is the transition time between the rigid and flexible simulations and the time of 0.095 s is just prior to fuselage contact with the ground. The velocity data from the rigid simulation at 0.045 s agree extremely well with the experimental values (within ± 5 percent). The floor-level velocity responses for the crew and troop seat locations and at FS 182 agree well with the test data at both 0.045 and 0.095 s. The accuracy of the predicted floor-level responses is especially important because the floor-level acceleration pulse is transmitted through the seats to the occupants.

Comparisons of the predicted and experimental acceleration responses at several locations on the fuselage were made. For these comparisons, both the experimental and predicted acceleration data were filtered by using a Butterworth 60-Hz low-pass digital filter. In general, the crash simulation accurately predicted the overall shape, magnitude, and pulse duration of the experimental acceleration responses. However, the predicted peak accelerations at the upper bulkhead and rotor head locations were substantially higher than the experimental data at those locations. The discrepancy was attributed to the large

number of rod elements that were unmodified from the original MSC.Nastran modal-vibration model. Typically, rod elements are extremely stiff and do not accurately reflect the response of the actual bulk-head beams. In addition, the crash simulation correctly predicted the subfloor crushing response and structural failures of the engine support beams. To further illustrate the level of agreement, a table of the percent differences in the predicted and experimental peak acceleration values was generated for nine locations on the airframe. The predicted peak acceleration values for five of the nine locations were within 20 percent of the experimental data. All of the predicted values were within ± 40 percent of the experimental data, with the exception of the rotor head location. Overall, the level of agreement obtained between test and analysis builds confidence in the future use of nonlinear, explicit transient dynamic finite element codes as a crashworthy design and evaluation tool.

References

1. Noor, A. K.; and Carden, H. D., eds.: *Computational Methods for Crashworthiness*. NASA CP-3223, 1993.
2. Gamon, M.; Wittlin, G.; and LaBarge, B.: KRASH 85 User's Guide—Input/Output Format. Final Report DOT/FAA/CT-85/10, May 1985.
3. *LS-DYNA3D User's Manual*. Livermore Software Technology Co., 1997.
4. *MSC.DYTRAN User's Manual Version 4.0*. MacNeal-Schwendler Corp., 1997.
5. *PAM-CRASH*. Engineering Systems International SA, F-94588 Rungis, France.
6. Jones, L. E.: Overview of the NASA Systems Approach to Crashworthiness Program. *Proceedings of the 58th American Helicopter Society Annual Forum*. AHS, 2002.
7. Vaughan, V. L.; and Alfaro-Bou, E.: *Impact Dynamics Research Facility for Full-Scale Aircraft Crash Testing*. NASA TN D-8179, 1976.
8. Jackson, K. E.; and Fasanella, E. L.: A Survey of Research Performed at NASA Langley Research Center's Impact Dynamics Research Facility. AIAA-2003-1896, April 2003.
9. Kay, B. F.; and Maass, D.: Airframe Preliminary Design for an Advanced Composite Airframe Program. USAAVRADCOM-TR-80-D-35A, U.S. Army, March 1982.
10. Perschbacher, J. P.; Clarke, C.; Furnes, K.; and Carnell, B.: Advanced Composite Airframe Program (ACAP) Militarization Test and Evaluation (MT&E): Volume V—Airframe Drop Test. USAATCOM-TR-88-D-22E, U.S. Army, March 1996.
11. Thomson, D. T.; and Clarke, C. W.: Advanced Composite Airframe Program (ACAP) Militarization Test and Evaluation (MT&E): Volume I—Landing Gear Drop Test. USAAVSCOM-TR-88-D-22A, U.S. Army, Aug. 1989.
12. Cronkhite, J. D.; and Mazza, L. T.: Bell ACAP Full-Scale Aircraft Crash Test and KRASH Correlation. *Proceedings of the 44th American Helicopter Society Annual Forum*, AHS, 1988.
13. Light Fixed- and Rotary-Wing Aircraft Crash Resistance. MIL-STD-1290A (AV), Sept. 1988.
14. Anthropomorphic Test Dummy. Chapter 5, Code of Federal Regulations, Title 49, Part 572, vol. 38, no. 62, U.S. Government Printing Office, 1973, pp. 8455–8458.

15. Backaitis, S. H.; and Mertz, H. J.; eds.: *Hybrid III: The First Human-Like Crash Test Dummy*. SAE, 1994.
16. *Working Model 2D User's Manual Version 4.0*. Knowledge Revolution, 1996.
17. Boitnott, R. L.; and Jones, L. E.: NASA Langley Research Center's Impact Dynamics Research Facility Full-Scale Crash Test Procedures. Presented at *Proceedings of the 3rd KRASH Users Conference*, Jan. 2001.
18. Boitnott, R. L.; Jackson, K. E.; Fasanella, E. L.; and Kellas, S.: Full-Scale Crash Test of the Sikorsky Advanced Composite Airframe Program Helicopter. *Proceedings of the 56th American Helicopter Society Annual Forum*. AHS, 2000.
19. Boitnott, R. L.; Bolukbasi, A. O.; and Kellas, S.: Helicopter Fuel Bladder Drop Test and Analyses, *Proceedings of the 50th American Helicopter Society Annual Forum*, AHS, 1994.
20. Instrumentation for Impact Test—Part 1: Electronic Instrumentation, RP-J211/1, SAE, March 1995.
21. Airworthiness Standard: Normal Category Rotorcraft. Emergency Landing Dynamics, Code of Federal Regulations, Part 27.562, U.S. Government Printing Office, 1991, pp. 487–488.
22. Stech, E. L.; and Payne, P. R.: Dynamic Models of the Human Body. AAMRL-TR-66-157, U.S. Air Force, 1969.
23. Brinkley, J. W.; and Shaffer, J. T.: Dynamic Simulation Techniques for the Design of Escape Systems: Current Applications and Future Air Force Requirements. AAMRL-TR-71-292, U.S. Air Force, Dec. 1971.
24. Coltman, J. W.; Van Ingen, C.; Johnson, N. B.; and Zimmerman, R. E.: Crash Survival Design Guide, Volume II—Aircraft Design Crash Impact Conditions and Human Tolerance. USAAVSCOM-TR-89-D-22B, U.S. ARMY, Dec. 1989.
25. Brinkley, J. W.; and Mosher, S. E.: Development of Acceleration Exposure Limits to Advanced Escape Systems. *Implications of Advanced Technologies for Air and Spacecraft Escape*, AGARD-CP-472, 1989.
26. Mosher, S. E.: *DYNRESP Six Degree-of-Freedom Model for Injury-Risk Evaluation User's Manual*. NASA Johnson Space Center, 1993.
27. Occupant Crash Protection, Federal Motor Vehicle Safety Standard No. 208. Code of Federal Regulations, Title 49, Part 571.208, U.S. Government Printing Office, 1987.
28. Human Tolerance to Impact Conditions as Related to Motor Vehicle Design. RP-J885, SAE, April 1980.
29. Gadd, C. W.: Use of a Weighted-Impulse Criterion for Estimating Injury Hazard. *Proceedings of the Tenth Stapp Car Crash Conference*, SAE, 1966.
30. Nusholtz, G. S.; Kaiker, P. S.; and Lehman, R. J.: Critical Limitations on Significant Factors in Head Injury Research. *Proceedings of the 30th Stapp Car Crash Conference*, SAE, Oct. 1986, pp. 237–267.
31. Eiband, A. M.: *Human Tolerance to Rapidly Applied Accelerations: A Summary of the Literature*. NASA TM-5-19-59E, 1959.
32. Desjardins, S. P.; Zimmerman, R. E.; Bolukbasi, A. O.; and Merritt, N. A.: Crash Survival Design Guide, Volume IV—Aircraft Seats, Restraints, Litters, and Cockpit/Cabin Delethalization. USAAVSCOM-TR-89-D-22B, U.S. Army, Dec. 1989.

33. Mertz, H. J.: Injury Assessment Values Used to Evaluate Hybrid III Response Measurements. NIHTSA Docket 74-14, Notice 32, Enclosure 2, Attachment I, Part III, General Motors Submission USG 2284, March 1984.
34. Jackson, K. E.; Fasanella, E. F.; Boitnott, R. L.; and McEntire, B. J.: Occupant Responses in a Full-Scale Crash Test of the Sikorsky ACAP Helicopter. *Proceedings of the 58th American Helicopter Society Annual Forum*. AHS, 2002.
35. Fasanella, E. L.; Boitnott, R. L.; Jackson, K. E.; and McEntire, J.: Occupant Responses in a Full-Scale Crash Test of an ACAP Helicopter. *Proceedings of the NATO Applied Vehicle Technology Panel's Symposium on Combat Survivability of Air, Sea, and Land Vehicles*. NATO, 2002.
36. Lahey, R. S.; Miller, M. P.; and Reymond, M.: *MSC/NASTRAN Reference Manual, Version 68*. MacNeal-Schwendler Corp., 1994.
37. Stebbins, R. F.; and Twomey, W. J.: *Plan, Formulate, and Discuss a NASTRAN Finite Element Model of the Sikorsky ACAP Helicopter Airframe*. NASA CR-182059, 1990.
38. *MSC.PATRAN, DYTRAN Preference Guide*. MacNeal-Schwendler Corp., 1996.
39. Lyle, K. H.; Jackson, K. E.; and Fasanella, E. L.: Simulation of Aircraft Landing Gears With a Nonlinear Transient Dynamic Finite Element Code. *J. Airc.*, vol. 39, no. 1, 2002, pp. 142–147.
40. Lyle, K. H.; Jackson, K. E.; and Fasanella, E. L.: Development of an ACAP Helicopter Impact Model. *J. American Helicopter Soc.*, vol. 45, no. 2, 2000, pp. 137–142.
41. Fasanella, E. L.; Jackson, K. E.; and Lyle, K. H.: Finite Element Simulation of a Full-Scale Crash Test of a Composite Helicopter. *J. American Helicopter Soc.*, vol. 47, no. 3, July 2002, pp. 156–168.
42. Fasanella, E. L.; Boitnott, R. L.; Lyle, K. H.; and Jackson, K. E.: Full-Scale Crash Test and Simulation of a Composite Helicopter. *Int. J. Crashworthiness*, vol. 6, no. 4, 2001, pp. 485–498.
43. *MATLAB User's Guide*. MathWorks, Inc., 1992.
44. *MADYMO Users' Manual 3-D Version 4.3*. The Dutch Institute of Applied Scientific Research, 1988.
45. Obergefell, L. A.; Gardner, T. R.; Kaleps, I.; and Fleck, J. T.: Articulated Total Body Model Enhancements, Volume 2: User's Guide. AAMRL-TR-88-043, U.S. Air Force, Jan. 1988.
46. Lyle, K. H.; Bark, L. W.; and Jackson, K. E.: Evaluation of Test/Analysis Correlation Methods for Crash Applications. *Proceedings of the 57th American Helicopter Society Annual Forum*. AHS, 2001.
47. Lyle, K. H.; Bark, L.; and Jackson, K. E.: Evaluation of Test/Analysis Correlation Methods for Crash Applications. *J. American Helicopter Soc.*, vol. 47, no. 4, 2002, pp. 219–232.

Appendix

Raw and Filtered Test Data

This appendix contains plots of the unfiltered test data obtained from the ACAP helicopter full-scale crash test. Most of the vertical acceleration channels have been integrated to obtain the velocity time history responses. A list of all instrumentation used in the crash test is provided in table A1. For some channels, serious anomalies in the test data were found. These channels are noted in the remarks in table A1 and are not included in this appendix. A discussion of electrical anomalies in transient dynamic test data is provided in section A1 to further clarify this issue. In addition to the unfiltered data, filtered data are provided. For most channels, the data were filtered by using a 60-Hz digital zero-phase low-pass Butterworth filter. The 60-Hz cutoff frequency was chosen because this frequency removes the high frequency oscillations from the data without any distortion in the integrated velocity response. The occupant head and chest responses were filtered by using a 1000-Hz low-pass digital filter, as specified by SAE J211/1 (ref. 21). This appendix contains the following sections:

- A1. Discussion of Electrical Anomalies in Transient Dynamic Test Data
- A2. Pilot Dummy Responses
- A3. Copilot Dummy Responses (NASA)
- A4. Copilot Dummy Responses (USAARL)
- A5. Right and Left Troop Dummy Responses
- A6. Fuselage Structural Responses
- A7. Rotor Transmission and Engine Responses
- A8. Landing Gear Responses
- A9. Fuel Tank Pressure Responses
- A10. Tail Continuity Gauge

Table A1. Instrumentation Description

Sensor location	Sensor type	Measurement	Range	Remarks
Pilot head	Accelerometer	Vertical acceleration	$\pm 100g$	Lost channel
Pilot head	Accelerometer	Forward acceleration	$\pm 100g$	
Pilot head	Accelerometer	Side acceleration	$\pm 100g$	
Pilot chest	Accelerometer	Vertical acceleration	$\pm 100g$	
Pilot chest	Accelerometer	Forward acceleration	$\pm 100g$	
Pilot chest	Accelerometer	Side acceleration	$\pm 100g$	
Pilot pelvis	Accelerometer	Vertical acceleration	$\pm 100g$	
Pilot pelvis	Accelerometer	Forward acceleration	$\pm 100g$	
Pilot pelvis	Accelerometer	Side acceleration	$\pm 100g$	
Pilot seat pan	Accelerometer	Vertical acceleration	$\pm 200g$	
Pilot seat pan	Accelerometer	Forward acceleration	$\pm 200g$	
Pilot lumbar load	Load cell	Compressive force	5000 lb	
Pilot lap belt	Load cell	Tensile force	3000 lb	
Pilot shoulder belt	Load cell	Tensile force	3000 lb	

Table A1. Continued

Sensor location	Sensor type	Measurement	Range	Remarks
Copilot seat pan	Accelerometer	Vertical acceleration	±200g	Lost channel
Copilot seat pan	Accelerometer	Forward acceleration	±200g	
Copilot lumbar load	Load cell	Compressive force	5000 lb	
Copilot lap belt	Load cell	Tensile force	3000 lb	
Copilot shoulder belt	Load cell	Tensile force	3000 lb	
Copilot head	Accelerometer	Forward acceleration	±500g	USAARL
Copilot head	Accelerometer	Side acceleration	±500g	USAARL
Copilot head	Accelerometer	Vertical acceleration	±500g	USAARL
Copilot head		Pitch rate	±50 krad/s	USAARL
Copilot head/neck		Forward moment	±2500 in-lb	USAARL
Copilot head/neck		Side moment	±2500 in-lb	USAARL
Copilot head/neck	Load cell	Forward shear force	±2000 lb	USAARL
Copilot head/neck	Load cell	Side shear force	±2000 lb	USAARL
Copilot head/neck	Load cell	Vertical tensile force	±2000 lb	USAARL
Copilot torso	Accelerometer	Forward acceleration	±200g	USAARL
Copilot torso	Accelerometer	Side acceleration	±200g	USAARL
Copilot torso	Accelerometer	Vertical acceleration	±200g	USAARL
Copilot torso	Load cell	Forward shear force	±3000 lb	USAARL
Copilot torso	Load cell	Side shear force	±3000 lb	USAARL
Copilot torso	Load cell	Vertical tensile force	±3000 lb	USAARL
Copilot torso		Forward moment	±4000 in-lb	USAARL
Copilot torso		Side moment	±4000 in-lb	USAARL
Copilot torso		Vertical moment	±3000 in-lb	USAARL
Copilot torso sternum	Accelerometer	Forward acceleration	±200g	USAARL
Copilot torso sternum	Accelerometer	Vertical acceleration	±200g	USAARL
Copilot lumbar	Load cell	Forward shear force	±3000 lb	USAARL
Copilot lumbar	Load cell	Side shear force	±3000 lb	USAARL
Copilot lumbar region	Load cell	Vertical force	±3000 lb	USAARL
Copilot pelvis/lumbar		Forward moment	±5000 in-lb	USAARL
Copilot pelvis/lumbar		Side moment	±5000 in-lb	USAARL
Copilot lumbar region		Vertical moment	±4000 in-lb	Lost channel
Copilot floor	Accelerometer	Forward acceleration	±400g	USAARL
Copilot floor	Accelerometer	Side acceleration	±400g	USAARL
Copilot floor	Accelerometer	Vertical acceleration	±400g	USAARL
Right troop chest	Accelerometer	Vertical acceleration	±100g	
Right troop chest	Accelerometer	Forward acceleration	±100g	
Right troop chest	Accelerometer	Side acceleration	±100g	
Right troop seat pan	Accelerometer	Vertical acceleration	±200g	
Left troop chest	Accelerometer	Vertical acceleration	±100g	
Left troop chest	Accelerometer	Forward acceleration	±100g	
Left troop chest	Accelerometer	Side acceleration	±100g	
Left troop seat pan	Accelerometer	Vertical acceleration	±200g	

Table A1. Continued

Sensor location	Sensor type	Measurement	Range	Remarks
Pilot seat floor	Accelerometer	Vertical acceleration	±750g	Lost channel <

Table A1. Concluded

Sensor location	Sensor type	Measurement	Range	Remarks
Nose gear top	Accelerometer	Vertical acceleration	$\pm 750g$	Lost channel
Nose gear hub	Accelerometer	Vertical acceleration	$\pm 750g$	Lost channel
Left main gear hub	Accelerometer	Vertical acceleration	$\pm 750g$	
Left main gear top	Accelerometer	Vertical acceleration	$\pm 750g$	
Right main gear hub	Accelerometer	Vertical acceleration	$\pm 750g$	
Right main gear top	Accelerometer	Vertical acceleration	$\pm 750g$	
Left gear honeycomb	String potentiometer	Displacement	20 in.	Lost channel
Left gear hub	String potentiometer	Displacement	20 in.	Lost channel
Right gear honeycomb	String potentiometer	Displacement	50 in.	Lost channel
Right gear hub	String potentiometer	Displacement	50 in.	Lost channel
Nose gear	String potentiometer	Displacement	20 in.	Lost channel
Fuel tank bottom right	Pressure gauge	Pressure	1000 psi	Lost channel
Fuel tank bottom left	Pressure gauge	Pressure	1000 psi	Lost channel
Fuel tank left inside	Pressure gauge	Pressure	500 psi	
Fuel tank right inside	Pressure gauge	Pressure	500 psi	
Tail continuity gauge	Strain gauge	Event marker		

A1. Discussion of Electrical Anomalies in Transient Dynamic Test Data

In addition to the actual physical data, electrical anomalies can be found in transient dynamic test data. These anomalies may be generated by electromagnetic interference, cross talk between channels, inadvertent overranging of the instrument itself, nonlinearity caused by exciting the resonance frequency of the accelerometer, overranging of the instrumentation caused by setting the voltage limits of amplifiers too low, short circuits due to cut or crimped wiring, and intermittent data caused by poor connectivity. It is often difficult to distinguish between electrical anomalies and good data; however, for some cases, electrical anomalies are immediately evident to an experienced researcher. During the ACAP helicopter crash test, electrical anomalies appeared in some channels. One example, illustrated in figure A1, is a force time history plot recorded by an anthropomorphic dummy lumbar load cell.

The high peaks that exceed 6000 lb are examples of electrical transients that are not part of the physical data. These transients appear in many of the data channels and the amplitude of the transients depends on the sensitivity of the instrument and the amplifier gain settings. Sometimes filtering the data will remove these electrical transients. However, filtering can sometimes mask an anomaly, making it appear as real physical data. As an example, the dummy load cell data in figure A1 are filtered with a 60-Hz low-pass filter, and the resulting plot is shown in figure A2. Note that in the filtered data, the peak of approximately 500 lb that occurs at 0.04 s looks like real physical data. However, because the ACAP fuselage did not impact the concrete surface until 0.098 s, this peak is not physical data, but an artifact of the filtered electrical anomaly.

Often, integrating an acceleration channel that has electrical anomalies will yield a nonphysical velocity change. Thus, integrating acceleration data to produce velocity plots is useful for data quality checking. Of course, before integrating the acceleration data, it is important to initialize the data to remove any offsets. An example of an accelerometer data channel from the ACAP test that has electrical anomalies

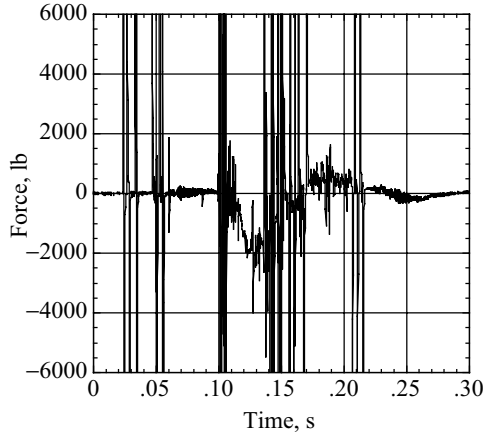


Figure A1. Electrical anomalies in dynamic load cell data.

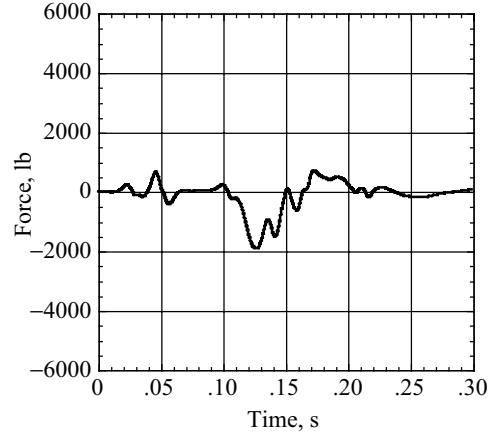


Figure A2. Lumbar load cell data filtered with 60-Hz low-pass digital filter.

similar to those seen in figure A1 is shown in figure A3. This plot shows the unfiltered vertical acceleration response of the left engine. The integrated velocity response is shown in figure A4, which indicates that between 0 and 0.12 s the velocity is being removed as expected. The velocity response crosses zero at approximately 0.12 s with a subsequent rebound to over 200 in/s. Thus, if the plot is accepted, the total velocity change including rebound for 0.125 s is $-466.6 \text{ in/s} - 200 \text{ in/s} = -666.6 \text{ in/s}$, which is a much higher value than would be expected. Also, the velocity response shown in figure A4 never returns to zero following the initial rebound, which is an artifact from integrating the electrical anomalies in the unfiltered acceleration data.

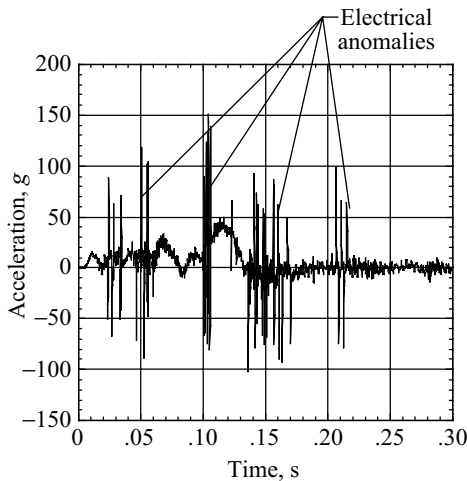


Figure A3. Unfiltered vertical acceleration response of the left engine with electrical anomalies.

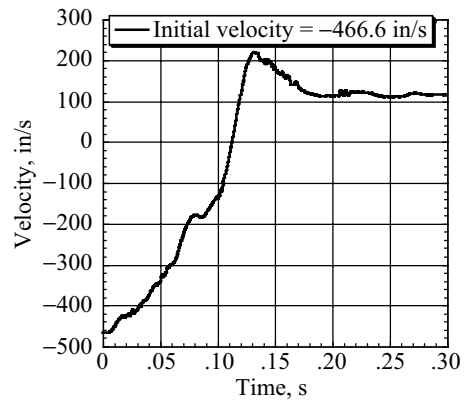


Figure A4. Vertical velocity response (integrated vertical acceleration) of the left engine.

Another example of problems with electrical anomalies in test data is shown in figure A5(a), which is the unfiltered vertical acceleration response of the fuselage bulkhead at FS 267. It is apparent from the figure that the DAS has stopped recording “real” test data from this accelerometer after approximately 0.15 s and is recording a digital signal that is oscillating about $-8g$. The filtered acceleration response is shown in figure A5(b). The velocity time history obtained by integrating the unfiltered acceleration data is a completely unrealistic response, as shown in figure A6.

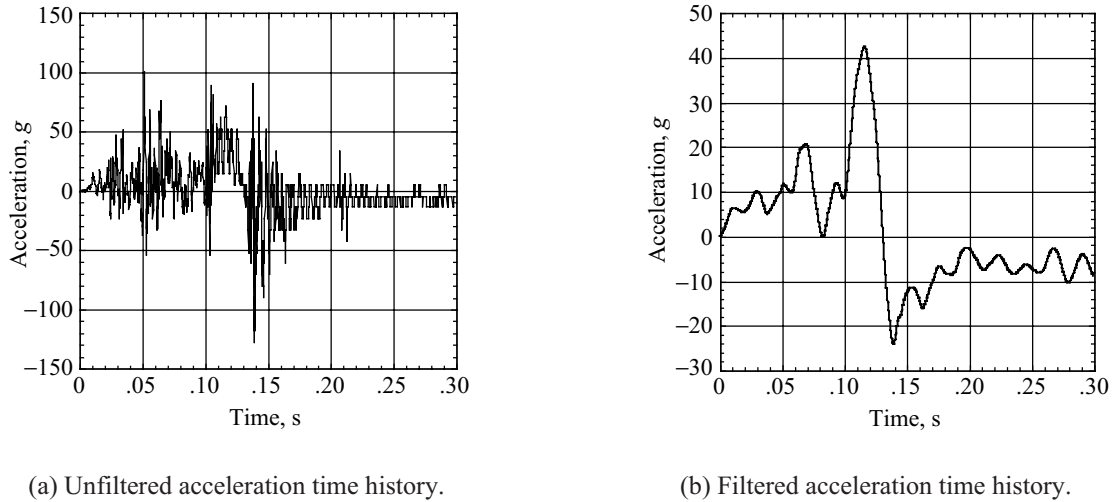


Figure A5. Acceleration response of the fuselage bulkhead at FS 267.

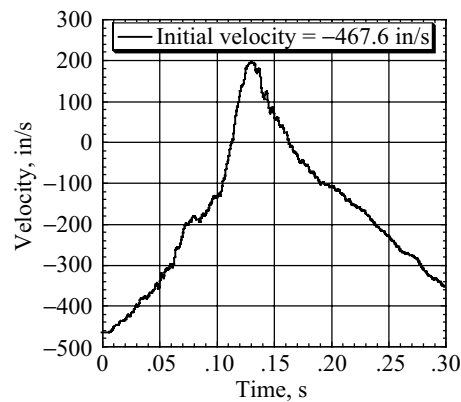


Figure A6. Vertical velocity response of the bulkhead at FS 267.

A2. Pilot Dummy Responses

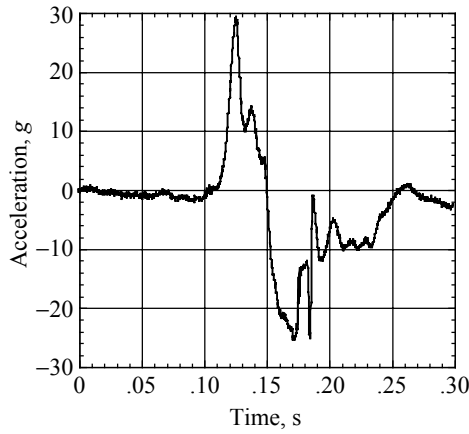


Figure A7. Unfiltered vertical acceleration response of the pilot head.

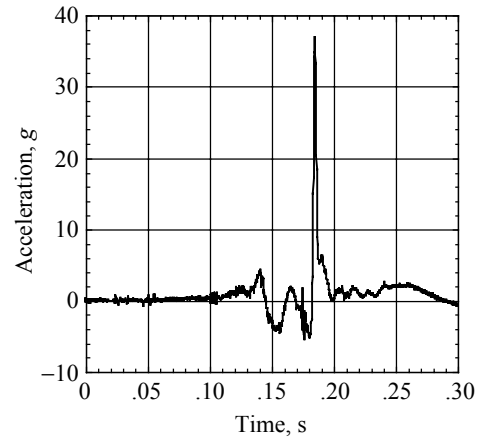


Figure A8. Unfiltered side acceleration response of the pilot head.

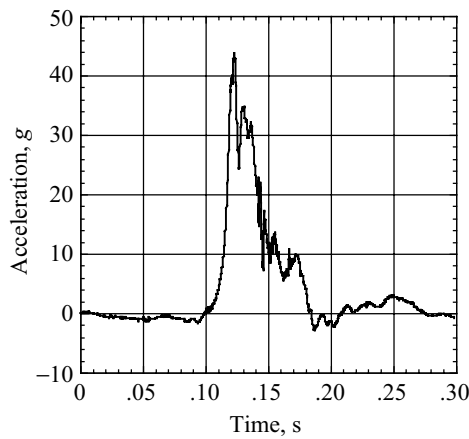


Figure A9. Unfiltered vertical acceleration response of the pilot chest.

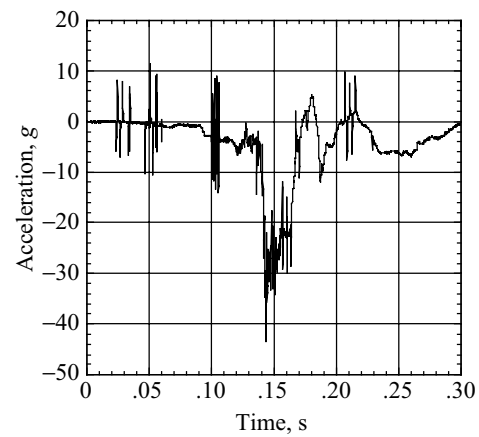


Figure A10. Unfiltered forward acceleration response of the pilot chest.

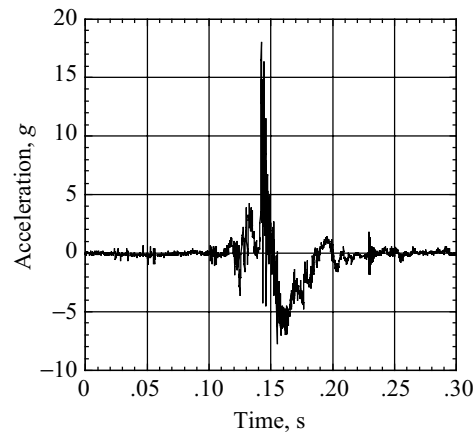
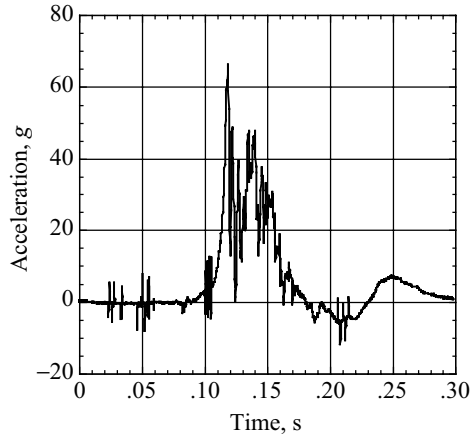
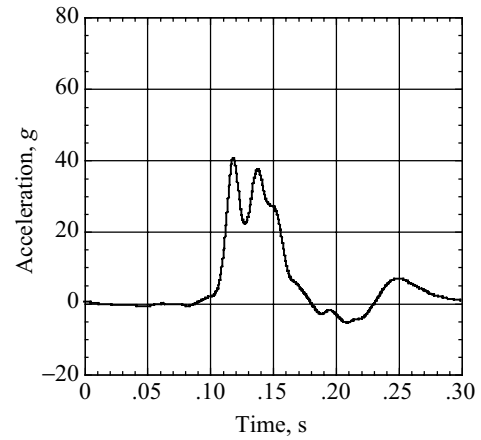


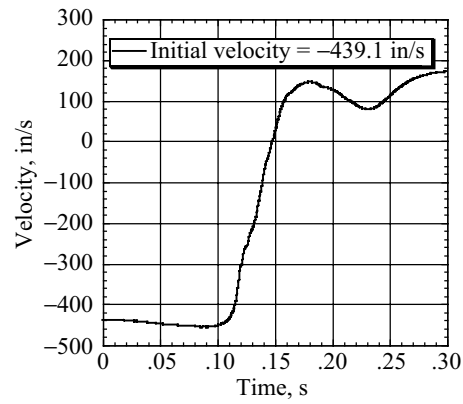
Figure A11. Unfiltered side acceleration response of the pilot chest.



(a) Unfiltered acceleration time history.



(b) Filtered acceleration time history.



(c) Velocity time history (integrated unfiltered acceleration).

Figure A12. Vertical acceleration and velocity responses of the pilot pelvis.

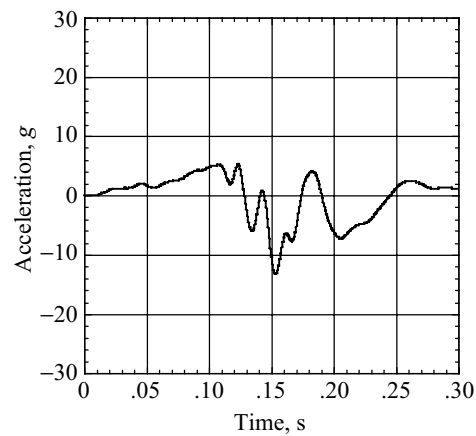
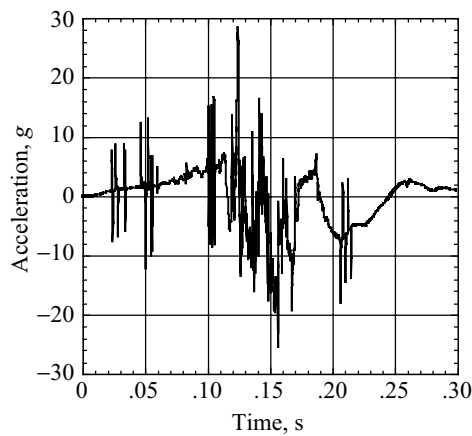


Figure A13. Unfiltered (left plot) and filtered (right plot) forward acceleration responses of the pilot pelvis.

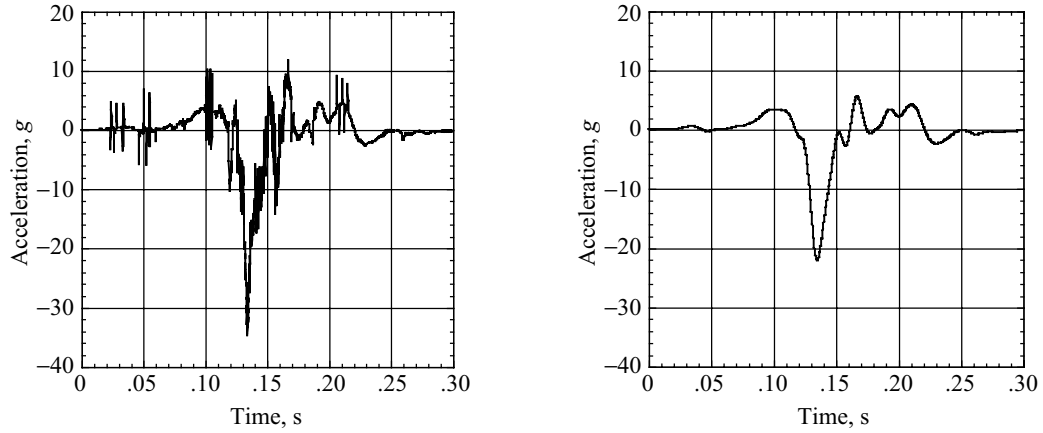
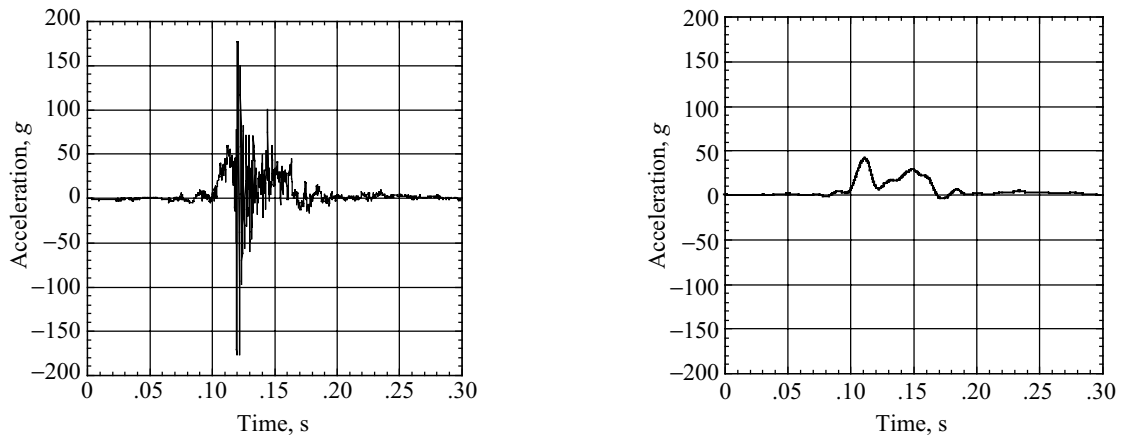
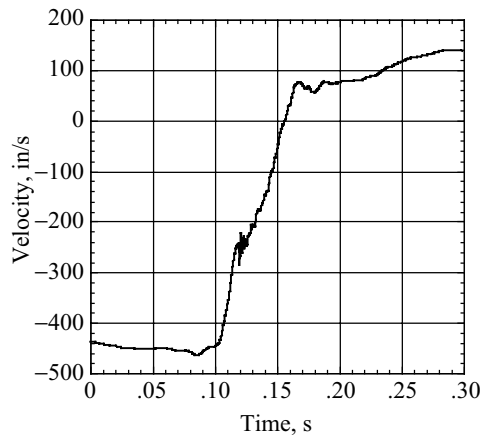


Figure A14. Unfiltered (left plot) and filtered (right plot) side acceleration responses of the pilot pelvis.



(a) Unfiltered acceleration time history.

(b) Filtered acceleration time history.



(c) Velocity time history (integrated unfiltered acceleration).

Figure A15. Vertical acceleration and velocity responses of the pilot seat pan.

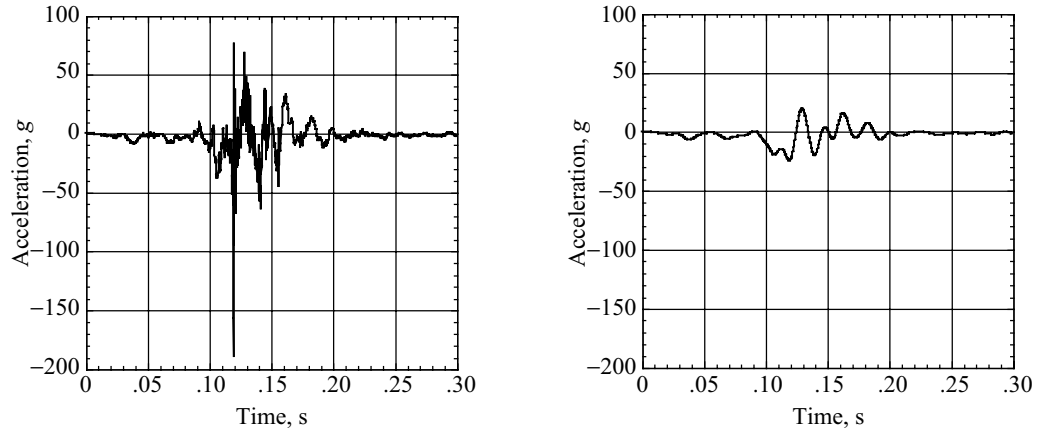


Figure A16. Unfiltered (left plot) and filtered (right plot) forward acceleration responses of the pilot seat pan.

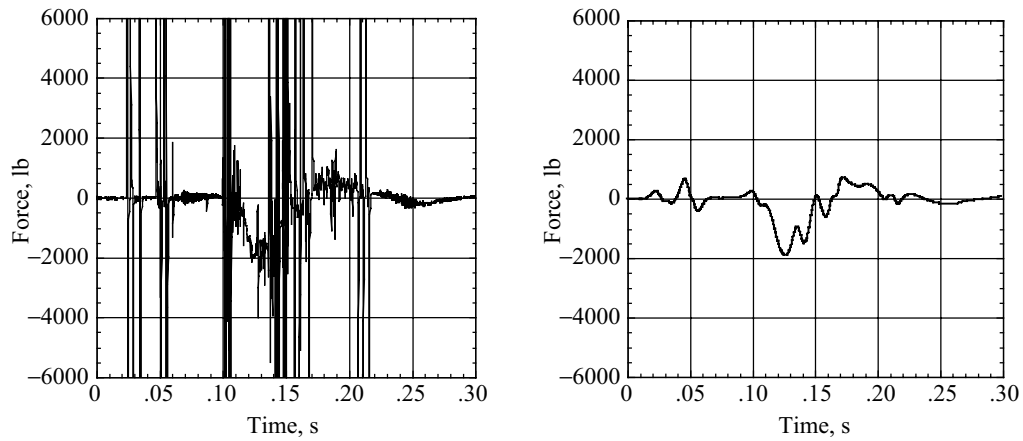


Figure A17. Unfiltered (left plot) and filtered (right plot) pilot lumbar load.

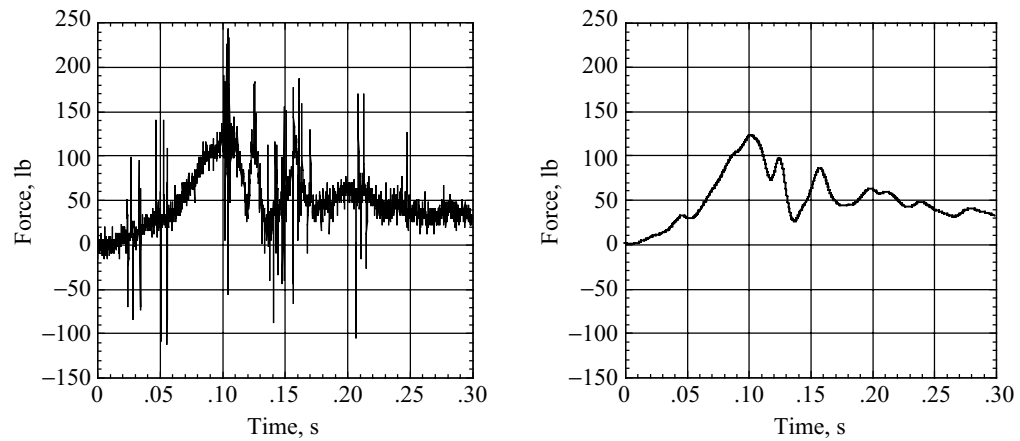


Figure A18. Unfiltered (left plot) and filtered (right plot) pilot lap belt load.

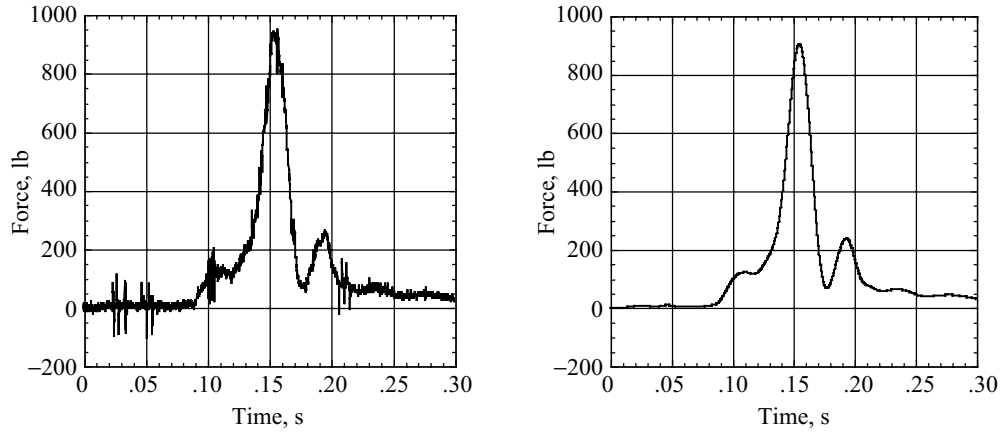
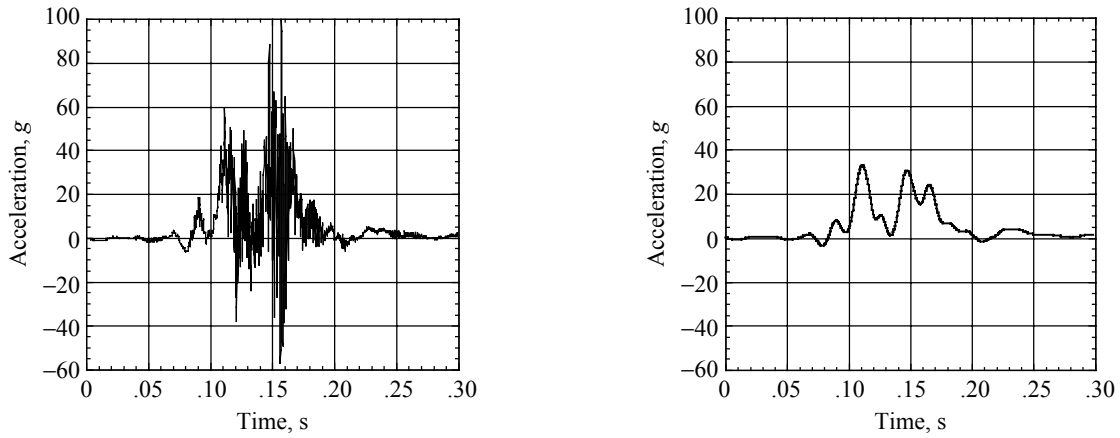


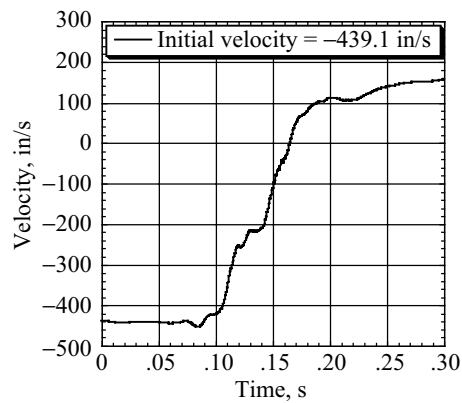
Figure A19. Unfiltered (left plot) and filtered (right plot) pilot shoulder belt load.

A3. Copilot Dummy Responses (NASA)



(a) Unfiltered acceleration time history.

(b) Filtered acceleration time history.



(c) Velocity time history (integrated unfiltered acceleration).

Figure A20. Vertical acceleration and velocity responses of the copilot seat pan.

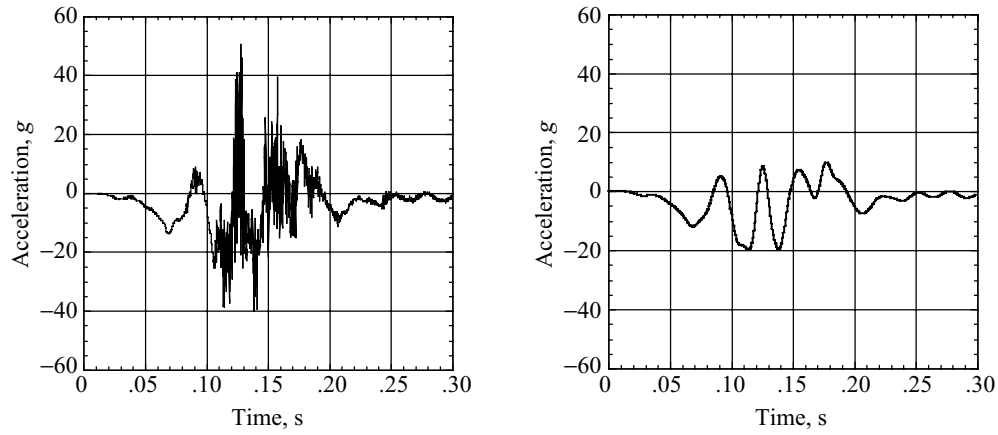


Figure A21. Unfiltered (left plot) and filtered (right plot) forward acceleration responses of the copilot seat pan.

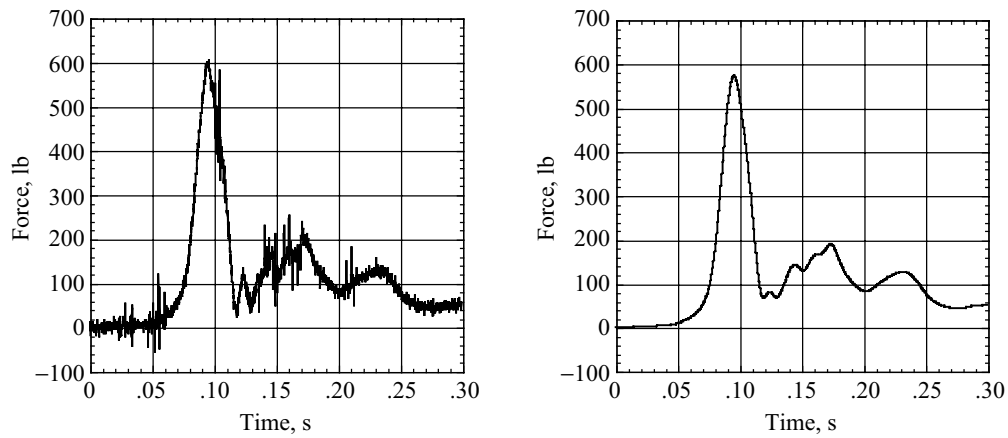


Figure A22. Unfiltered (left plot) and filtered (right plot) copilot lap belt load.

A4. Copilot Dummy Responses (USAARL)

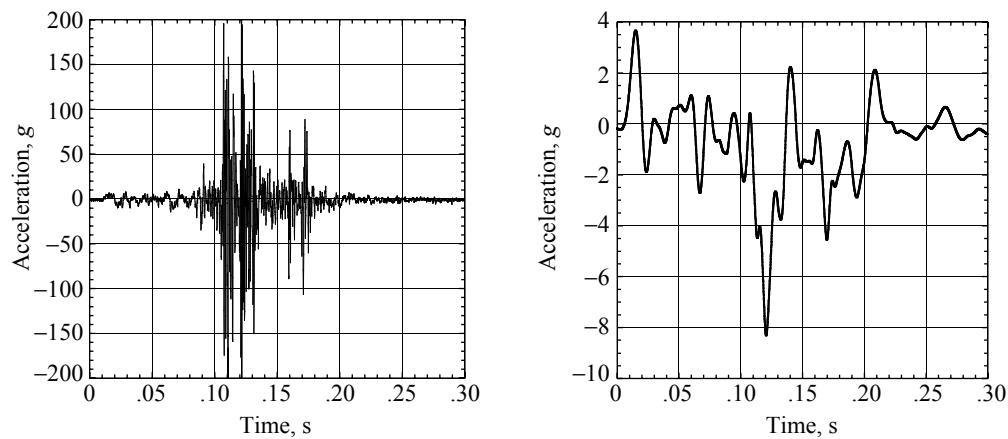


Figure A23. Unfiltered (left plot) and filtered (right plot) forward acceleration responses of the copilot seat floor.

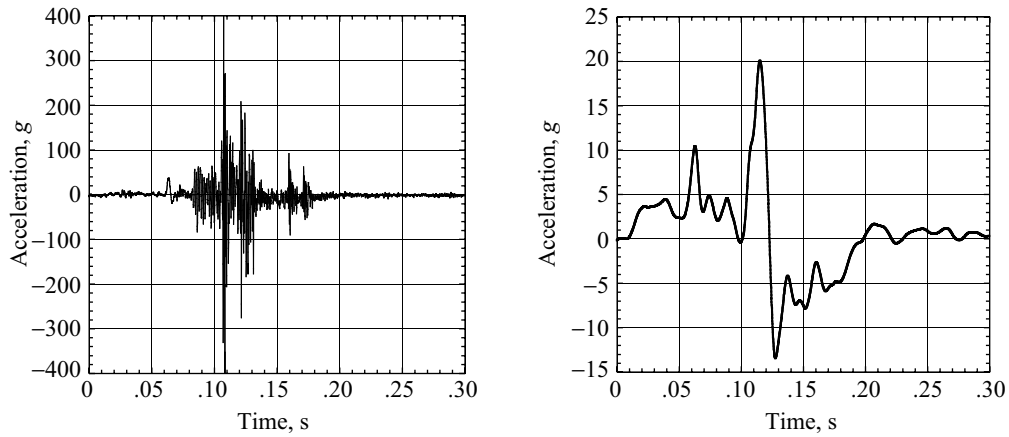
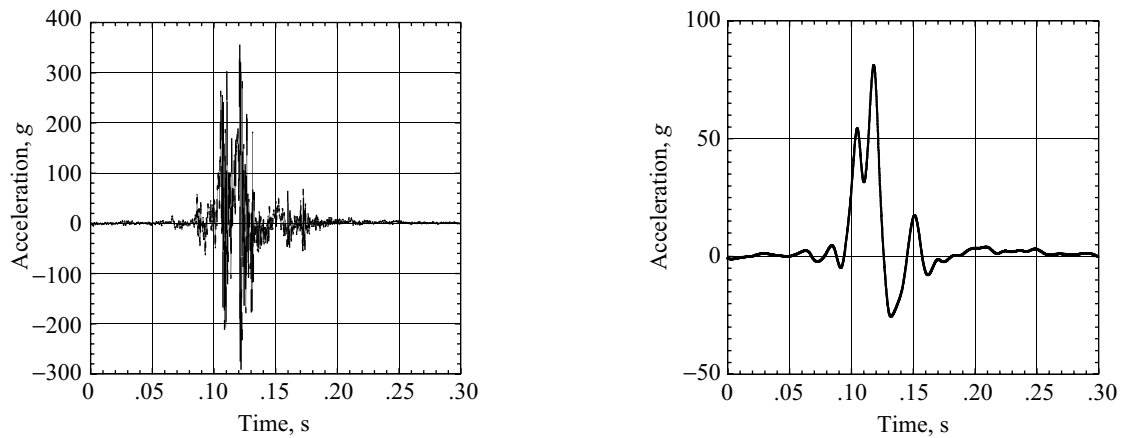
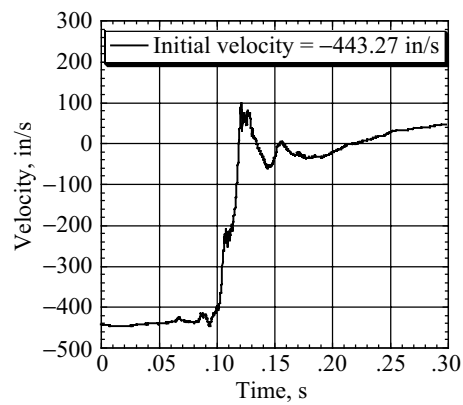


Figure A24. Unfiltered (left plot) and filtered (right plot) side acceleration responses of the copilot seat floor.



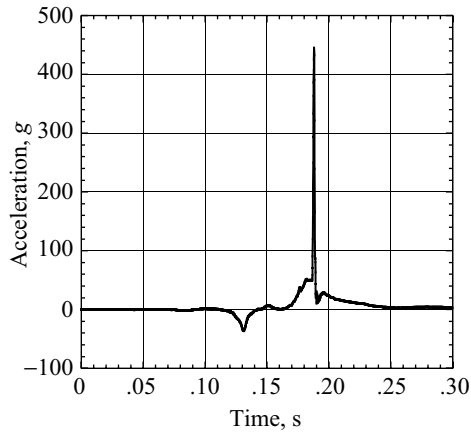
(a) Unfiltered acceleration time history.

(b) Filtered acceleration time history.

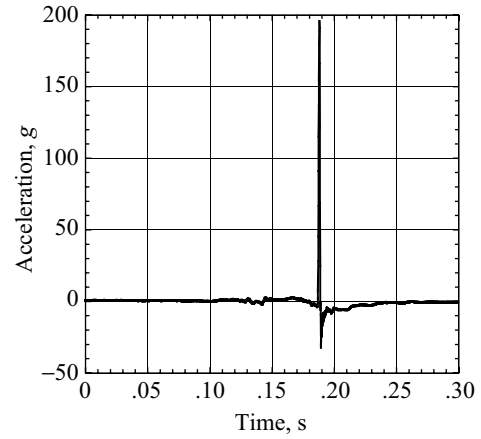


(c) Velocity time history (integrated unfiltered acceleration).

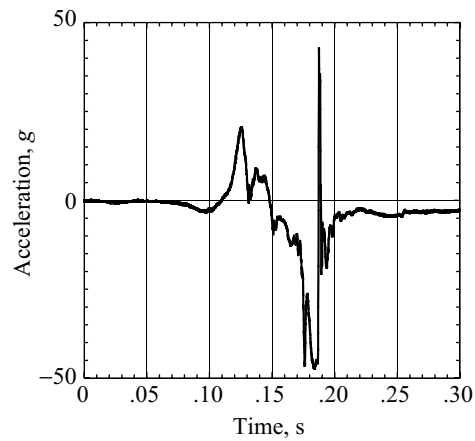
Figure A25. Vertical acceleration and velocity responses of the copilot seat floor.



(a) Forward acceleration time history.



(b) Side acceleration time history.



(c) Vertical acceleration time history.

Figure A26. Unfiltered copilot head acceleration time histories in three directions.

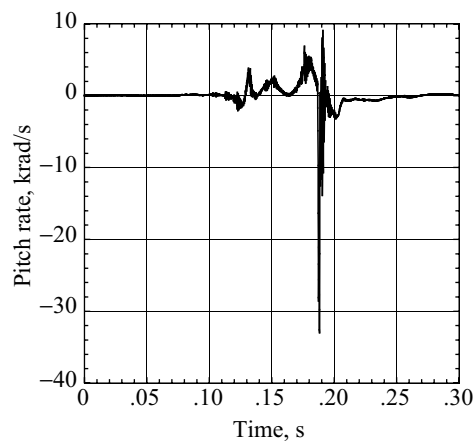
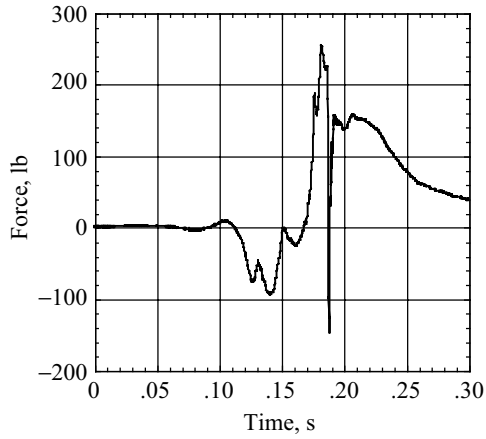
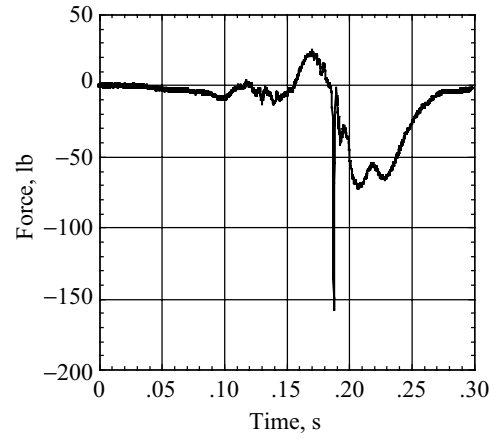


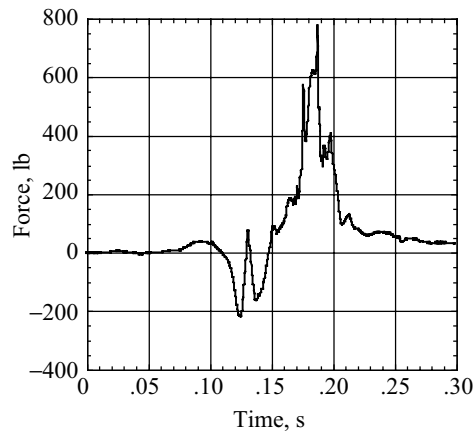
Figure A27. Unfiltered copilot head pitch rate about the side axis.



(a) Forward direction shear force.

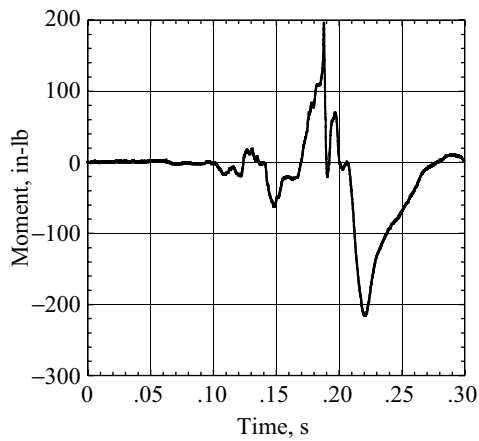


(b) Side direction shear force.

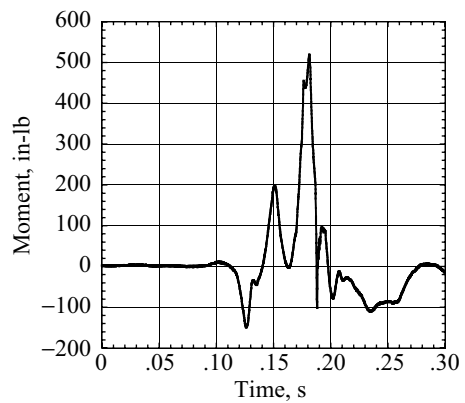


(c) Vertical direction force.

Figure A28. Unfiltered copilot head/neck force time histories in three directions.

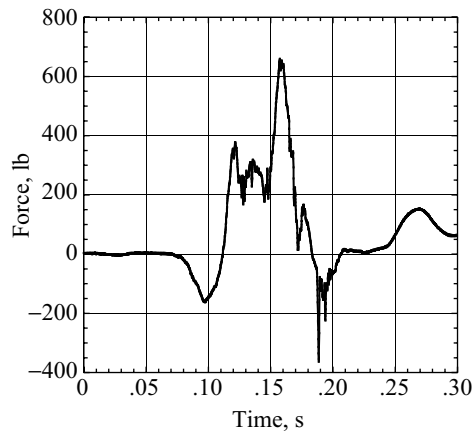


(a) Forward direction.

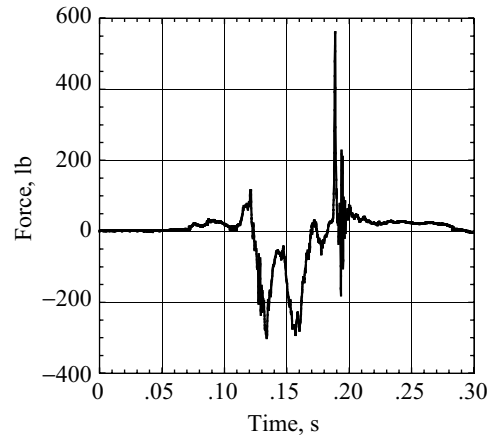


(b) Side direction.

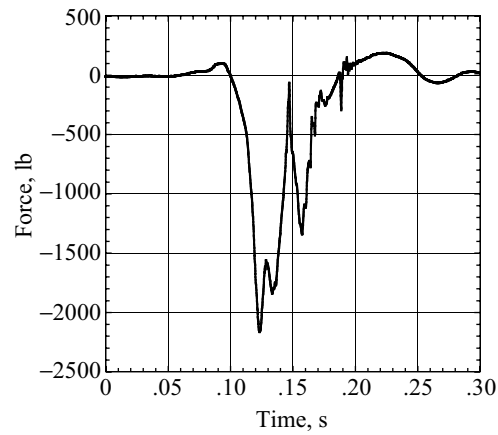
Figure A29. Unfiltered copilot head moment time histories in two directions.



(a) Forward direction.



(b) Side direction.



(c) Vertical direction.

Figure A30. Unfiltered copilot lumbar force time histories in three directions.

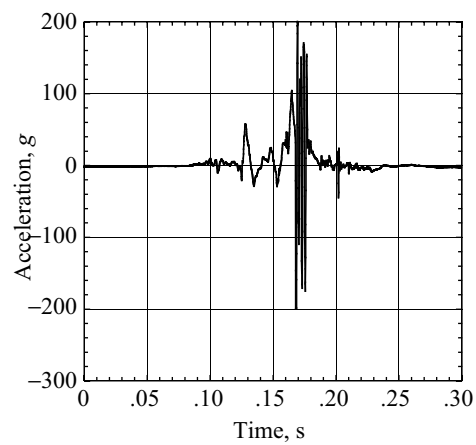


Figure A31. Unfiltered forward acceleration response of the copilot torso sternum.

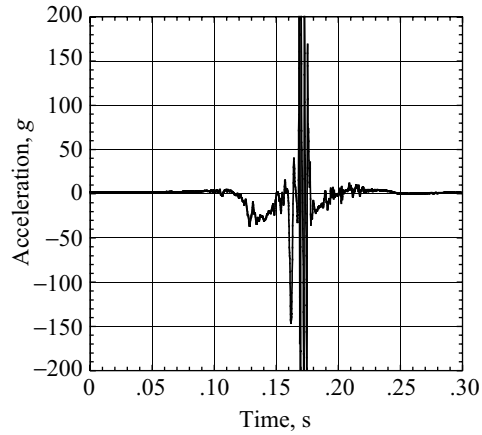
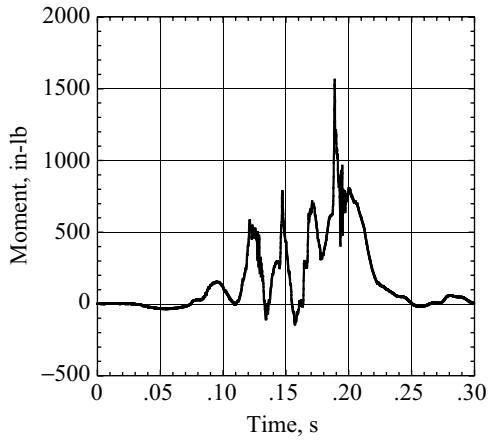
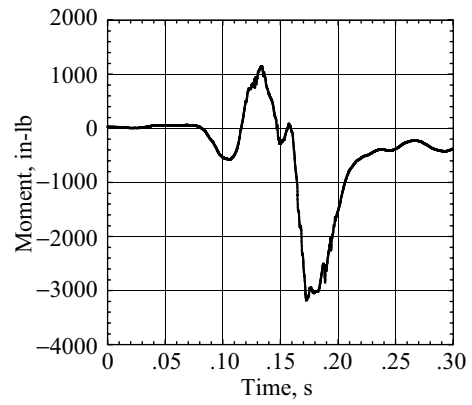


Figure A32. Unfiltered vertical acceleration response of the copilot torso sternum.



(a) Pelvis/lumbar forward moment.



(b) Pelvis/lumbar side moment.

Figure A33. Unfiltered moment responses of the copilot pelvis/lumbar region.

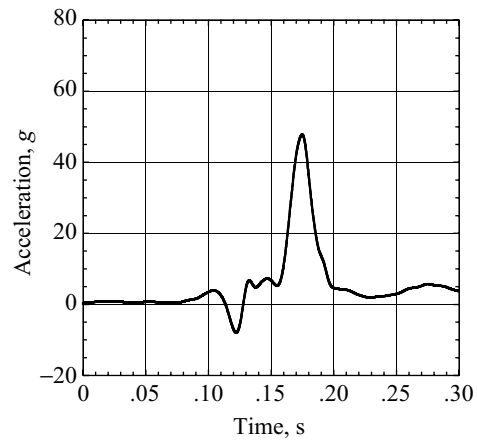
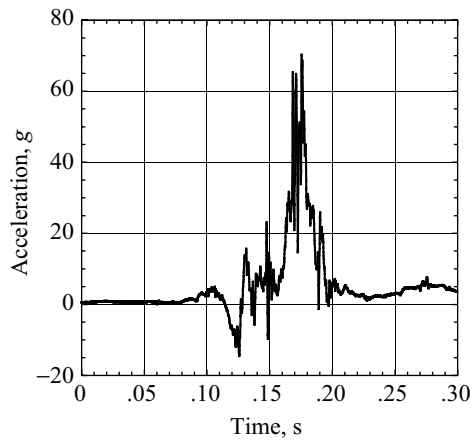


Figure A34. Unfiltered (left plot) and filtered (right plot) forward acceleration responses of the copilot torso.

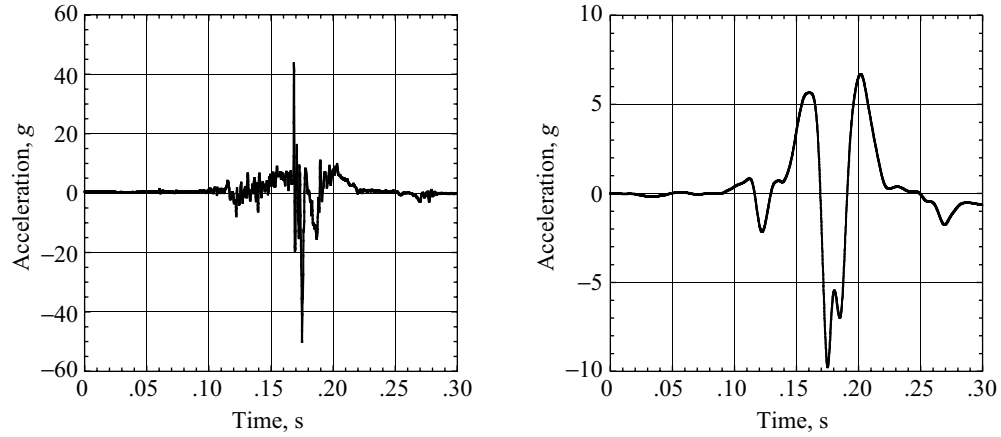


Figure A35. Unfiltered (left plot) and filtered (right plot) side acceleration responses of the copilot torso.

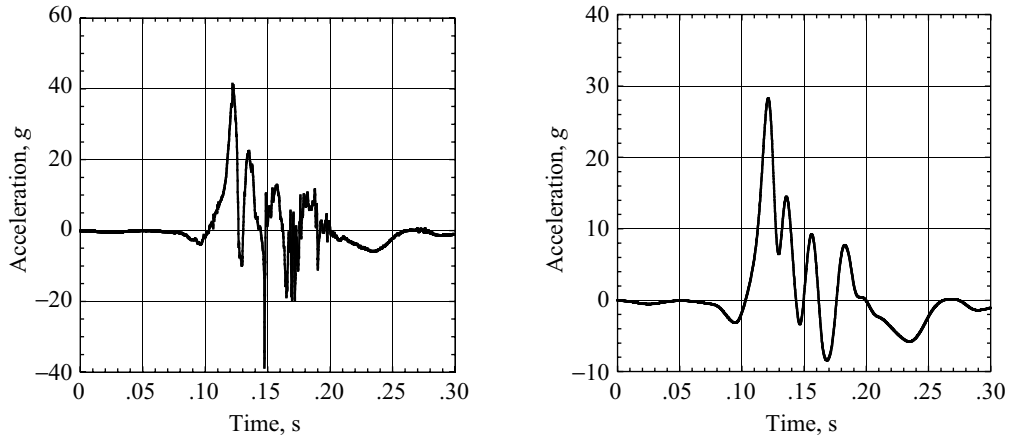


Figure A36. Unfiltered (left plot) and filtered (right plot) vertical acceleration responses of the copilot torso.

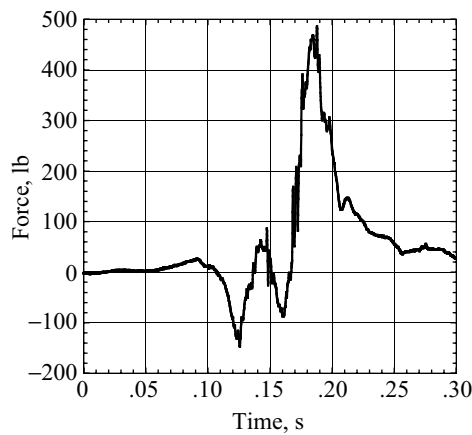


Figure A37. Unfiltered shear force response of the copilot torso in the forward direction.

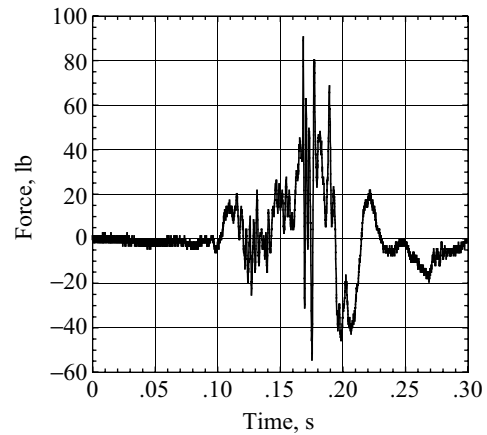


Figure A38. Unfiltered shear force response of the copilot torso in the side direction.

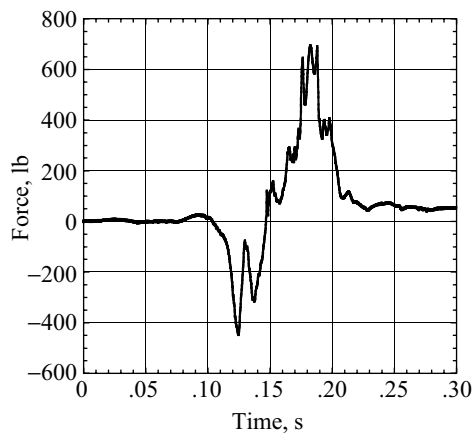


Figure A39. Unfiltered force response of the copilot torso in the vertical direction.

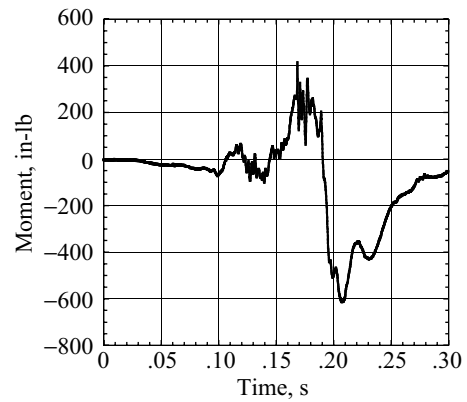


Figure A40. Unfiltered copilot torso moment response about the forward axis.

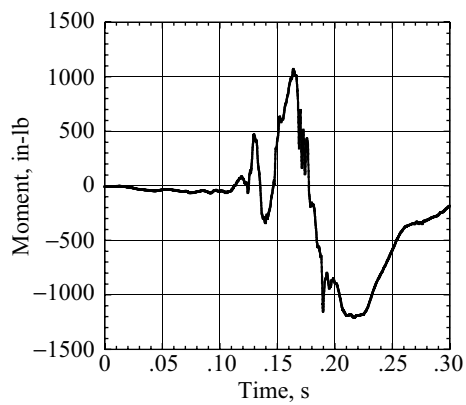


Figure A41. Unfiltered copilot torso moment time history about the side axis.

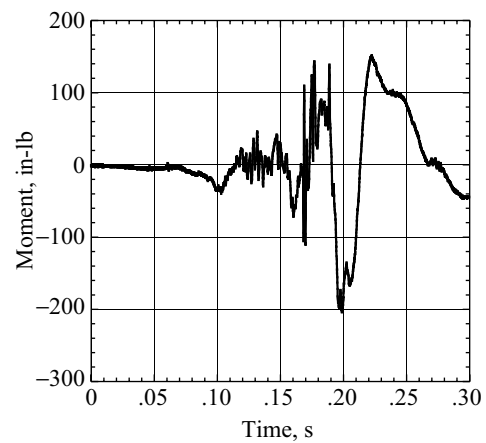


Figure A42. Unfiltered copilot torso moment time history about the vertical axis.

A5. Right and Left Troop Dummy Responses

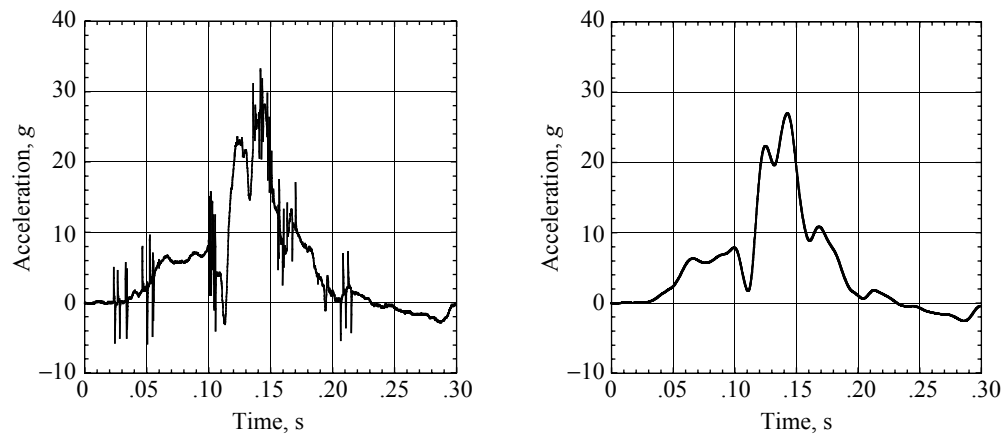


Figure A43. Unfiltered (left plot) and filtered (right plot) vertical acceleration responses of the right troop chest.

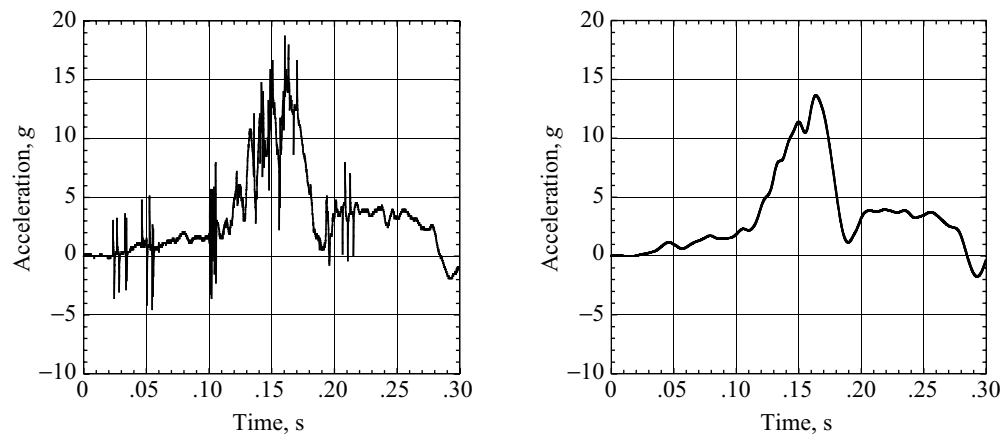


Figure A44. Unfiltered (left plot) and filtered (right plot) forward acceleration responses of the right troop chest.

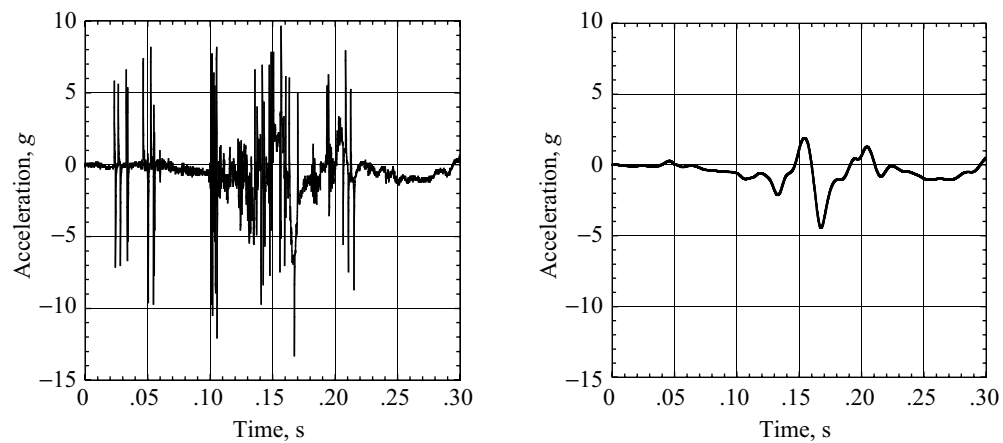
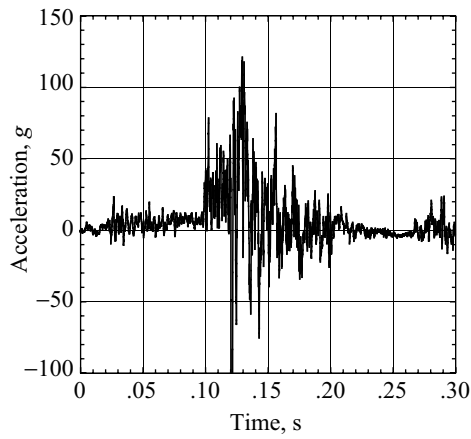
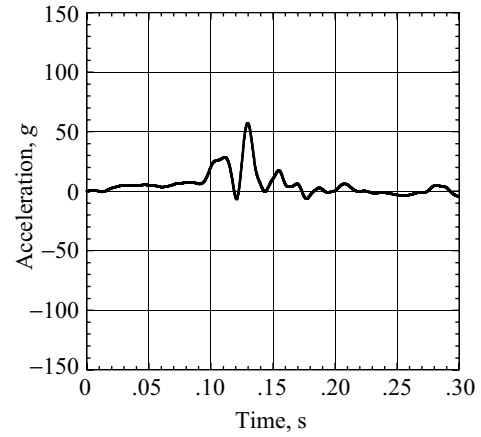


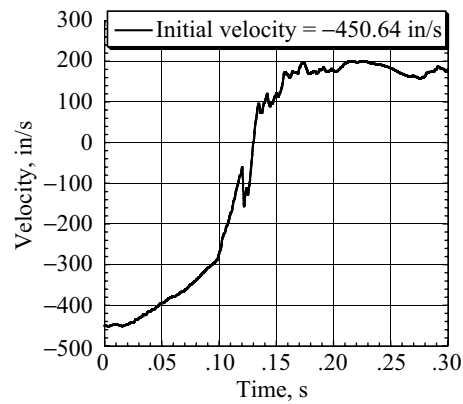
Figure A45. Unfiltered (left plot) and filtered (right plot) side acceleration responses of the right troop chest.



(a) Unfiltered acceleration time history.



(b) Filtered acceleration time history.



(c) Velocity time history (integrated unfiltered acceleration).

Figure A46. Vertical acceleration and velocity responses of the right troop seat pan.

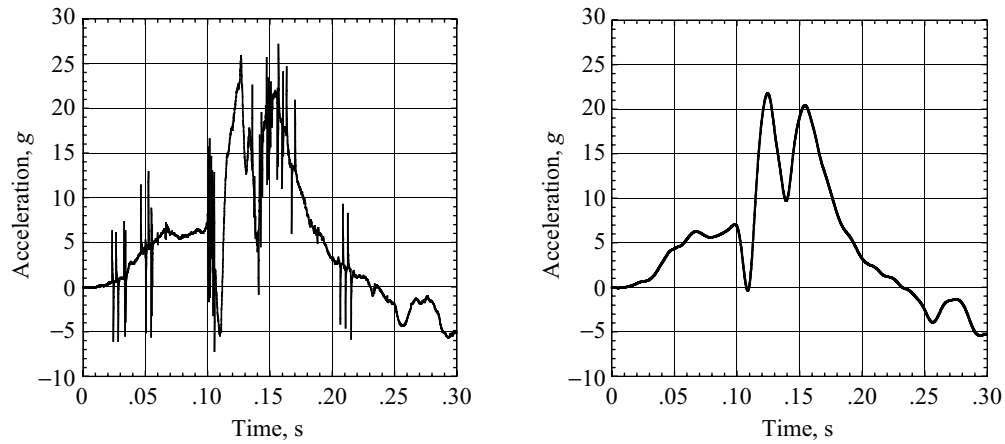


Figure A47. Unfiltered (left plot) and filtered (right plot) vertical acceleration responses of the left troop chest.

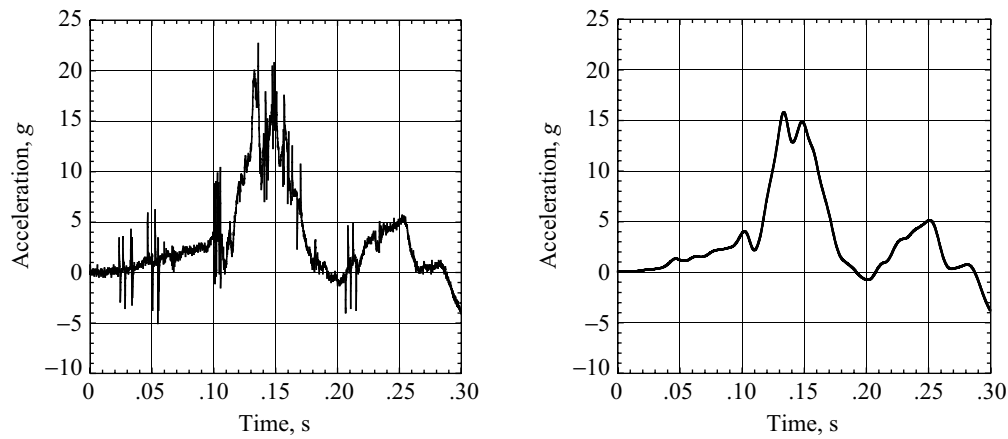


Figure A48. Unfiltered (left plot) and filtered (right plot) forward acceleration responses of the left troop chest.

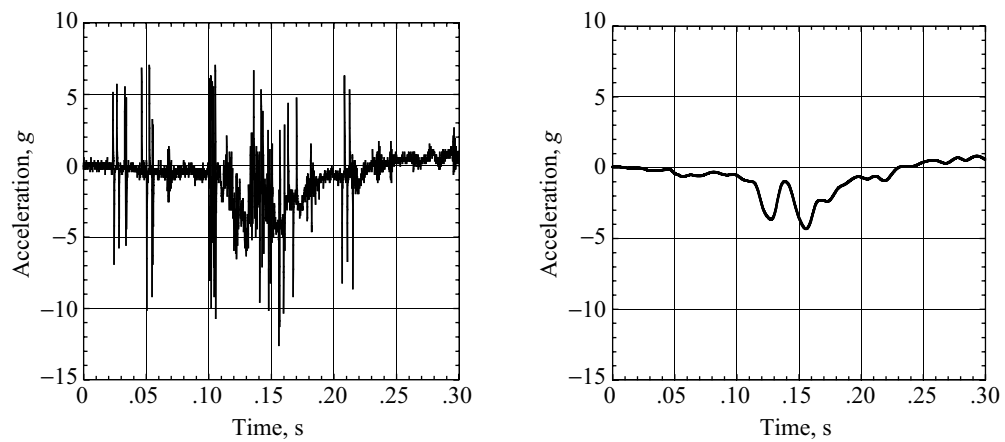
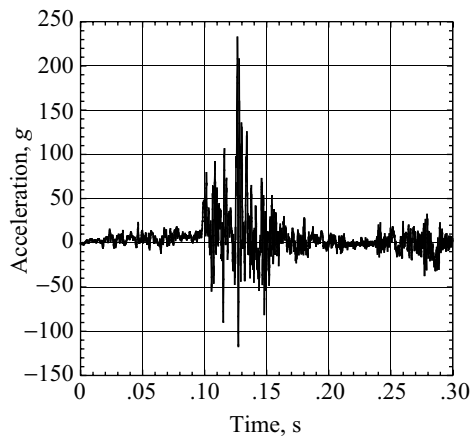
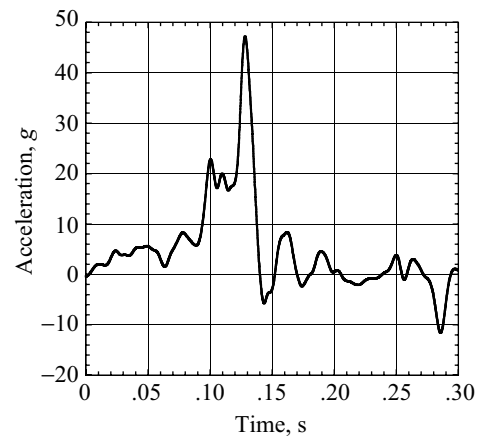


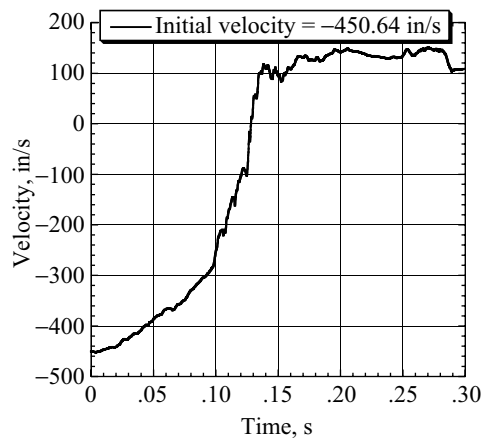
Figure A49. Unfiltered (left plot) and filtered (right plot) side acceleration responses of the left troop chest.



(a) Unfiltered acceleration time history.



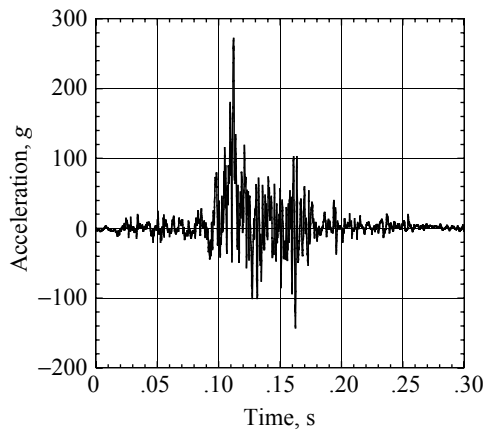
(b) Filtered acceleration time history.



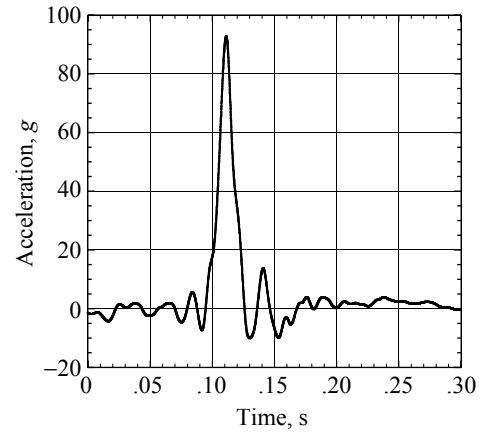
(c) Velocity time history (integrated unfiltered acceleration).

Figure A50. Vertical acceleration and velocity responses of the left troop seat pan.

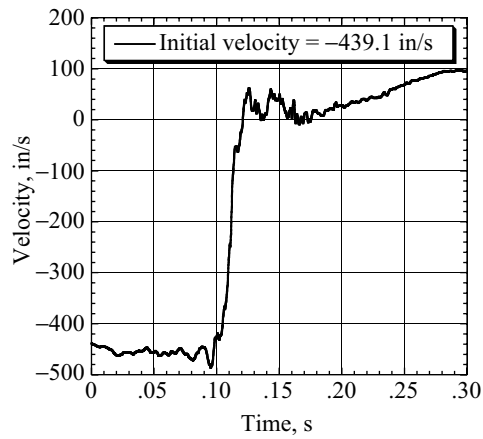
A6. Fuselage Structural Responses



(a) Unfiltered acceleration time history.



(b) Filtered acceleration time history.



(c) Velocity time history (integrated unfiltered acceleration).

Figure A51. Vertical acceleration and velocity responses of the pilot seat floor.

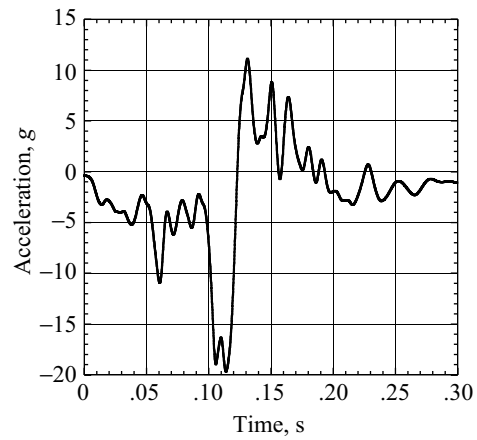
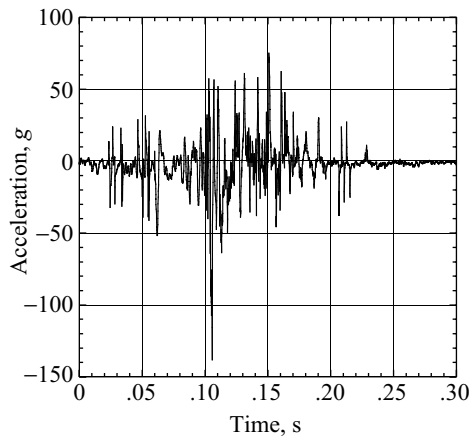


Figure A52. Unfiltered (left plot) and filtered (right plot) forward acceleration responses of the pilot seat floor.

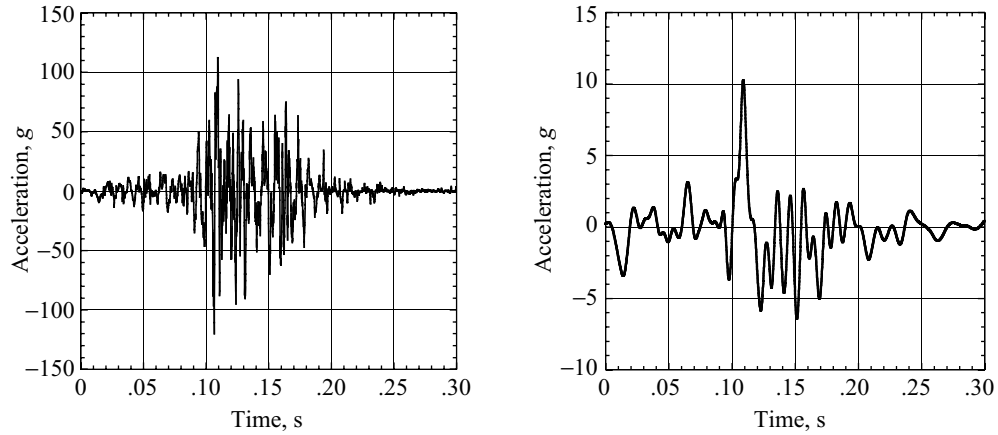
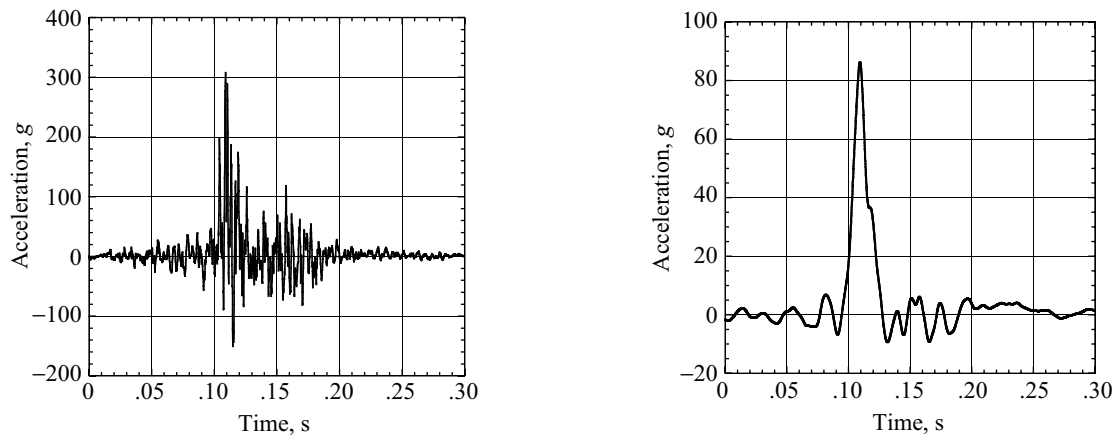
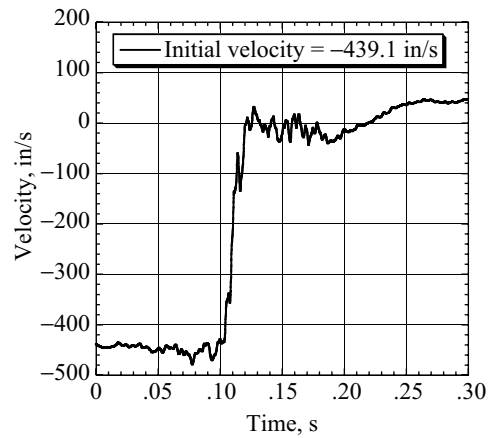


Figure A53. Unfiltered (left plot) and filtered (right plot) side acceleration responses of the pilot seat floor.



(a) Unfiltered acceleration time history.

(b) Filtered acceleration time history.



(c) Velocity time history (integrated unfiltered acceleration).

Figure A54. Vertical acceleration and velocity responses of the copilot seat floor.

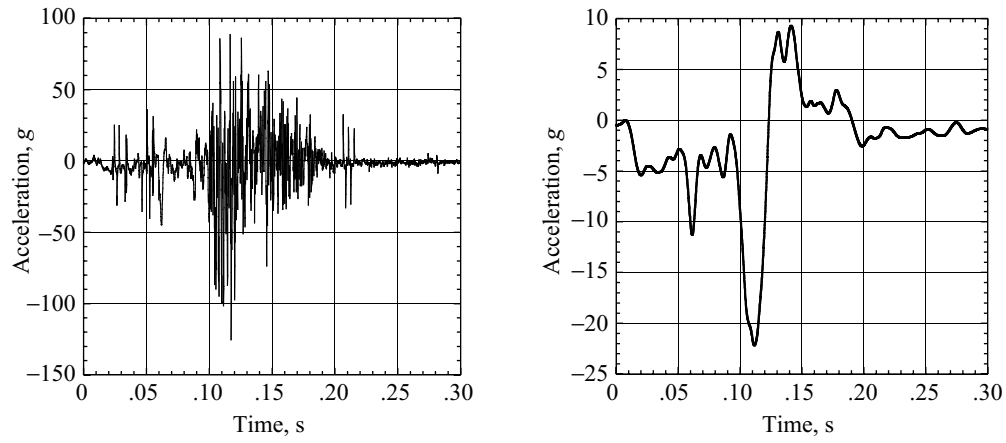


Figure A55. Unfiltered (left plot) and filtered (right plot) forward acceleration responses of the copilot seat floor.

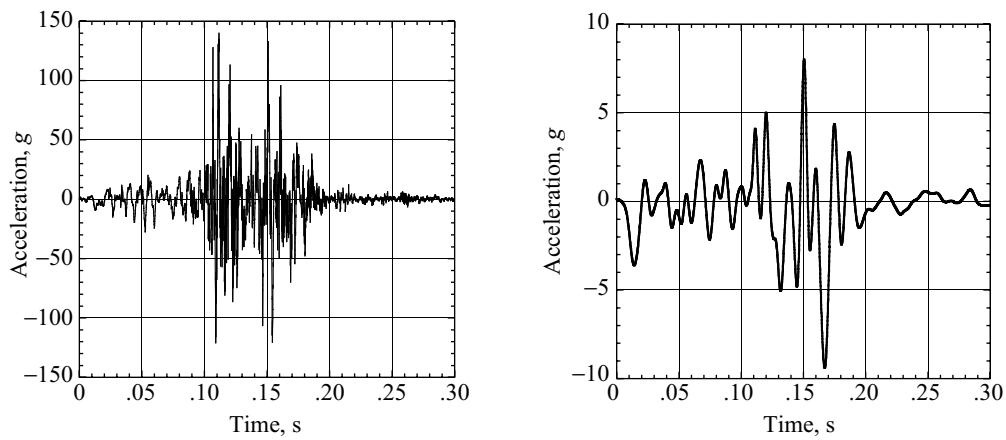
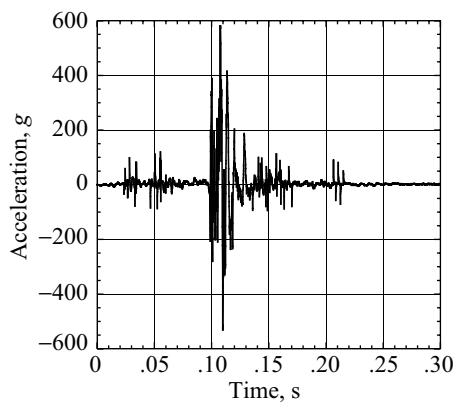
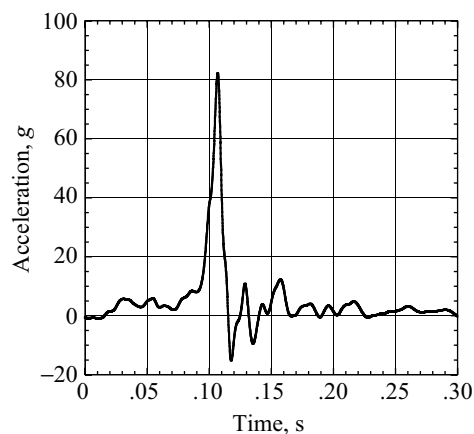


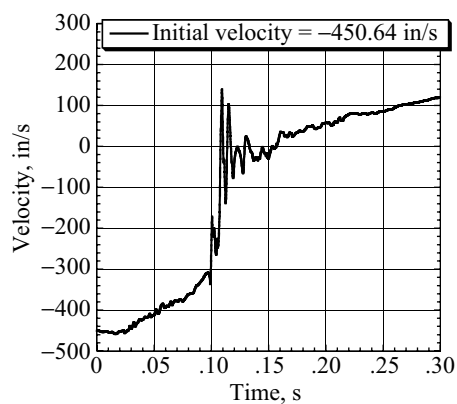
Figure A56. Unfiltered (left plot) and filtered (right plot) side acceleration responses of the copilot seat floor.



(a) Unfiltered acceleration time history.



(b) Filtered acceleration time history.



(c) Velocity time history (integrated unfiltered acceleration).

Figure A57. Vertical acceleration and velocity responses of the right troop seat floor.

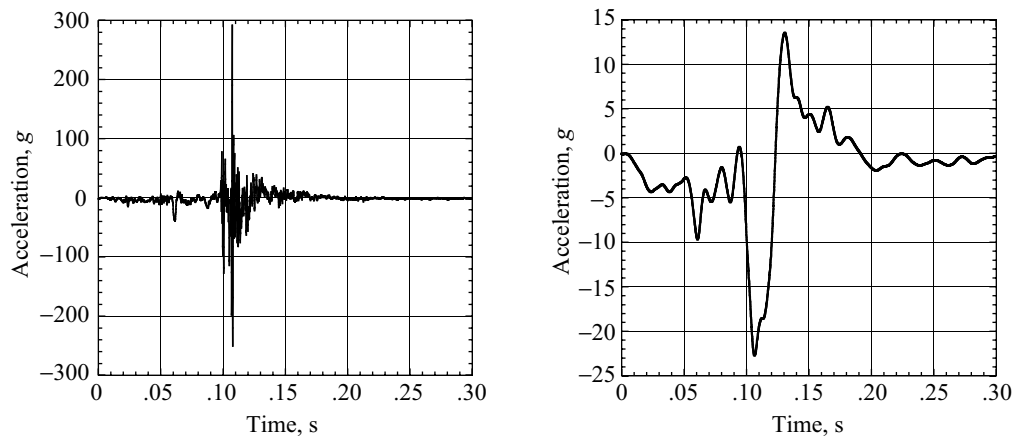
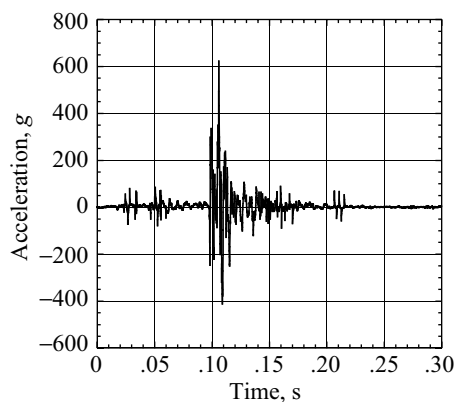
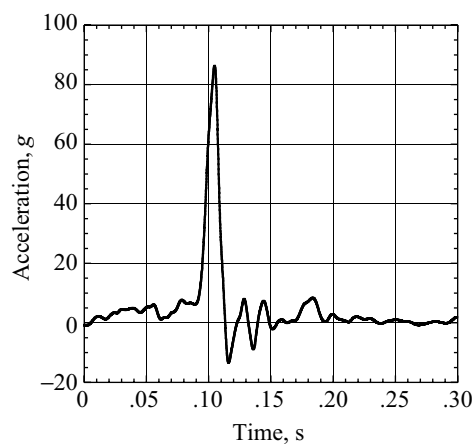


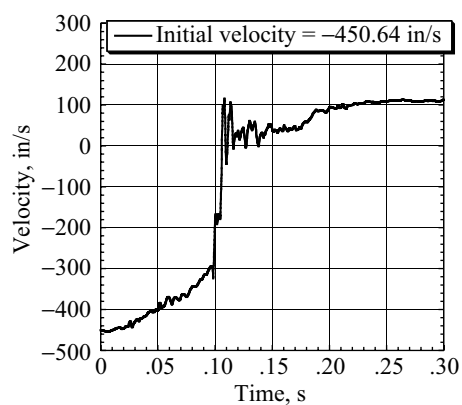
Figure A58. Unfiltered (left plot) and filtered (right plot) forward acceleration responses of the right troop seat floor.



(a) Unfiltered acceleration time history.



(b) Filtered acceleration time history.



(c) Velocity time history (integrated unfiltered acceleration).

Figure A59. Vertical acceleration and velocity responses of the left troop seat floor.

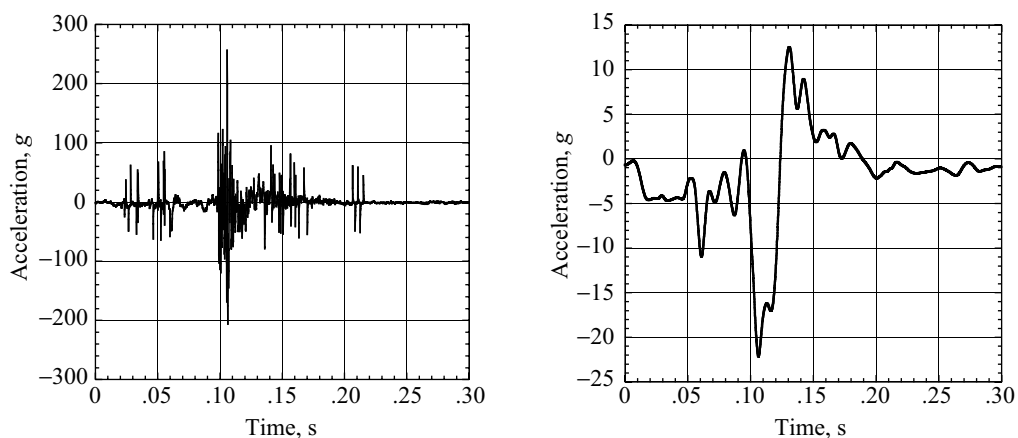


Figure A60. Unfiltered (left plot) and filtered (right plot) forward acceleration responses of the left troop seat floor.

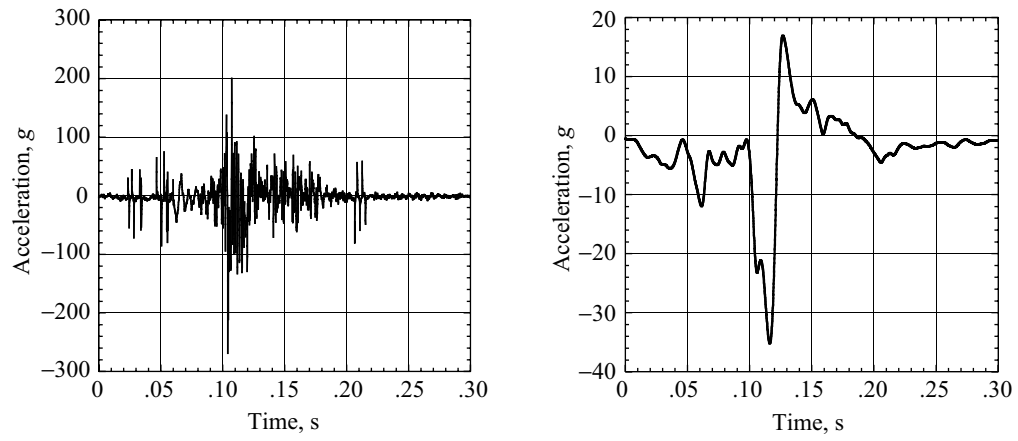


Figure A61. Unfiltered (left plot) and filtered (right plot) forward acceleration responses of the floor at FS 122.

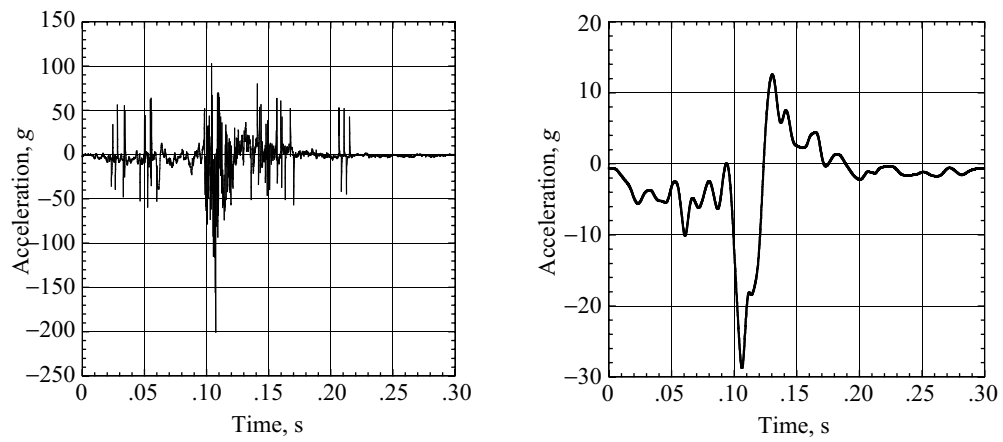
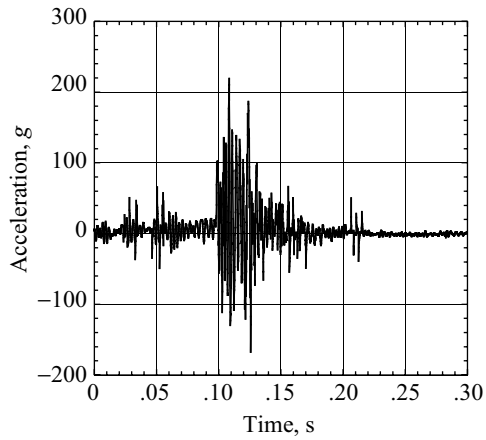
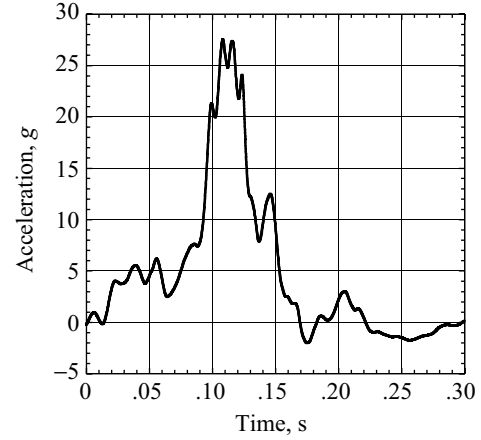


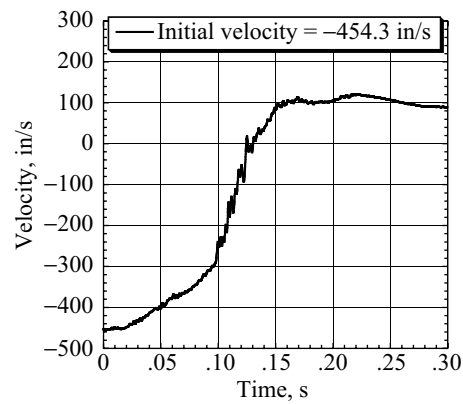
Figure A62. Unfiltered (left plot) and filtered (right plot) forward acceleration responses of the floor at FS 188.



(a) Unfiltered acceleration time history.



(b) Filtered acceleration time history.



(c) Velocity time history (integrated unfiltered acceleration).

Figure A63. Vertical acceleration and velocity responses of the top of the bulkhead at FS 188.

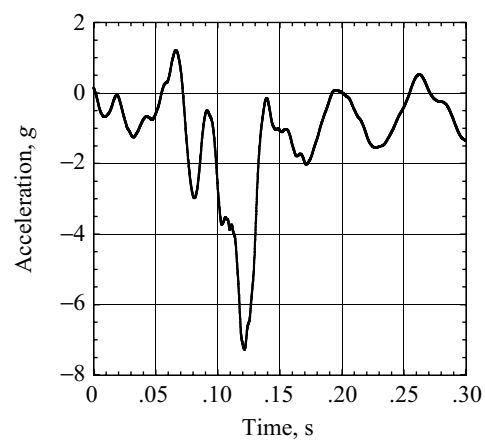
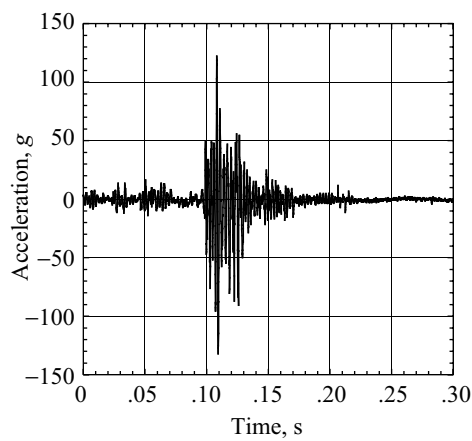
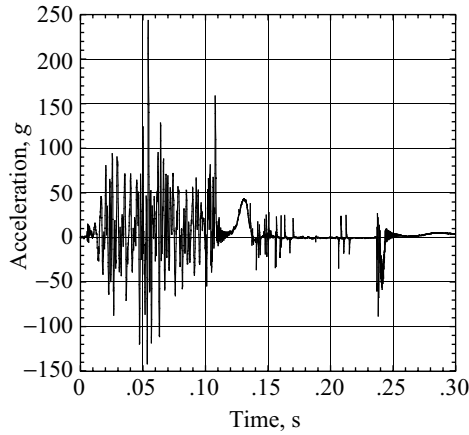
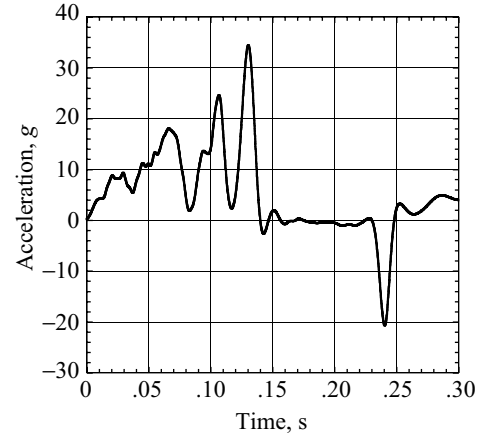


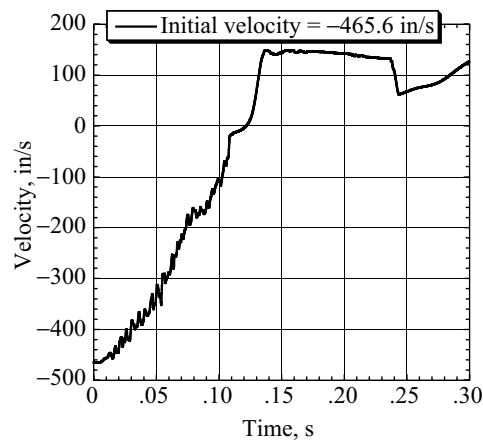
Figure A64. Unfiltered (left plot) and filtered (right plot) forward acceleration responses of the top of the bulkhead at FS 188.



(a) Unfiltered acceleration time history.



(b) Filtered acceleration time history.



(c) Velocity time history (integrated unfiltered acceleration).

Figure A65. Vertical acceleration and velocity responses of the bulkhead at FS 255.

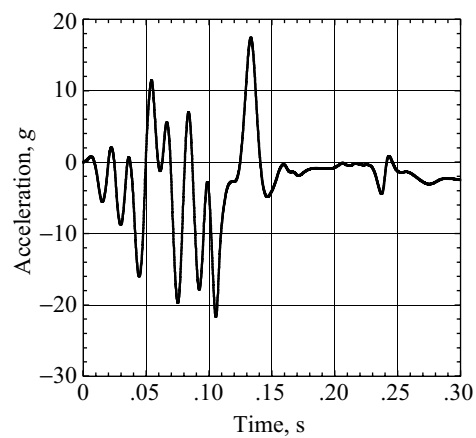
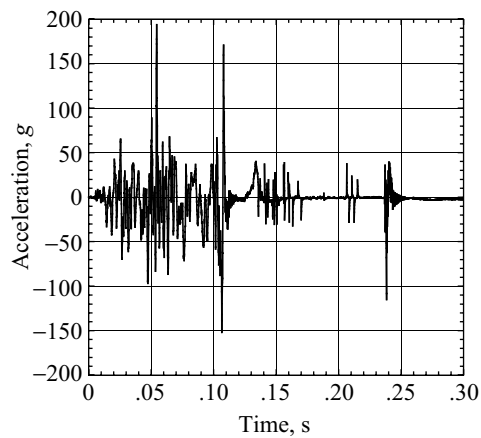
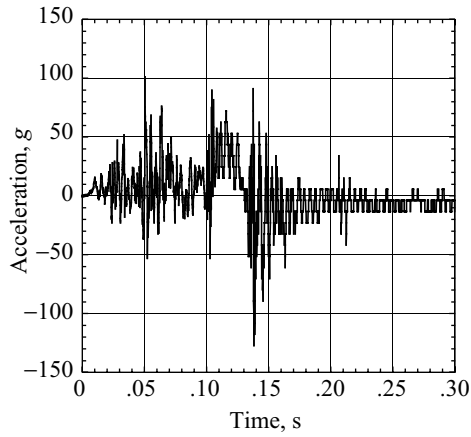
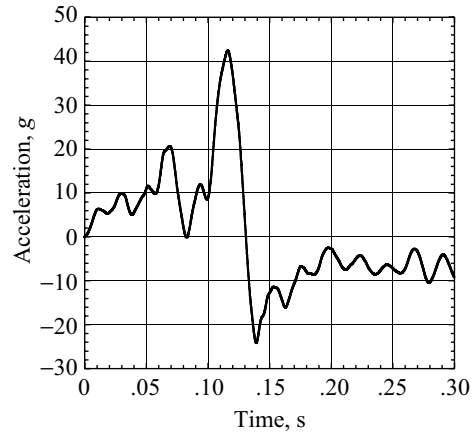


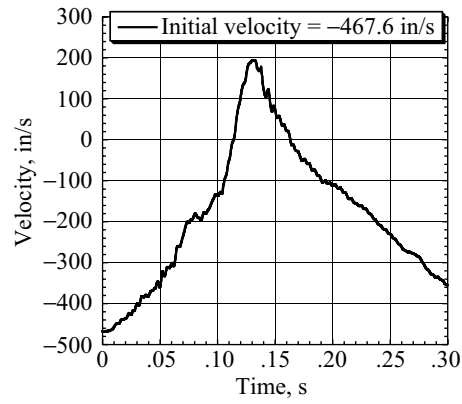
Figure A66. Unfiltered (left plot) and filtered (right plot) forward acceleration responses of the bulkhead at FS 255.



(a) Unfiltered acceleration time history.



(b) Filtered acceleration time history.



(c) Velocity time history (integrated unfiltered acceleration).

Figure A67. Vertical acceleration and velocity responses of the bulkhead at FS 267.

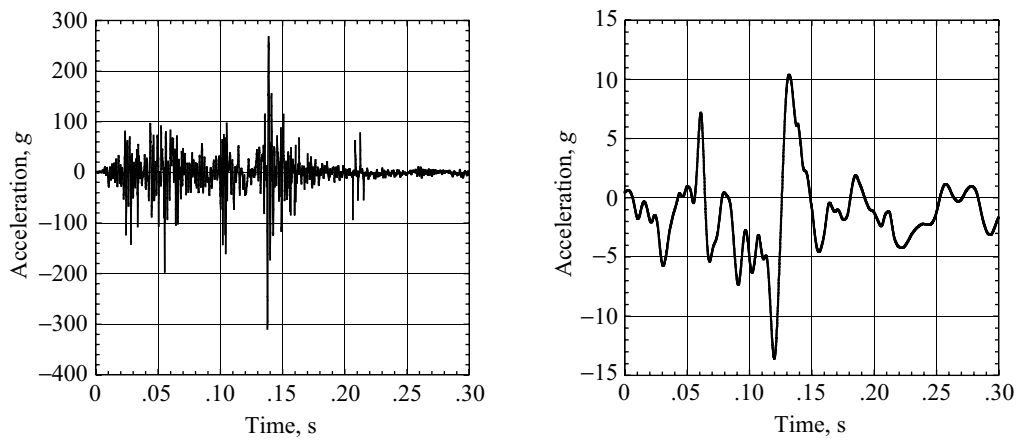


Figure A68. Unfiltered (left plot) and filtered (right plot) forward acceleration responses of the bulkhead at FS 267.

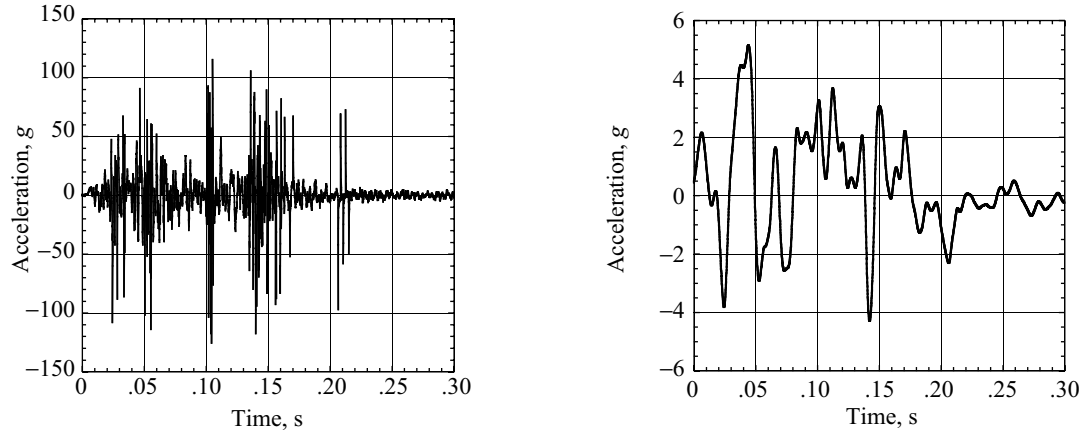
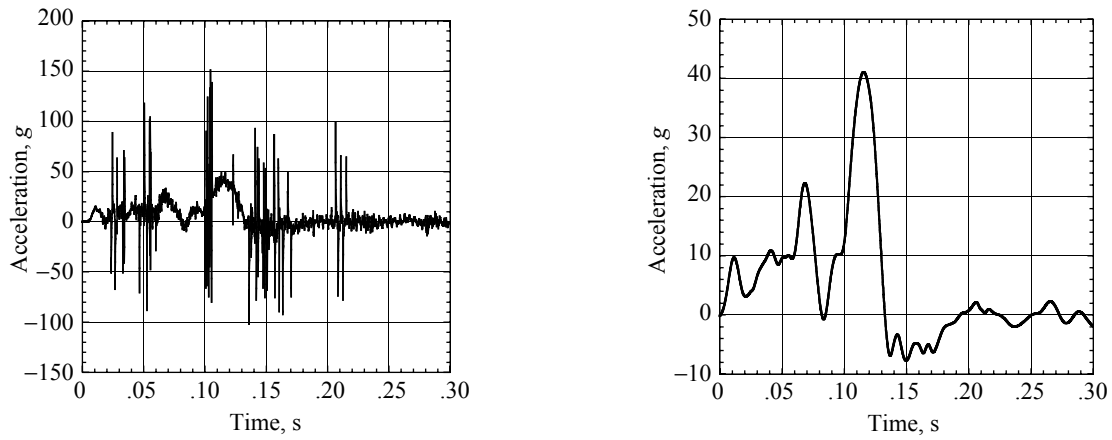


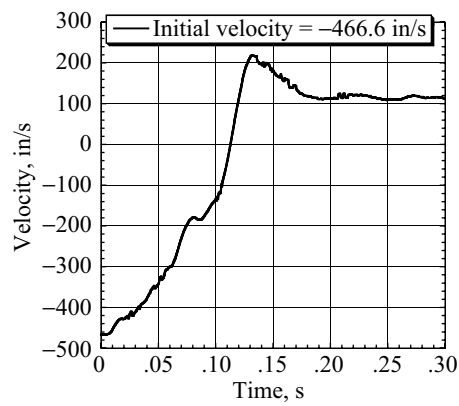
Figure A69. Unfiltered (left plot) and filtered (right plot) side acceleration responses of the bulkhead at FS 267.

A7. Rotor Transmission and Engine Responses



(a) Unfiltered acceleration time history.

(b) Filtered acceleration time history.



(c) Velocity time history (integrated unfiltered acceleration).

Figure A70. Vertical acceleration and velocity responses of the left engine.

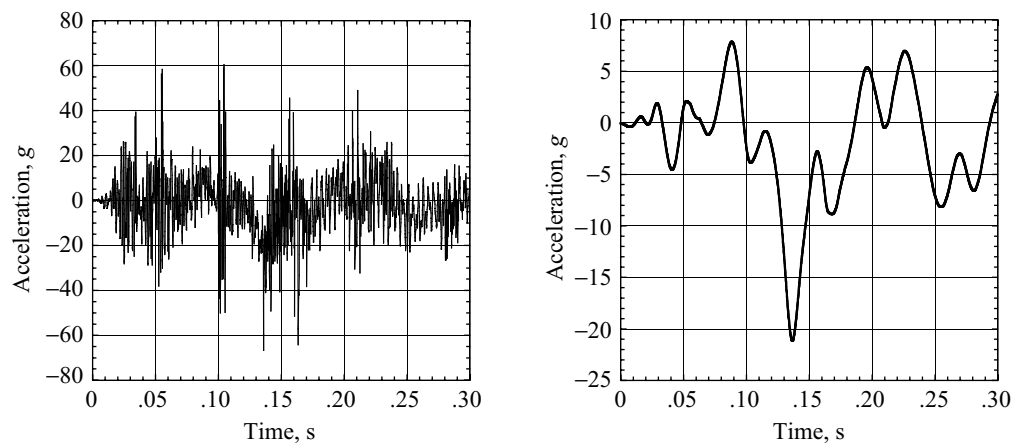


Figure A71. Unfiltered (left plot) and filtered (right plot) forward acceleration responses of the left engine.

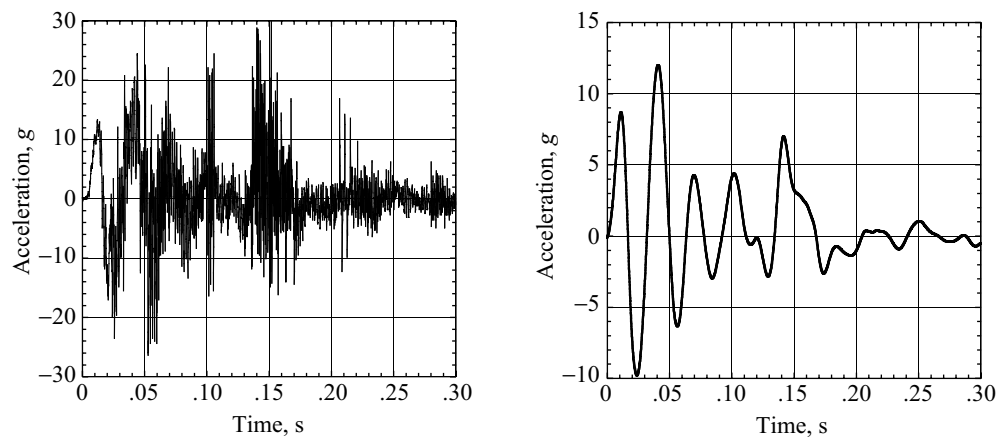
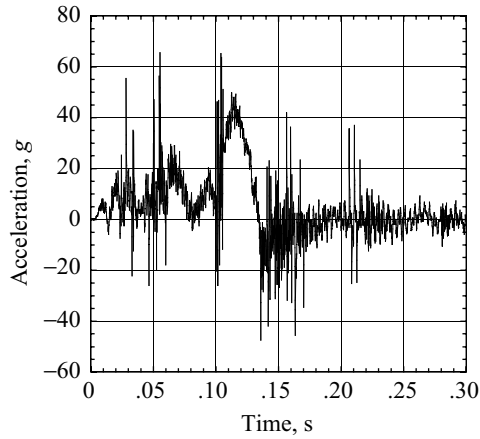
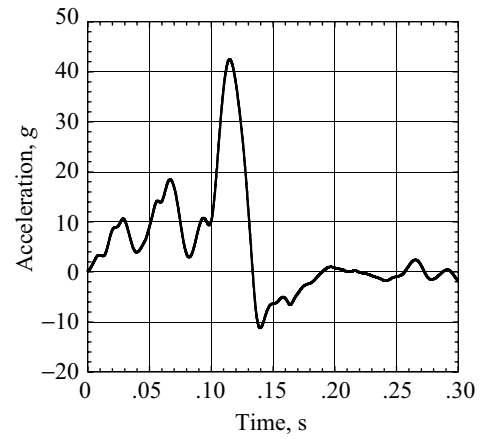


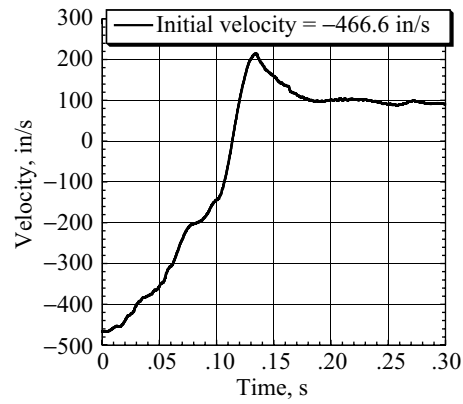
Figure A72. Unfiltered (left plot) and filtered (right plot) side acceleration responses of the left engine.



(a) Unfiltered acceleration time history.



(b) Filtered acceleration time history.



(c) Velocity time history (integrated unfiltered acceleration).

Figure A73. Vertical acceleration and velocity responses of the right engine.

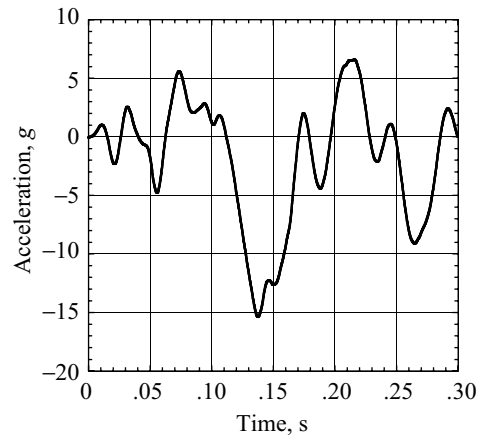
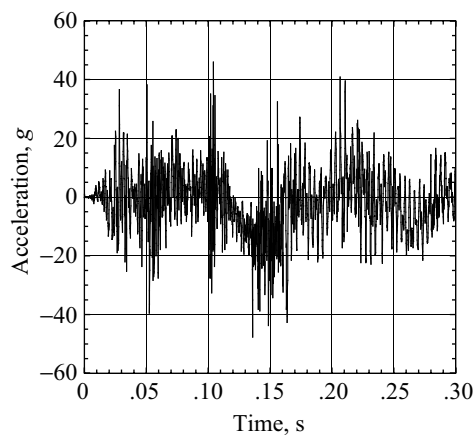
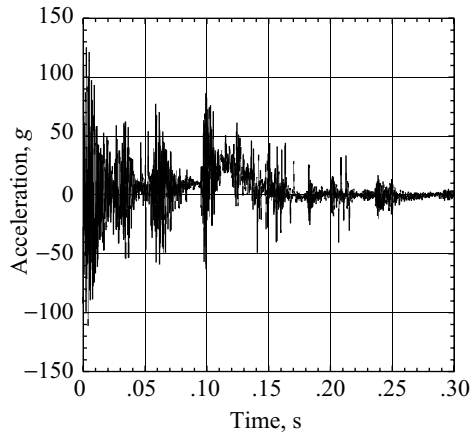
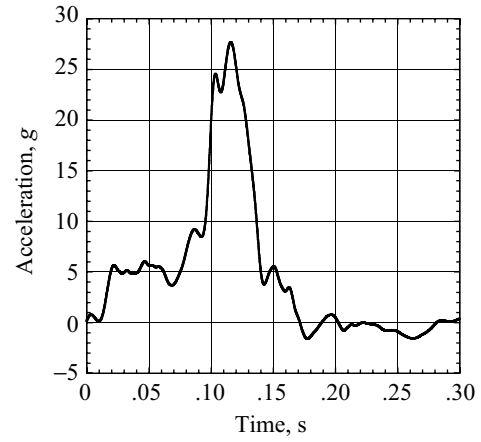


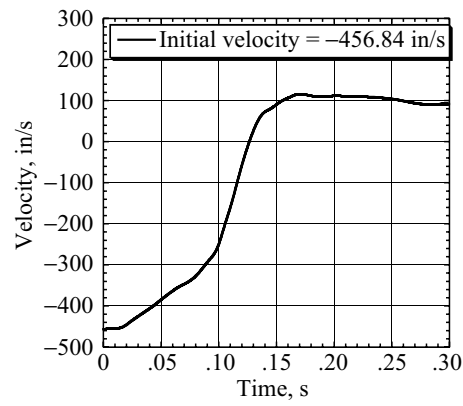
Figure A74. Unfiltered (left plot) and filtered (right plot) forward acceleration responses of the right engine.



(a) Unfiltered acceleration time history.



(b) Filtered acceleration time history.



(c) Velocity time history (integrated unfiltered acceleration).

Figure A75. Vertical acceleration and velocity responses of the rotor head.

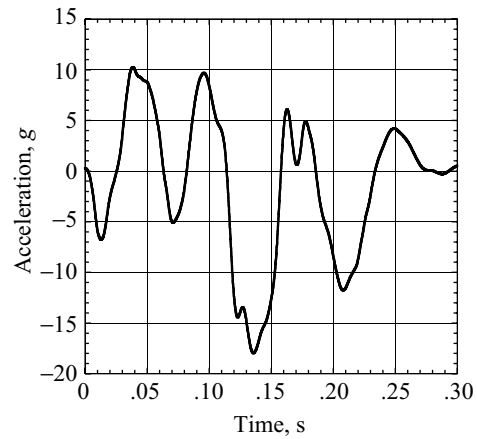
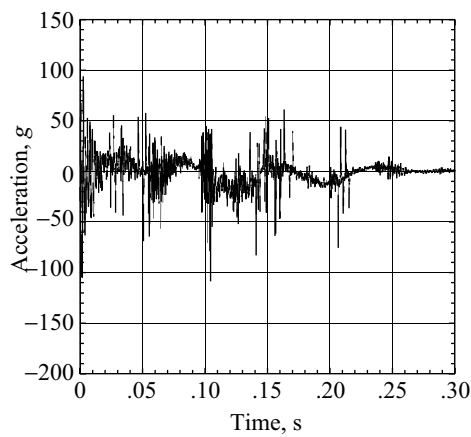
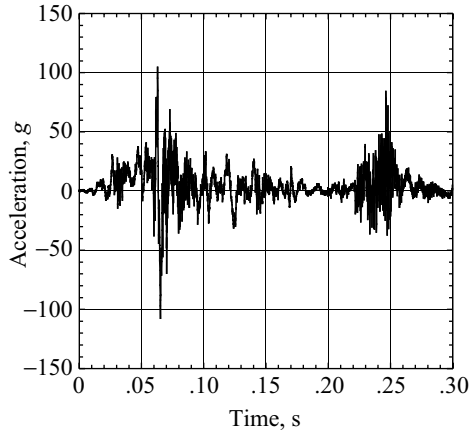
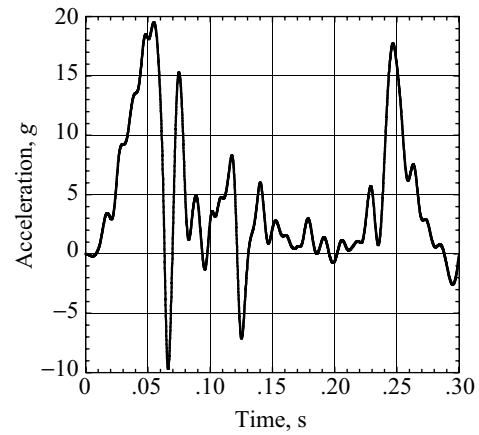


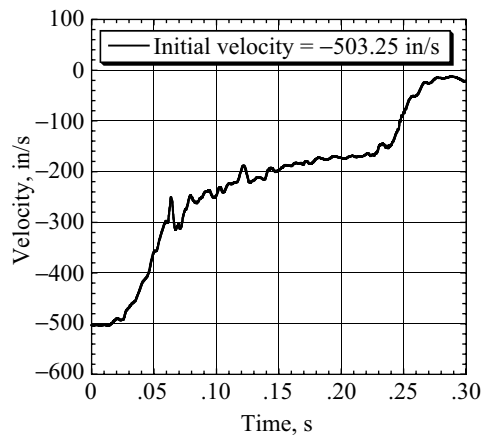
Figure A76. Unfiltered (left plot) and filtered (right plot) forward acceleration responses of the rotor head.



(a) Unfiltered acceleration time history.



(b) Filtered acceleration time history.



(c) Velocity time history (integrated unfiltered acceleration).

Figure A77. Vertical acceleration and velocity responses of the tail rotor.

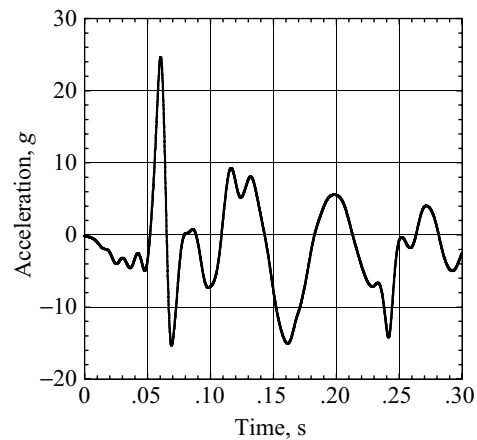
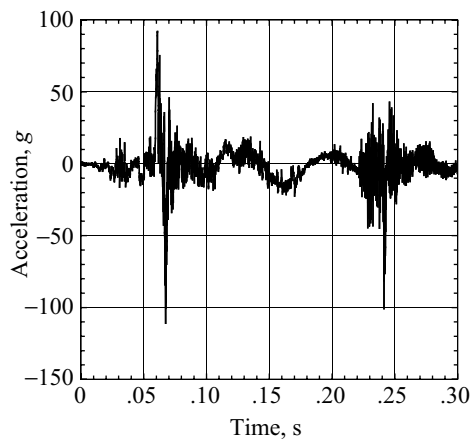
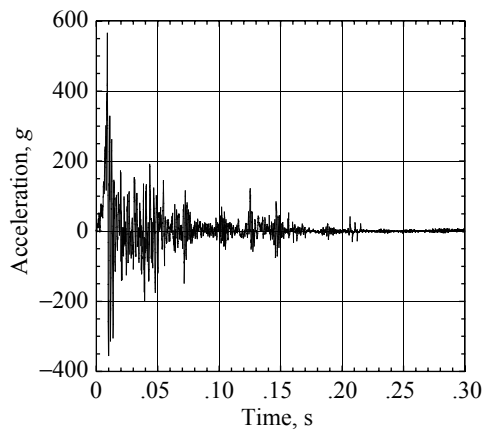
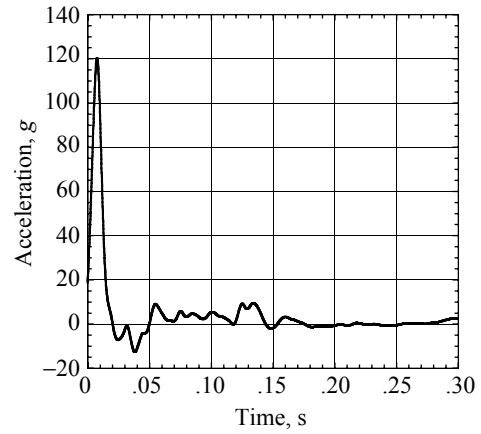


Figure A78. Unfiltered (left plot) and filtered (right plot) forward acceleration responses of the tail rotor.

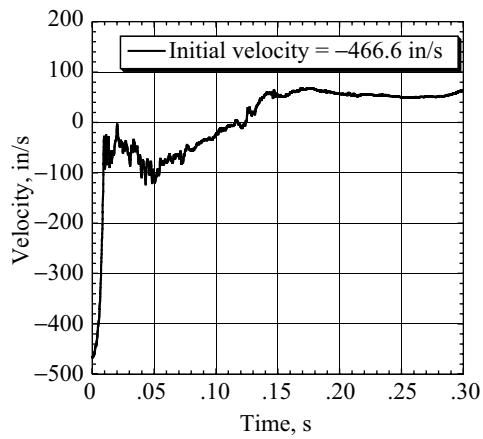
A8. Landing Gear Responses



(a) Unfiltered acceleration time history.

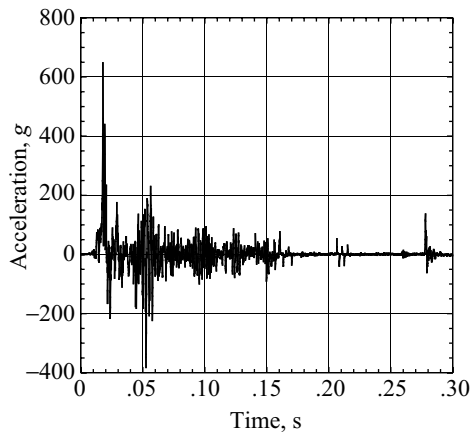


(b) Filtered acceleration time history.

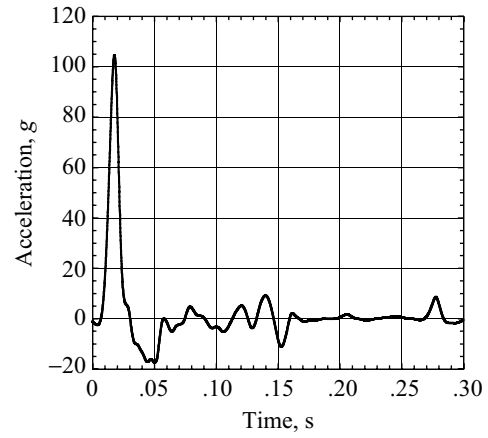


(c) Velocity time history (integrated unfiltered acceleration).

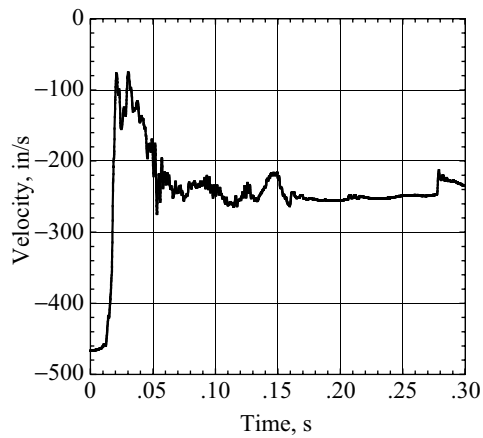
Figure A79. Vertical acceleration and velocity responses of the left main gear hub.



(a) Unfiltered acceleration time history.

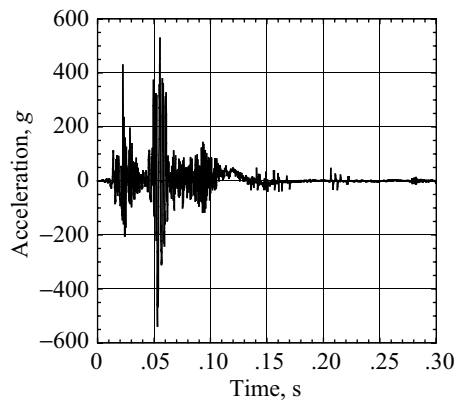


(b) Filtered acceleration time history.

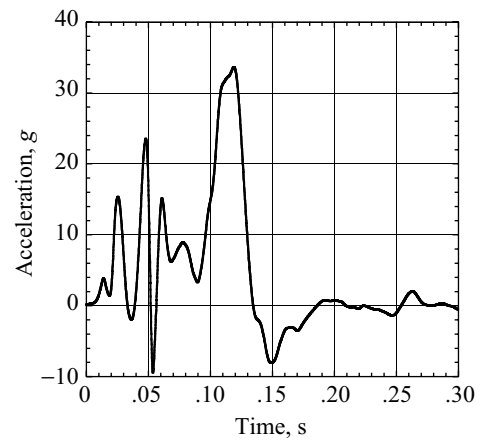


(c) Velocity time history (integrated unfiltered acceleration).

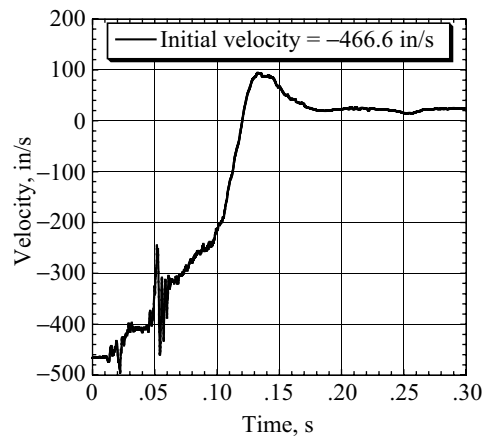
Figure A80. Vertical acceleration and velocity responses of the right main gear hub.



(a) Unfiltered acceleration time history.



(b) Filtered acceleration time history.



(c) Velocity time history (integrated unfiltered acceleration).

Figure A81. Vertical acceleration and velocity responses of the right main gear top.

A9. Fuel Tank Pressure Responses

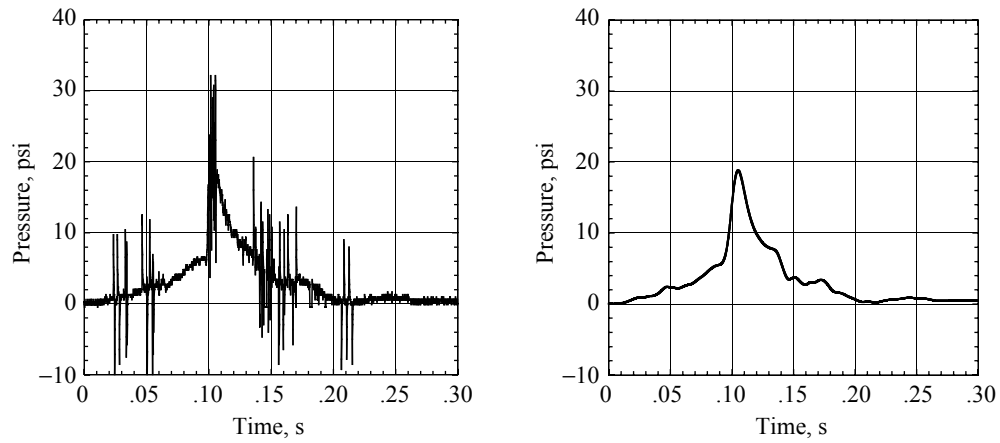


Figure A82. Unfiltered (left plot) and filtered (right plot) pressure responses of the fuel tank (inside left).

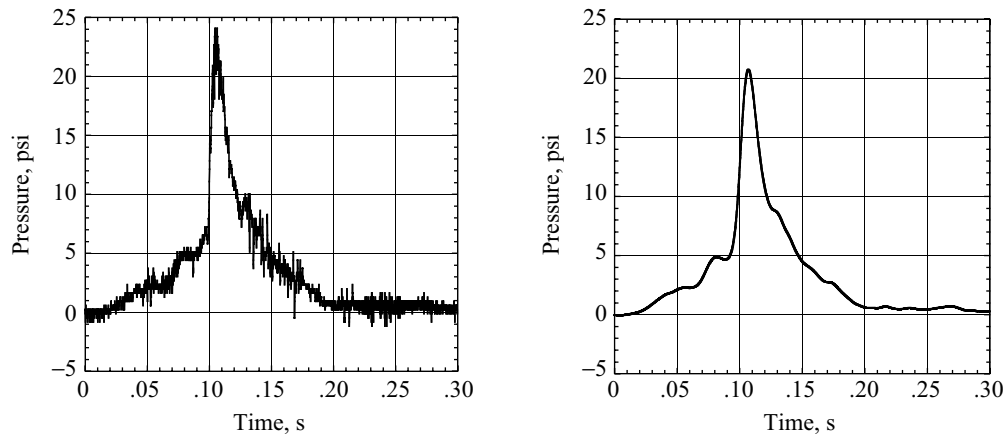


Figure A83. Unfiltered (left plot) and filtered (right plot) pressure responses of fuel tank (inside right).

A10. Tail Continuity Gauge

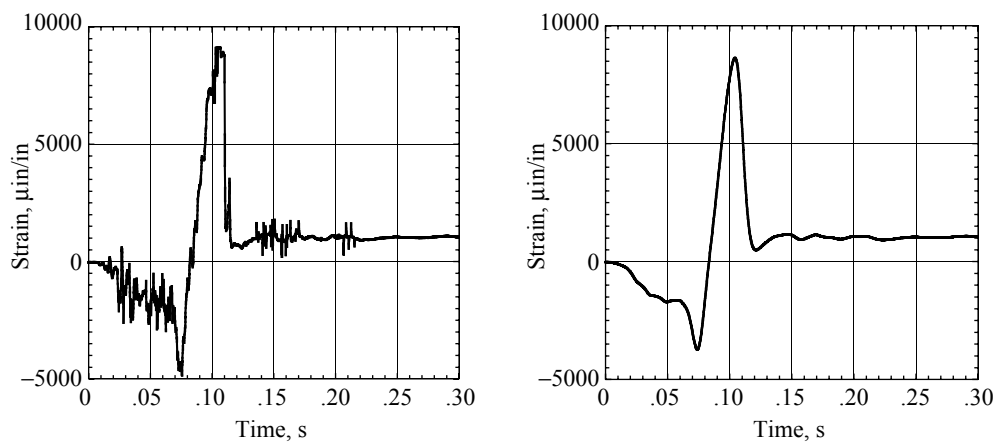


Figure A84. Unfiltered (left plot) and filtered (right plot) strain responses from the tail continuity gauge.

REPORT DOCUMENTATION PAGE					Form Approved OMB No. 0704-0188	
<p>The public reporting burden for this collection of information is estimated to average 1 hour per response, including the time for reviewing instructions, searching existing data sources, gathering and maintaining the data needed, and completing and reviewing the collection of information. Send comments regarding this burden estimate or any other aspect of this collection of information, including suggestions for reducing this burden, to Department of Defense, Washington Headquarters Services, Directorate for Information Operations and Reports (0704-0188), 1215 Jefferson Davis Highway, Suite 1204, Arlington, VA 22202-4302. Respondents should be aware that notwithstanding any other provision of law, no person shall be subject to any penalty for failing to comply with a collection of information if it does not display a currently valid OMB control number.</p> <p>PLEASE DO NOT RETURN YOUR FORM TO THE ABOVE ADDRESS.</p>						
1. REPORT DATE (DD-MM-YYYY)		2. REPORT TYPE		3. DATES COVERED (From - To)		
01- 08 - 2003		Technical Publication				
4. TITLE AND SUBTITLE Full-Scale Crash Test and Finite Element Simulation of a Composite Prototype Helicopter				5a. CONTRACT NUMBER		
				5b. GRANT NUMBER		
				5c. PROGRAM ELEMENT NUMBER		
6. AUTHOR(S) Jackson, Karen E.; Fasanella, Edwin L.; Boitnott, Richard L.; and Lyle, Karen H.				5d. PROJECT NUMBER		
				5e. TASK NUMBER		
				5f. WORK UNIT NUMBER 728-50-10-01		
7. PERFORMING ORGANIZATION NAME(S) AND ADDRESS(ES) NASA Langley Research Center Hampton, VA 23681-2199				8. PERFORMING ORGANIZATION REPORT NUMBER L-18228		
9. SPONSORING/MONITORING AGENCY NAME(S) AND ADDRESS(ES) National Aeronautics and Space Administration Washington, DC 20546-0001				10. SPONSOR/MONITOR'S ACRONYM(S) NASA		
				11. SPONSOR/MONITOR'S REPORT NUMBER(S) NASA/TP-2003-212641 ARL-TR-2824		
12. DISTRIBUTION/AVAILABILITY STATEMENT Unclassified - Unlimited Subject Category 39 Availability: NASA CASI (301) 621-0390 Distribution: Standard						
13. SUPPLEMENTARY NOTES Jackson, Fasanella, and Boitnott, U.S. Army Research Laboratory. Lyle, Langley Research Center. An electronic version can be found at http://techreports.larc.nasa.gov/ltrs/ or http://ntrs.nasa.gov						
14. ABSTRACT A full-scale crash test of a prototype composite helicopter was performed at the Impact Dynamics Research Facility at NASA Langley Research Center in 1999 to obtain data for validation of a finite element crash simulation. The helicopter was the flight test article built by Sikorsky Aircraft during the Advanced Composite Airframe Program (ACAP). The composite helicopter was designed to meet the stringent Military Standard (MIL-STD-1290A) crashworthiness criteria and was outfitted with two crew and two troop seats and four anthropomorphic dummies. The test was performed at 38-ft/s vertical and 32.5-ft/s horizontal velocity onto a rigid surface. An existing modal-vibration model of the Sikorsky ACAP helicopter was converted into a model suitable for crash simulation. A two-stage modeling approach was implemented and an external user-defined subroutine was developed to represent the complex landing gear response. The crash simulation was executed with a nonlinear, explicit transient dynamic finite element code. Predictions of structural deformation and failure, the sequence of events, and the dynamic response of the airframe structure were generated and the numerical results were correlated with the experimental data to validate the simulation. The test results, the model development, and the test-analysis correlation are described.						
15. SUBJECT TERMS Impact phenomena of aerospace structures; Shock testing; Composite materials; Energy absorption (structures); Dynamic structural analysis						
16. SECURITY CLASSIFICATION OF:			17. LIMITATION OF ABSTRACT	18. NUMBER OF PAGES	19a. NAME OF RESPONSIBLE PERSON	
a. REPORT	b. ABSTRACT	c. THIS PAGE			STI Help Desk (email: help@sti.nasa.gov)	
U	U	U	UU	121	19b. TELEPHONE NUMBER (Include area code) (301) 621-0390	